



저작자표시-비영리-변경금지 2.0 대한민국

이용자는 아래의 조건을 따르는 경우에 한하여 자유롭게

- 이 저작물을 복제, 배포, 전송, 전시, 공연 및 방송할 수 있습니다.

다음과 같은 조건을 따라야 합니다:



저작자표시. 귀하는 원저작자를 표시하여야 합니다.



비영리. 귀하는 이 저작물을 영리 목적으로 이용할 수 없습니다.



변경금지. 귀하는 이 저작물을 개작, 변형 또는 가공할 수 없습니다.

- 귀하는, 이 저작물의 재이용이나 배포의 경우, 이 저작물에 적용된 이용허락조건을 명확하게 나타내어야 합니다.
- 저작권자로부터 별도의 허가를 받으면 이러한 조건들은 적용되지 않습니다.

저작권법에 따른 이용자의 권리는 위의 내용에 의하여 영향을 받지 않습니다.

이것은 [이용허락규약\(Legal Code\)](#)을 이해하기 쉽게 요약한 것입니다.

[Disclaimer](#)

Practical Development of Si Anodes for High-Energy Lithium Ion Batteries

Sujong Chae

Department of Energy Engineering
(Battery Science and Technology)

Graduate School of UNIST

2019

Practical Development of Si Anodes for High-Energy Lithium Ion Batteries

Sujong Chae

Department of Energy Engineering
(Battery Science and Technology)

Graduate School of UNIST

Practical Development of Si Anodes for High-Energy Lithium Ion Batteries

A dissertation
submitted to the Graduate School of UNIST
in partial fulfillment of the requirements for the degree of
Doctor of Philosophy in Energy Engineering

Sujong Chae

12. 03. 2018

Approved by



Advisor

Jaephil Cho

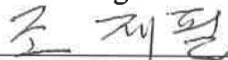
Practical Development of Si Anodes for High-Energy Lithium Ion Batteries

Sujong Chae

This certifies that the thesis/dissertation of Sujong Chae is approved.

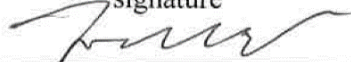
12. 03. 2018

signature



Advisor: Jaephil Cho

signature



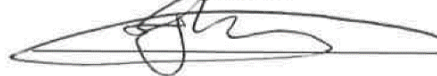
Kyeong-Min Jeong

signature



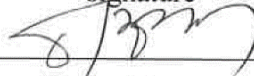
Nam-soon Choi

signature



Seok Ju Kang

signature



Hyun-Wook Lee

Abstract

Since the first commercialization of the lithium ion battery (LIB), LIB has played a significant role as a power source for electric devices. As increasing energy demands with the emergence of the electric vehicle and the energy storage system, improving the energy density of LIB has been recognized as one of the most important issue for battery researchers. Accordingly, the high-capacity materials have been investigated to break the theoretical capacity limit of current LIB chemistry with the carbonaceous anode and the lithium metal oxide cathode. In terms of the anode, silicon (Si) has received great attention because of its low discharge potential and 10 times greater theoretical capacity than the state-of-the-art graphite. However, the intrinsic hurdle of Si anodes, which is the huge volume expansion (300%) during battery operation, retards the application to the practical LIB. Therefore, the concrete strategies for overcoming the challenge are required in order to improve the energy density with utilizing Si anodes. For over twenty years, the nanoengineering has considerably improved the electrochemical performance of the Si anode by alleviating the intensified stress and strain from the volume change. However, there is a significant gap between the nanoengineered Si anode in academic field and the commercial LIB system in terms of the synthesis of Si anode, the battery manufacturing, and the electrochemical cell design. In this regards, to implement the Si anodes in commercial LIBs, several commercial factors such as the scalability, the rational cost, and performance feasibility, should be considered at the beginning of the development. Accordingly, herein, I have covered a comprehensive review about the co-utilization of graphite and Si anodes for commercial LIBs, the development of high-capacity Si anode for commercial high energy LIB, the benchmarking comparison of industrially-developed Si anode, and finally the remaining issues regarding the practical implementation of Si anode.

In the Chapter 1, the graphite Specifically, the development of the Si anodes would be presented with physicochemical analysis, and the practical utilization of Si anodes for high-energy LIB would be discussed. Furthermore, in order to compare the performance of the developed Si anodes, benchmarking with industrial samples would be conducted with the electrochemical characterization and the failure mechanism analysis.

In chapter 2, the high-capacity Si anodes for commercial high energy LIB is proposed with Fe-Cu-Si composite. FeCuSi is built up with Si nanoparticles and numerous nano-sized metal silicides as a form of a secondary particle. In this design, the micron-sized secondary particle exhibits high tap density which is easy to handle in the battery manufacturing process, and the numerous voids between Si nanoparticles effectively accommodated volume expansion of Si. In addition, the metal silicides such as iron silicide and copper silicide reduced interparticle contact resistance between Si nanoparticles. To investigate the commercial feasibility, the graphite-blended electrode with FeCuSi composite was fabricated under the commercial standard. It exhibited the superior electrochemical

performances compared to industrially developed SiO_x and FeSi anodes.

In chapter 3, the benchmark comparison of industrially developed Si anodes including Si nanolayer-embedded graphite composite, carbon-coated SiO_x , Si-containing graphite/carbon composite, has been presented. The benchmarking comparison was performed in graphite-Si blending system (fixed reversible specific capacity of 420 mAh/g) under the industrial electrode density ($> 1.6 \text{ g/cc}$), areal capacity ($> 3 \text{ mAh/cm}^2$), and a small amount of binder (3 wt%). In addition, the one-to-one comparison has included essential items of both material characterization including laser diffraction particle size analysis, BET surface area, tap density, SEM, and HR-TEM, as well as the electrochemical analysis including half-cell and full-cell tests with measuring electrode volume expansion. As a result, the Si nanolayer-embedded graphite composite exhibited a great compatibility with conventional graphite.

In chapter 4, I discuss the critical issues of the practical implementation of Si anode in high-energy LIBs. The electrochemical cell design has been systematically presented with proper examples. I emphasize that the influence of the electrochemical cell design on the battery performances when aimed at high volumetric energy density. In addition, based on the electrochemical design, the limit on the electrode swelling of Si anodes in terms of energy density is suggested. Furthermore, the origin of differences in the capacity fading between in the half-cell and in the full-cell is carefully figured out. Finally, I propose the potential future direction regarding with the electrode swelling, the capacity fading, and the feasibility study.

Contents

Abstract	
List of Figures	
List of Tables	
List of publications	
Chapter I – Integration of Graphite and Si Anodes for the Commercialization of High-Energy Lithium-Ion Batteries	1
1.1 Introduction	2
1.2 Necessity for co-utilization of graphite and Si in commercial level	3
1.3 Research progress in co-utilization of graphite and Si	9
1.4 Critical factors for co-utilization of graphite and Si	35
1.5 Conclusion and outlook	42
1.6 References	44
Chapter II – Micron-Sized Fe-Cu-Si Ternary Composite Anodes for High Energy Li-ion Batteries	58
2.1 Introduction	59
2.2 Experimental detail	60
2.3 Results and discussion	63
2.4 Conclusion	79
2.5 References	80
Chapter III – One-to-one Comparison of Graphite-blended Negative Electrodes using Silicon Nanolayer-embedded Graphite versus Commercial Benchmarking Materials for High-energy Lithium-ion Batteries	84
3.1 Introduction	85
3.2 Experimental detail	87
3.3 Results and discussion	89
3.4 Conclusion	104
3.5 References	106
Chapter IV – Confronting Issues of the Practical Implementation of Si Anode in High-energy Lithium-ion Batteries	109
4.1 Introduction	110
4.2 Results and discussion	113
4.3 Conclusion and outlook	127
4.4 References	129
Acknowledgements	135

List of Figures

Chapter 1

Figure 1. 1. Schematic illustration for the failure mechanism of Si anodes.

Figure 1. 2. Algorithm of the electrochemical cell design, from the demand of customer to the full-cell assembly/evaluation. Copyright: Elsevier, 2017.

Figure 1. 3. Schematic illustration for graphite/Si anode. The co-utilization of graphite and Si strengthens the advantages and makes up for the weakness of graphite and Si, in short, demonstrating their synergy effects.

Figure 1. 4. The relationship between Si amount in the anode and the specific volumetric capacity, where the electrode includes 5 wt% of binder and no conductive materials. Copyright: Nature Publishing Group, 2016.

Figure 1. 5. Schematic illustration of various synthetic methods for graphite-blended Si anode and graphite/Si composite

Figure 1. 6. SiO_x and Si-metal alloys for graphite-blended Si anode. a) TEM images and selective area electron diffraction patterns (SAED) of granulated SiO_x particle. b) Discharge capacities of graphite-blended SiO_x in full-cell for 200 cycles. Copyright: Elsevier, 2014. c-e) Cross-sectional SEM images of Ti-Si binary alloy@porous Si core-shell (C/S) composites annealed at (c) 600 °C, (d) 700 °C, and (e) 800 °C, respectively. Inset gives the magnified images. f) Discharge capacities versus cycle numbers showing effects of annealing temperature. g) Discharge capacities of blended electrodes including MAE600 and graphite (SG1 and SG2). h) Discharge capacities of blended electrodes including MAE600 and SG1 with various ratio (A: 35/65, B: 45/55, and C: 55/45). Copyright: Elsevier, 2015.

Figure 1. 7. 3M Si alloy (V6) for graphite-blended Si anode. a), b) SEM images of (a) uncalendered and (b) calendered V6 electrodes, respectively. c) Discharge capacities of uncalendered and calendered V6 electrodes. d), e) SEM images of (d) uncalendered and (e) calendered V6/SFG6L electrode, respectively. f) Discharge capacities of uncalendered and calendered V6/MAG-E electrode with different amounts of MAG-E. g) Discharge capacities of uncalendered and calendered V6/MAG-E and V6/SFG6L electrodes. h) Schematic design of cell stack model. Copyright: the Electrochemical Society, 2014.

Figure 1. 8. Porous Si for graphite-blended Si anode. a) Schematic design of porous Si/C-graphite electrode. b) Voltage profiles of porous Si/C-graphite electrode (1:2) at the first cycle. c) Discharge capacities of the calendered porous Si/C-graphite electrode (1:2) in the half-cell. d) Cross-sectional SEM image of porous Si/C particle in calendered electrode. Inset indicates corresponding low magnification SEM image. e) High magnification SEM image of (d). f) Discharge capacities of full-

cell building with $\text{Li}(\text{Ni}_{1/3}\text{Mn}_{1/3}\text{Co}_{1/3})\text{O}_2$ cathode and pre-lithiated anode over 300 cycles. Copyright: Royal Society of Chemistry, 2017.

Figure 1. 9. Fe-Cu-Si ternary composites (FeCuSi). a) Schematic illustration of the structure of FeCuSi and its synthetic process. b) Particle size distribution of FeCuSi. c) SEM image of FeCuSi. d) Magnified cross-sectional HAADF-STEM image of FeCuSi and elemental analysis at Si and metal silicides phase in FeCuSi particle. e) Voltage profiles of graphite-blended FeCuSi and other benchmarking samples (C-SiO_x , and FeSi_2) at the first cycle. f) Discharge capacities and cycling CEs of the graphite-blended anodes for 50 cycles in half-cell configuration. g) Discharge capacities and cycling CEs of the graphite-blended anodes with LiCoO_2 cathode for 300 cycles. Copyright: Royal Society of Chemistry, 2016.

Figure 1. 10. Graphite/Si composite fabricated by ball-milling. a) SEM image of the graphite/Si composites ($\text{C}_{0.8}\text{Si}_{0.2}$). b) HR-TEM image of the ball-milled graphite for 150 h. c) HR-TEM image of the ball-milled $\text{C}_{1-x}\text{Si}_x$ composite. d) HR-TEM image at the surface region of ball-milled $\text{C}_{1-x}\text{Si}_x$ composites. e) Discharge capacities of ball-milled $\text{C}_{1-x}\text{Si}_x$ ($x=0, 0.1, 0.2, \text{ and } 0.25$) and unmilled $\text{C}_{0.6}\text{Si}_{0.4}$. Copyright: the Electrochemical Society, 1998.

Figure 1. 11. Natural graphite/Si/pitch composite by ball-milling. a), b) SEM images of Si-coated natural graphite composites. c) Cross-sectional view of Si-coated natural graphite composites, where the homogeneous and smooth coating layer of Si was formed on the graphite. d) XRD pattern of the natural graphite/Si/pitch composite. e) dQ/dV plots for the 1st and 2nd cycles. f) Discharge capacities in the prototype full-cell system for 300 cycles. Copyright: Elsevier, 2011.

Figure 1. 12. Si/inactive matrix/graphite composites by ball-milling. a) Schematic illustration of fabrication process of Si/SiO_x/C composite. Copyright: Royal Society of Chemistry, 2017. b) Schematic illustration of fabrication process of FeSi₂/Si@C composite. Copyright: American Chemical Society, 2012. c) Schematic illustration of the fabrication process for SiO/Ni/graphite composites. Copyright: Wiley-VCH, 2015. d) Schematic illustration of the synthetic process for nanostructured P-doped Si/graphite composite. Copyright: American Chemical Society, 2017.

Figure 1. 13. Graphite/Si composites fabricated by spray drying. a), b) SEM and TEM image of graphite/Si@reGO composite. Copyright: Elsevier, 2013. c) SEM image of Si/C composites. d) Magnified cross-sectional image of Si/C composites. e) Discharge capacities and cycling CEs of Si/C composites, demonstrating its comparability with that of graphite. Copyright: Elsevier, 2014. f) SEM image of Si/G/PDA-C composites. g) EDS mapping image of N for Si/G/PDA-C composites depicting the presence of the polydopamine on the surface. h) Discharge capacities of Si/G and Si/G/PDA-C composites. Copyright: Elsevier, 2016.

Figure 1. 14. Si/C microspheres fabricated by spray drying with Si nanoparticles and ball-milled flake graphite. a) Schematic illustration of the overall structure of watermelon-inspired Si/C microsphere. b) SEM image of hierarchical buffer structured Si/C microspheres. The inset gives the magnified SEM

image of the single microparticle. c) Voltage profiles of Si/C microspheres at the first cycle. d) Areal capacities of Si/C microspheres for 500 cycles. Copyright: Wiley-VCH, 2017.

Figure 1. 15. Graphite/Si composites fabricated by CVD. a), b) SEM images of (a) pristine MCMB and (b) Si-coated MCMB. c) Raman spectra of pristine and Si-coated MCMB. d) Discharge capacities with different treating temperatures of Si coating on MCMB. Copyright: Elsevier, 2004.

Figure 1. 16. copper silicide-coated graphite fabricated by PECVD and RF magnetron sputtering. a-c) SEM images showing the surface of (a) raw graphite, (b) Si-coated graphite, (c) copper silicide-coated graphite, respectively. d) AC current plot the conductivity for raw graphite, Si-coated graphite and copper silicide-coated graphite. e), f) XPS spectra of copper silicide-coated graphite for (e) Cu 2p and (f) Si 2p. (g) Discharge capacities of raw graphite, Si-coated graphite and copper silicide-coated graphite for 30 cycles. Copyright: Elsevier, 2006.

Figure 1. 17. Si-nanolayer-embedded graphite/carbon (SGC) composite. a) Schematic illustration of the fabrication process of SGC composite. b) Photograph of the fabricated SGC composite per batch. c) Cross-sectional STEM image for EDS mapping of SGC composite. d) Discharge capacities of SGC composite for 100 cycles, containing PG, SG, 9wt% SGC, and B-Si/G. e,f) Captured *in situ* TEM images for expansion of Si (e) on the surface of empty space and (f) between graphite layer, respectively. Copyright: Nature Publishing Group, 2016.

Figure 1. 18. The optimized structure of Si/carbon/graphite composite *via* liquid solidification method. a-c) SEM images with schematic morphologies for composites according to the different mixing order of Si, graphite, and pitch. d) Electrochemical cycle performance showing the effect of mixing order of Si, graphite, and pitch. Copyright: the Electrochemical Society, 2006.

Figure 1. 19. Graphite/Si composites fabricated by liquid solidification method. a) HR-TEM image at the interfacial region of Si-C-G composites. b) HR-TEM image at the boundaries between Si and amorphous carbon coating layer of Si-C-G composites, with FFT patterns (inset). Copyright: American Chemical Society, 2016. c) Schematic illustration of fabrication process for the nano-Si/pitch/graphite composite. d) Discharge capacities of the nano-Si/pitch/graphite composite for 1200 cycles. e) Voltage profiles of the prototype full-cells at 1st, 200th, 600th, 1000th, and 1200th cycles. Copyright: Royal Society of Chemistry, 2018.

Figure 1. 20. Critical factors for designing graphite/Si composite and graphite-blended Si anode.

Figure 1. 21. Electrochemical characterization of SSP/G, LSG, and CSG. a) Voltage profiles at the first cycle measured at 0.1 C. b) Discharge capacities and cycling CEs of the anodes for 50 cycles. c) Magnified CEs at each cycle plotted from 98 to 100% of (b). d) Change of electrode thickness at lithiated state during 50 cycles.

Figure 1. 22. SEM images of electrode changes before and after 50 cycles regarding SSP/G, LSG, and

CSG. a-f) Cross-sectional views before cycling and after 50 cycles with magnified images.

Figure 1. 23. A Schematic illustration of electrode swelling behavior depending on Si distribution.

Chapter 2

Figure. 2. 1. Schematic illustrations of FeCuSi and its synthesis. (a) Simplified two-dimensional cross-section view of FeCuSi. Silicon nanoparticles build up the secondary particle with metal silicides which can improve electrical conductivity and structural stability. (b) Fabrication process of FeCuSi.

Figure. 2. 2. Characterization of FeCuSi. (a) SEM image of FeCuSi. (b) Magnified cross-sectional SEM images of FeCuSi. (c) Statistical analysis for the size distribution of FeCuSi. (d) Volume comparison between 1 g of FeCuSi and conventional Si nanoparticles after measuring tap density. (e) X-ray diffraction patterns of FeCuSi as a function of heating temperature.

Figure 2. 3. SEM image of amorphous silicon nanoparticles which were synthesized through chemical vapor deposition (CVD) of monosilane (SiH_4).

Figure 2. 4. Pore size distribution of FeCuSi. The derivative volume with respect to the pore diameter shows where clusters of pores of a particular diameter occur.

Figure 2. 5. Crystallite sizes of FeCuSi with different heating temperatures.

Figure. 2. 6. Detailed investigation of FeCuSi with TEM analysis. (a) HAADF-STEM image and EDS mapping of FeCuSi in cross sectional view. Cyan, red, and yellow indicate Si, Fe, and Cu respectively. (b) Magnified HAADF-STEM image of FeCuSi and EDS point analysis for Si nanoparticle, iron silicide, and copper silicide.

Figure 2. 7. EDS line scan of FeCuSi. (a) Magnified HAADF-STEM image of FeCuSi. (b) Element profile according to line scanning in (a).

Figure 2. 8. Electrochemical characterization of FeCuSi with benchmarking samples in half-cell. (a) Voltage profiles of FeCuSi, C-SiO_x, and FeSi₂ at the formation cycle. (b) Reversible capacities of FeCuSi, C-SiO_x, and FeSi₂ for 50 cycles. The formation cycle (a) and cycling test (b) were carried out at a rate of 0.1C and 0.5C, respectively. (1C was set as 1.3 A/g, 1.1 A/g and 1.7 A/g for FeCuSi, C-SiO_x, and FeSi₂, respectively.) All electrochemical tests were performed at 25 °C in 2032R coin-type cell.

Figure 2. 9. Optimization for heating temperature of FeCuSi. (a) Reversible capacities of FeCuSi as a function of heating temperature. (b) Coulombic efficiencies of FeCuSi with diverse heating temperature. FeCuSi with 860 °C of heating temperature was optimized one.

Figure 2. 10. Electrochemical characterization of FeCuSi anode with benchmarking samples in half-cell (a, b) and full-cell (c, d) and measurement of the thickness change of electrode (e). (a) Voltage profiles of FeCuSi, C-SiO_x, and FeSi₂ at the formation cycle. (b) Reversible capacities and cycling CEs of FeCuSi, C-SiO_x, and FeSi₂ for 50 cycles. The formation cycle (a) and cycling test (b) in half-cell were carried out at a rate of 0.1C and 0.5C, respectively. (1C = 0.42 A/g.) (c) Voltage profiles of full-cell systems with LCO and different anodes of FeCuSi, C-SiO_x, and FeSi₂ at the formation cycle. (d) Reversible capacities and cycling CEs of the full-cells for 300 cycles with 1C. The formation cycle (c) and cycling test (d) in full-cell were carried out at a rate of 0.1C and 1C, respectively. (1C = 3.0 mA/cm²) All electrochemical tests were performed at 25 °C in 2032R coin-type cell. (e) The change of electrode thickness of graphite, FeCuSi, C-SiO_x, and FeSi₂ at lithiated state during 30 cycles. Electrode thickness at the lithiation state were measured with a micrometer after disassembling coin cells in Ar-filled glove box.

Figure 2. 11. Electrochemical properties of LCO. (a) Voltage profile of LCO at the formation cycle. (b) Reversible capacities of LCO for 100 cycles with 0.5C. The formation cycle (a) and cycling test (b) were carried out at a rate of 0.1C and 0.5C, respectively. (1C = 0.18 A/g) All electrochemical test were performed at 25 °C in 2032R coin-type cell.

Figure 2. 12. Various voltage profiles of FeCuSi (a), C-SiO_x(b), and FeSi₂(c) plotted for 1st, 100th, 200th, and 300th cycle.

Chapter 3

Figure 3. 1. Material characterization of pristine SGC and benchmarking samples. Benchmarking comparison for physical properties with a) particle size distribution, citing D10, D50, and D90, b) specific surface area based on BET theory, and c) tap density after mechanically tapping a container. Morphological comparison of C-SiO_x (d-g), Si-G/C (h-k), and SGC (l-o), using SEM images with top and cross-sectional views, EDS mapping from cross-sectional views, and HR-TEM images of the interfacial regions. SEM images (d, h, l) and HR-TEM images (g, k, o) include insets depicting magnified images and FFT analyses, respectively.

Figure 3. 2. Electrochemical evaluation of C-SiO_x, Si-G/C, and SGC in half-cell. a) Voltage profiles at the first cycle. b) Cycling performances at the charge/discharge rate of 0.5C with CE plots for 50 cycles. c-e) Various voltage profiles of C-SiO_x (c), Si-G/C (d), and SGC (e) at second, tenth, and fiftieth cycle.

Figure 3. 3. Electrochemical evaluations of G/C-SiO_x, G/Si-G/C, and G/SGC in half-cell. a) Voltage profiles at the first cycle. corresponding to the battery formation process. b) Discharge capacities and CEs of the anodes cycled at 0.5C for 100 cycles. c) Rescaled form of CE at each cycle from 99 to 100%.

d-f) Various voltage profiles of (d) G/C-SiO_x, (e) G/Si-G/C, and (f) G/SGC at the first, fiftieth, and hundredth cycle.

Figure 3. 4. Electrochemical performances of high-voltage LCO in half-cell. a) Voltage profile at the first cycle. b) Cycling performances at the charge/discharge rate of 0.5C. c) Voltage profiles at second, fiftieth, and ninetieth cycle. The surface modified LCO was used to improve structural stability even beyond 4.45 V. It showed high reversible specific capacity of 183 mAh/g with first cycle CE of 97.9% and capacity retention of 92.1% at ninetieth cycle in the voltage range of 4.45-3 V.

Figure 3. 5. Electrochemical performances of G/C-SiO_x, G/Si-G/C, and G/SGC in the prototype full-cell high-energy-density batteries. a) Voltage profiles of the prototype full cells at the first formation cycle. b) Cycling performances at the charge/discharge rate of 0.5C with CE plots for 400 cycles. Inset shows magnified areal capacity versus cycle number plotted for the early cycles. c) Rescaled form of CE at each cycle from 99 to 100% for 100 cycles. d-f) Voltage profiles of the prototype full cells at the first, hundredth, two-hundredth, and four-hundredth cycle.

Figure 3. 6. Electrode volume expansion after cycling and estimation of volumetric energy density. a-l) SEM images of the electrodes composed of (a-d) G/C-SiO_x, (e-h) G/Si-G/C, and (i-l) G/SGC from top and cross-sectional views, describing the structural change of the electrodes before and after the cycling. m) *ex-situ* measurement of electrode volume expansion after cycling. n) Volumetric energy densities before and after 400 cycles.

Figure 3. 7. Morphological changes of (a-d) SiO_x, (e-h) Si-G/C, and (i-l) SGC in the graphite-blended electrode after 400 cycles. a, e, i) SEM images of the Si composite on the electrodes cycled for 400 cycles. b, f, j) Cross-sectional images of SiO_x, Si-G/C, and SGC after 400 cycles with EDS mapping (c, g, k). F, C, and Si are indicated by yellow, green, and red, respectively. d, h, l) HR-TEM images at the interfacial region.

Chapter 4

Figure 4. 1. Overview of the challenges and representative strategies associated with the Si anode. (a) Intrinsic properties of Si disadvantageous to charge transfer kinetics and to stable cycling behavior. (b) Unfavorable phenomena in the Si anode causing the active material loss and consumption of lithium ion in the cell. (c) Various representative strategies for addressing the unfavorable phenomena such as size control, surface coating, active/inactive alloy, void space engineering, and composite.

Figure 4. 2. Flow chart of the electrochemical cell design. The brief procedure of the electrochemical cell design is presented from the customer demand, such as cell dimension and structure, to the full-cell

assembly/evaluation.

Figure 4. 3. Photographs of the pouch-type full-cell with the cell capacity of 1.2 Ah. (a) Double-sided cathode and anode for stack type pouch cell. (b) Stacking type pouch cell with the dimension of 70 mm * 90 mm * 2.5 mm. (c) Cross sectional photograph of the pouch cell.

Figure 4. 4. The relationship between the energy density and the electrode swelling and the measurement of the electrode swelling. (a) Energy density plot of Graphite/HVLCO and graphite-blended Si anode/HVLCO full-cells as a function of the electrode swelling. (b) The limits of electrode swelling in different specific capacities of graphite-blended Si anode where the energy density of graphite-blended Si anode and graphite become the same. The electrode swelling of graphite is set as 20%. (c) Electrode porosity versus electrode density in graphite. The electrode porosity is estimated with the true density of graphite, binder, and conductive agents. (d) *Ex situ* measurement of the electrode swelling by micrometer and microscope. (e) *In situ* measurement of the electrode swelling with electrochemical dilatometry.

Figure 4. 5. The causes of the difference in the capacity fading between the half-cell and the full-cell. (a) Contrasting lithium sources in the half-cell and in the full-cell. The cyclable lithium is infinitely supplied from the lithium metal in the half-cell, whereas the supply is limited to the capacity of the cathode in the full-cell. (b) Different voltage behaviors between the half-cell and the full-cell. While the cut-off voltages and SOC are fixed with the lithium metal reference/counter electrode, the cut-off voltages and SOC shift as a result of the degradation. (c) The difference in the amounts of the electrolyte for the coin-type half-cell and for the commercial full-cell such as a pouch-type cell. The coin-type cell for the half-cell test is generally filled with the excessive amount of the electrolyte, on the other hand, the commercial cell such as pouch-type cell contains the limited amount of the electrolyte.

List of Tables

Chapter 1

Table 1. 1. Parameters of various Si anodes regarding the volumetric energy density

Chapter 2

Table 2. 1. The peak list of Fe, Cu, Si, FeSi₂, and Cu_{3,17}Si with the index from the XRD analysis. The references of Fe, Cu, Si, FeSi₂, and Cu_{3,17}Si are ICSD 631729, 627117, 43403, 24360, 160694, respectively.

Table 2. 2. Summary of electrochemical performance of FeCuSi and benchmarking samples

Chapter 3

Table 3. 1. Battery testing protocols for the half-cell and the full-cell.

Table 3. 2. Volumetric energy density estimation

Table 3. 3. Summarized electrochemical performances of C-SiO_x, Si-G/C, and SGC in half- and full-cell

Chapter 4

Table 4. 1. Detailed electrochemical cell designs for graphite and graphite-blended Si anodes

List of publications

I contributed to the following publications during my PhD course.

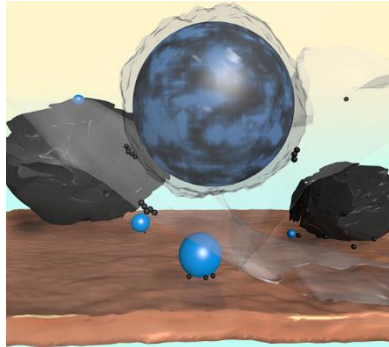
Peer-reviewed publications

1. Nam, G.; Son, Y.; Park, S. O.; Jeon, W. C.; Jang, H.; Park, J.; Chae, S.; Yoo, Y.; Ryu, J.; Kim, M. G., A Ternary Ni₄₆Co₄₀Fe₁₄ Nanoalloy-Based Oxygen Electrocatalyst for Highly Efficient Rechargeable Zinc–Air Batteries. *Adv. Mater.* **2018**, 1803372.
2. Han, J.-G.; Lee, J. B.; Cha, A.; Lee, T. K.; Cho, W.; Chae, S.; Kang, S. J.; Kwak, S. K.; Cho, J.; Hong, S. Y., Unsymmetrical fluorinated malonatoborate as an amphoteric additive for high-energy-density lithium-ion batteries. *Energ Environ Sci* **2018**.
3. Lee, M.-J.; Lho, E.; Bai, P.; Chae, S.; Li, J.; Cho, J., Low-temperature carbon coating of nanosized Li_{1.015}Al_{1.006}Mn_{1.925}O₄ and high-density electrode for high-power Li-Ion batteries. *Nano letters* **2017**, 17 (6), 3744-3751.
4. Kim, N.; Chae, S.; Ma, J.; Ko, M.; Cho, J., Fast-charging high-energy lithium-ion batteries via implantation of amorphous silicon nanolayer in edge-plane activated graphite anodes. *Nature communications* **2017**, 8 (1), 812.
5. Chae, S.; Ko, M.; Kim, K.; Ahn, K.; Cho, J., Confronting issues of the practical implementation of Si anode in high-energy lithium-ion batteries. *Joule* **2017**, 1 (1), 47-60.
6. Chae, S.; Kim, N.; Ma, J.; Cho, J.; Ko, M., One-to-One Comparison of Graphite-Blended Negative Electrodes Using Silicon Nanolayer-Embedded Graphite versus Commercial Benchmarking Materials for High-Energy Lithium-Ion Batteries. *Adv. Energy Mater.* **2017**, 7 (15), 1700071.
7. Ko, M.; Chae, S.; Ma, J.; Kim, N.; Lee, H.-W.; Cui, Y.; Cho, J., Scalable synthesis of silicon-nanolayer-embedded graphite for high-energy lithium-ion batteries. *Nature Energy* **2016**, 1 (9), 16113.
8. Chae, S.; Ko, M.; Park, S.; Kim, N.; Ma, J.; Cho, J., Micron-sized Fe–Cu–Si ternary composite anodes for high energy Li-ion batteries. *Energ Environ Sci* **2016**, 9 (4), 1251-1257.
9. Son, Y.; Son, Y.; Choi, M.; Ko, M.; Chae, S.; Park, N.; Cho, J., Hollow silicon nanostructures via the Kirkendall effect. *Nano letters* **2015**, 15 (10), 6914-6918.
10. Liu, X.; Liu, W.; Ko, M.; Park, M.; Kim, M. G.; Oh, P.; Chae, S.; Park, S.; Casimir, A.; Wu, G., Metal (Ni, Co)-metal oxides/graphene nanocomposites as multifunctional electrocatalysts. *Adv. Funct Mater.* **2015**, 25 (36), 5799-5808.
11. Liu, W.; Oh, P.; Liu, X.; Lee, M. J.; Cho, W.; Chae, S.; Kim, Y.; Cho, J., Nickel-rich layered lithium transition-metal oxide for high-energy lithium-ion batteries. *Angewandte Chemie International Edition* **2015**, 54 (15), 4440-4457.
12. Ko, M.; Oh, P.; Chae, S.; Cho, W.; Cho, J., Considering Critical Factors of Li-rich Cathode and Si Anode Materials for Practical Li-ion Cell Applications. *Small* **2015**, 11 (33), 4058-4073.

13. Ko, M.; Chae, S.; Cho, J., Challenges in accommodating volume change of Si anodes for Li-ion batteries. *ChemElectroChem* **2015**, *2* (11), 1645-1651.
14. Park, M.-H.; Noh, M.; Lee, S.; Ko, M.; Chae, S.; Sim, S.; Choi, S.; Kim, H.; Nam, H.; Park, S., Flexible high-energy Li-ion batteries with fast-charging capability. *Nano letters* **2014**, *14* (7), 4083-4089.
15. Ko, M.; Chae, S.; Jeong, S.; Oh, P.; Cho, J., Elastic α -silicon nanoparticle backboned graphene hybrid as a self-compacting anode for high-rate lithium ion batteries. *Acs Nano* **2014**, *8* (8), 8591-8599.
16. Kim, C.; Ko, M.; Yoo, S.; Chae, S.; Choi, S.; Lee, E.-H.; Ko, S.; Lee, S.-Y.; Cho, J.; Park, S., Novel design of ultra-fast Si anodes for Li-ion batteries: crystalline Si@ amorphous Si encapsulating hard carbon. *Nanoscale* **2014**, *6* (18), 10604-10610.

Chapter 1

Integration of Graphite and Si Anodes for the Commercialization of High-Energy Lithium-Ion Batteries



Abstract: Silicon (Si) has been considered as the most promising anode material for overcoming the theoretical capacity limit of a carbonaceous anode. Since the implementation of nanotechnology on Si anode, the significant progress has been made as addressing severe volume change during (de)lithiation. However, the practical application of Si anodes in commercial lithium-ion batteries (LIBs) has been still stagnant. Nowadays, with the drastic increase in energy demands of diverse industries, co-utilization of Si and graphite has resurfaced as the commercially viable method for realizing high energy. Herein, we highlight the necessity for the co-utilization of graphite and Si in terms of the commercialization, and carefully review the development of graphite/Si anodes. Representative Si anodes implemented in the graphite-blended electrode are covered and a variety of strategies for building graphite/Si composites are organized according to their synthetic method. Particularly noteworthy, the critical factors for the co-utilization of graphite and Si are systematically presented. Finally, we provide insightful suggestions with regard to the co-utilization of graphite and Si for the commercialization.

Chapter 1 will be submitted to “Angewandte Chemie” in Dec. 2018.

1. 1. Introduction

Since the first commercialization of Li-ion batteries (LIBs), LIBs have been played an essential role in providing power to diverse cordless electric devices.¹⁻⁴ The enormous interest on high-tech electrical vehicles and electronics have constantly stimulated to improve the energy density of LIB.⁵⁻⁷ As the battery technology regarding manufacturing process and material science has grown into maturity, the energy density has been marvelously increased. However, the conventional LIB system, which is comprised of lithium transition metal oxide and a carbonaceous material as cathode and anode respectively, is now facing the theoretical limit of the energy density. Therefore, the progress of LIB system through the material paradigm shift from conventional intercalation chemistry becomes highly desired for the further improvement of energy density.⁸⁻¹²

Among the alloy-type anode, Si has been vigorously investigated as one of the most promising active materials because of its ten times higher gravimetric capacity than that of conventional graphite (3579 mAh g⁻¹ for Si and 372 mAh g⁻¹ for graphite).¹³⁻¹⁶ Its abundance and low working voltage (~0.2 V vs. Li/Li⁺) consolidate a preeminent position as a next-generation anode.¹⁷⁻¹⁹ However, its direct utilization is hampered by the huge volume change of Si (> 300%) during (de)alloying with Li, which causes fracture of Si and electrode deformation with swelling (**Fig. 1.1**).²⁰⁻²³ The pulverization of Si caused by its repeated fracture accompanies the electrical isolation.²⁴ In addition, the ceaseless side reaction with electrolytes occurs at the newly exposed surface and consumes confined Li⁺ ions, resulting in the excessive formation of solid electrolyte interphase (SEI) layer during cycling.²⁵⁻²⁷ Consequentially, the accumulated SEI layer increases the internal resistance of the cell.²⁸⁻²⁹ From these unfavorable phenomena from severe volume change, the electrochemical performances of Si anode are significantly deteriorated.^{28, 30-31} Besides, with respect to the electrode level, the rearrangement of the components in the electrode would bring about the electrical isolation of Si by the disconnection from the current collector.^{18, 32} The electrode swelling could also squeeze the electrolyte filled in the pore of the separator, which blocks the transportation of Li-ion.³³ Even worse, the severe electrode swelling causes the bulge of the cell package, which raises the safety concern.³⁴

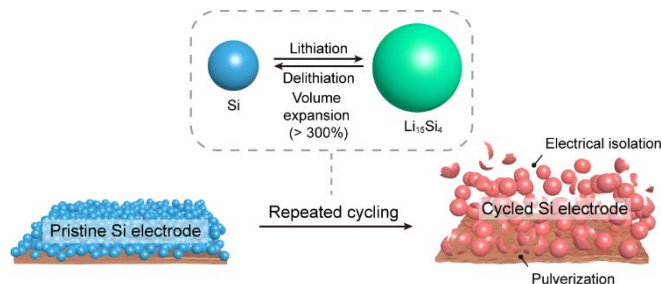


Figure 1. 3. Schematic illustration for the failure mechanism of Si anodes.

To address the issue of severe volume expansion, numerous efforts have been devoted to investigating the electrochemical and the mechanical behaviors of Si anode. Notably, reducing the particle size of Si to nano-size can prevent the crack evolution by alleviating the stress/strain, leading to the era of nano-structuring.^{20, 35-36} A variety of nano-engineered Si anodes, such as nanoparticles,³⁷⁻³⁸ nanowires,³⁹ nanotubes,⁴⁰ and void-contained structures like yolk-shell,⁴¹⁻⁴⁴ have achieved significant improvement in cycling stability.⁴⁵ With these promising strategies, the practical application for high-energy LIB has been regarded as next agenda. Several studies have reported their industrial feasibilities with their scalable synthesis, high tap density, high-mass loading, high electrode density, improved volumetric energy density and so on.^{35, 42, 46-48} However, the sole utilization of Si is regarded as practically difficult to improve the volumetric energy density because of their large requirements of binder and conductive agent and severe electrode swelling.^{10, 49} In this regards, the co-utilization of graphite, which is the most popular anode among various carbonaceous materials, and Si have been deemed as the best method for the current commercial LIB system to realize high-energy cell with Si anode.⁴⁹⁻⁵² The co-utilization would combine the established battery technology of the graphite anode with the innovative development of Si anodes, making a synergy.

In contrast to the previous reviews about Si anodes which mainly focused on the nanostructures of Si,⁵³⁻⁵⁵ herein, we will first cover the co-utilization of graphite and Si anodes for the commercialization of high-energy LIB. First of all, the necessity for the co-utilization of graphite and Si will be discussed in the practical point of view. Then, we will systematically review the graphite/Si anode for high volumetric energy density, specifically divided into the graphite-blended Si anode and the graphite/Si composite anode. Besides, the critical considering factors for the development of graphite/Si anodes will be presented deliberately with the simple experimental demonstration.

1. 2. Necessity for co-utilization of graphite and Si in commercial level

For decades, the battery research is constantly aiming at reducing the size/weight of battery, increasing the energy of battery with low cost,⁵⁶⁻⁵⁷ and extending the cycle life.^{10, 58} The pioneering work on the innovative anode materials has received attention by demonstrating marvelously improved specific capacity and stable cycling behaviors. However, since the criticism about the true performance metric for electrochemical energy storage in 2010,⁵⁹ there have been several concerns over the prevalent testing protocol in numerous literature, which just maximizes the electrochemical performances.^{11, 56, 60}

Considering the practical battery application with limited space, the volumetric energy density is much more comprehensive performance metric than the specific capacity which has been usually adopted in the academic field.⁵⁹⁻⁶⁰ The volumetric energy density is defined as the amount of energy stored in a battery per unit volume, thereby including all the battery components. To improve the

volumetric energy density, the development in the electrochemical cell design factors, such as the areal capacity, electrode density, electrode swelling, and average voltage, should be enhanced instead of just increasing the specific capacity (**Fig. 1. 2**). Improving the volumetric energy density is practically hindered by the influence of the factors on the battery performance such as cycle life and rate capability. Therefore, the imprudent increase of the cell design factor can deteriorate the battery performance and even lower the volumetric energy density as well.¹⁰ The innovative active material can overcome the limit of those factors and achieve high volumetric energy density along with great performances.^{47, 49}

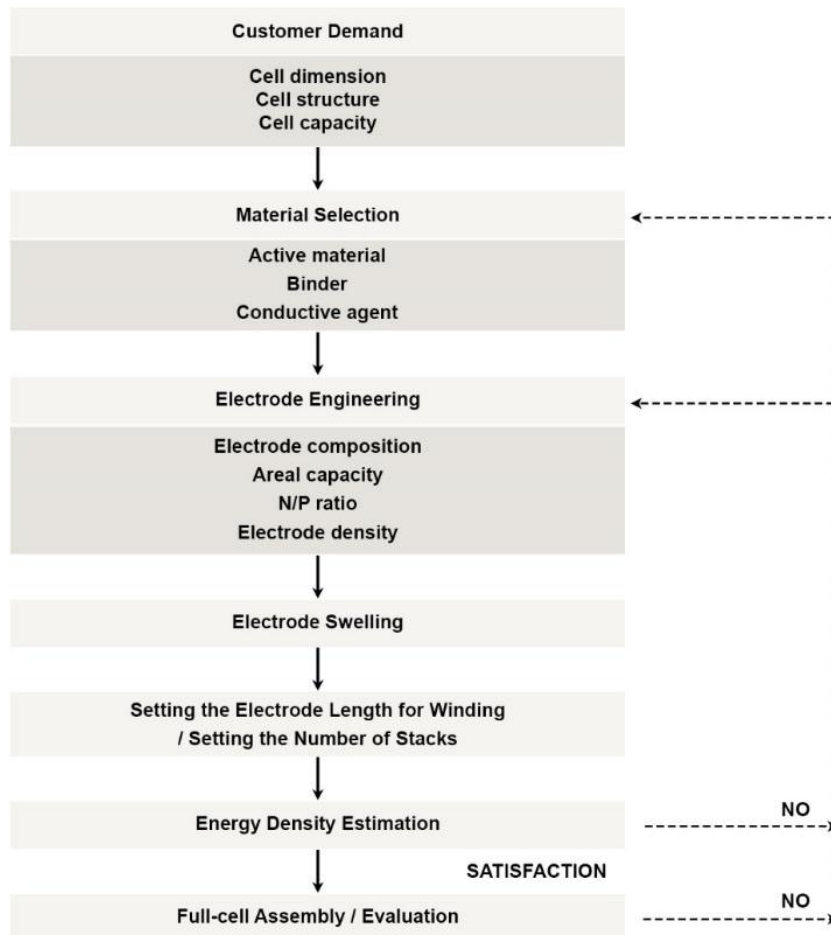


Figure 1. 4. Algorithm of the electrochemical cell design, from the demand of customer to the full-cell assembly/evaluation. Copyright: Elsevier, 2017.

Recently, as an investigation for the commercial viability, several studies focus on areal capacity with high mass loading or high electrode density. However, they focused on the particular factor, and frequently miss the other key factors for estimating volumetric energy density, such as areal capacity (or areal current density), loading level, electrode thickness, electrode density, electrode swelling, and average voltage. We summarized the information of various Si anodes for recent three years (**Table 1.1**). We noted several values by the range depending on the different electrode fabrication for specific electrochemical testing.

Because of the scarce information regarding the average voltage of Si anodes and the difference in the cathode for the full-cell systems, the comparison of the volumetric energy density can be guessed with the areal capacity (mAh/cm^2), the volumetric capacity (mAh/cc), and the electrode swelling (%). The areal capacity reflects the volume/mass fraction of other battery components. In other words, it indicates that the high areal capacity decreases the volume/mass fraction of other components, thus leading to increase in the volumetric energy density. The volumetric capacity implies how densely the electrode is fabricated with specific capacity, and the electrode swelling shows how much the electrode would occupy additional volume during cycling. The high volumetric energy density can be obtained when improving all these electrochemical design factors together. For the commercial graphite as a standard, it is acknowledged that the areal capacity, the volumetric capacity, and the electrode swelling are about $3.3 \text{ mAh}/\text{cm}^2$, about $570 \text{ mAh}/\text{cc}$ ($360 \text{ mAh}/\text{g}$ for the specific capacity and $1.6 \text{ g}/\text{cc}$ for the electrode density), and maximum 20%, respectively.

Unfortunately, the majority of Si anodes without graphite demonstrated high specific capacity, however they didn't get high areal capacity and high volumetric capacity at the same time. Owing to the electrode instability from severe volume expansion and low electrical conductivity of Si anodes, achieving high areal capacity by high mass loading could bring about poor battery performances, and the severe side reactions of Li counter electrode at high current density could shorten the cycle life drastically in the half cell. In addition, there is no information about electrode thickness or electrode density for some of Si anodes, such as Mesoporous a-Si,⁶¹ Si nanosheet,⁶² Si/CNT/BTO,⁶³ RGO-SiNPs,⁶⁵ and d-SiO@vG.⁷¹ For these anodes, it is difficult to judge the progress in the volumetric energy density in spite of their superior performance in the report.

On the other hand, the Si anodes where the graphite was co-utilized, such as Fe-Cu-Si,⁴⁸ SGC,⁴⁷ Watermelon Si/C,⁶⁷ SEAG,⁶⁸ Porous Si-C/graphite,⁵² and blocky SiO_x/C,⁷⁷ succeeded in demonstrating the high areal capacity and the high volumetric capacity at the same time, leading to certain progress in the volumetric energy density. Although the co-utilization of graphite brings about relatively low specific capacity, graphite has multiple advantages in a compatibility with Si anodes for the commercialization. Graphite is a well-established commercial anode material with great

electrochemical performances such as low irreversible capacity, robust cycle life, good rate capability, low volume expansion upon lithiation (~10%), and high electrical conductivity.^{8, 78-79} In this regard, making a sacrifice of specific capacity, the addition of graphite can compensate the defect of Si anode by imparting electrical conductivity to the Si anode,⁸⁰⁻⁸¹ mitigating the severe electrode swelling with its low volume change, and improving almost the whole electrochemical performances even with its low prices (**Fig. 1. 3**).⁸² In addition, the slippery and deformable properties of graphite allow the graphite/Si anode to be easily calendered for high electrode density with preventing severe damage of brittle Si, which effectively improves the volumetric energy density.^{9, 49} Finally, the most attractive advantage for the commercialization in the near future is that the co-utilization of graphite and Si anode is readily adaptable to the established battery manufacturing process which numerous efforts and huge financial investment have been already dedicated to.^{12, 57}

Improving the volumetric energy density with only Si anode is considered as theoretically impossible due to the significant volume expansion of Si. Recently, the theoretical limit of energy density in graphite/Si anode was investigated with a rational model. The theoretical model is based on the practical standard that the increase in the external dimensions of LIB is not allowed beyond 5% of the swelling limit. Depending on the anode porosity at lithiated state and the amount of conductive material and binder, the weight fraction of Si for the highest energy density can be changed, but its maximum value is limited to only 11.68 wt% in the ideal case (no conductive material and binder, and 0% anode porosity at lithiated state). The relationship between volumetric capacity and the weight fraction of Si is presented in **Figure 1. 4** as an example.⁵¹ In this regard, co-utilizing graphite and Si is a rational way to improve the energy density instead of using Si anode only.

Active materials	Graphite-included	Specific capacity (mAh g ⁻¹)	Initial CE (%)	Electrode composition ^[a] (AM:BM:CM)	Areal capacity (mAh cm ⁻²)	Loading level (mg cm ⁻²)	Electrode thickness (μ m)	Electrode density (g cc ⁻¹)	Electrode swelling (%)
Mesoporous a-Si ⁶¹	none	1679	64.6	60:15:25	1.24	0.7-1.2	-	-	-
Si nanosheet ⁶²	none	1780	79.4	70:15:15	-	-	-	-	-
Si/CNT/BTO ⁶³	none	2204	86.2	90:10:0	-	-	-	-	-
Si/carbon/graphite ⁶⁴	included	712	79.8	80:10:10	-	1.5	30	-	16.7% @ 1 cycle and 33.3% @50 cycles
RGO-SiNP _s ⁶⁵	none	1957	58	-	2.48	2.5	-	-	-
Fe-Cu-Si ⁴⁸	included	1287	91	80:10:10 for sole Si anode and 97:3:0 for graphite-blended electrode	1-3.44	1 for sole Si anode and 8.5 for graphite-blended electrode	-	1.6	49% @ 30th cycle for graphite-blended electrode
SiMP@Gr ⁶⁶	none	~3300	93.2	90:10:00	4.5	0.8-2.5	15 (for 0.8 mg cm ⁻²)	-	11% @10 cyc
SGC ⁴⁷	included	517	92	95.8:3.2:1	3.3	6.5	42	1.6	38% @100cyc
Watermelon Si/C ⁶⁷	included	620	89.2	90:5:5	2.54	4.1	37	1.1	30% @100cyc
SEAG ⁶⁸	included	525	93.8	96:3:1	3.5	-	-	1.6	-
Porous Si-C/graphite ⁵²	included	~650	65	75:20:5	2.5-3	-	32	~1.2	56% @ 200 cyc
Silicene flower ⁶⁹	none	2000	74	80:10:10	-	0.9-1.5	13	-	7% @ 100 cyc
Si@TiO ₂ ⁷⁰	none	~1562	65.8	70:15:15	-	0.8-2.1	14.7	1.4	-
d-SiO@vG ⁷¹	none	1600	X(~75%)	75:15:10	1.4	1.5	-	-	-
Si-PBI ⁷²	none	2133	60.27	80:10:10	-	-	17	-	64.7% @ 80 cyc
Si-SiO _x -C composite ⁷³	none	1561.9	80.2	60:20:20	-	1	16.8	-	18% @ 100cyc
raspberry-like HSi@C ⁷⁴	none	1032.6	52.4	70:10:20	-	0.7-2.67	25	0.4~0.66	-
Mesoporous Si from zeolite ⁷⁵	none	1031-1184	73.1-73.7	80:10:10	-	1.0-2	15-40	0.67, 0.75	5.7% for sole Si, 7.1% for graphite-blended electrode
SiSPC ⁷⁶	none	3154	81.4	60:20:20 or 52.5:30:17.5	-	0.6-2.54	12.6	-	320%
blocky SiO _x /C ⁷⁷	included	645	82.2	90:5:5	-	3.5	35	1.3	37.1% @ 10 cycle

Table 1.1. Parameters of various Si anodes regarding the volumetric energy density

[a] AM: Active material; BM: Binder; CM: Conductive material

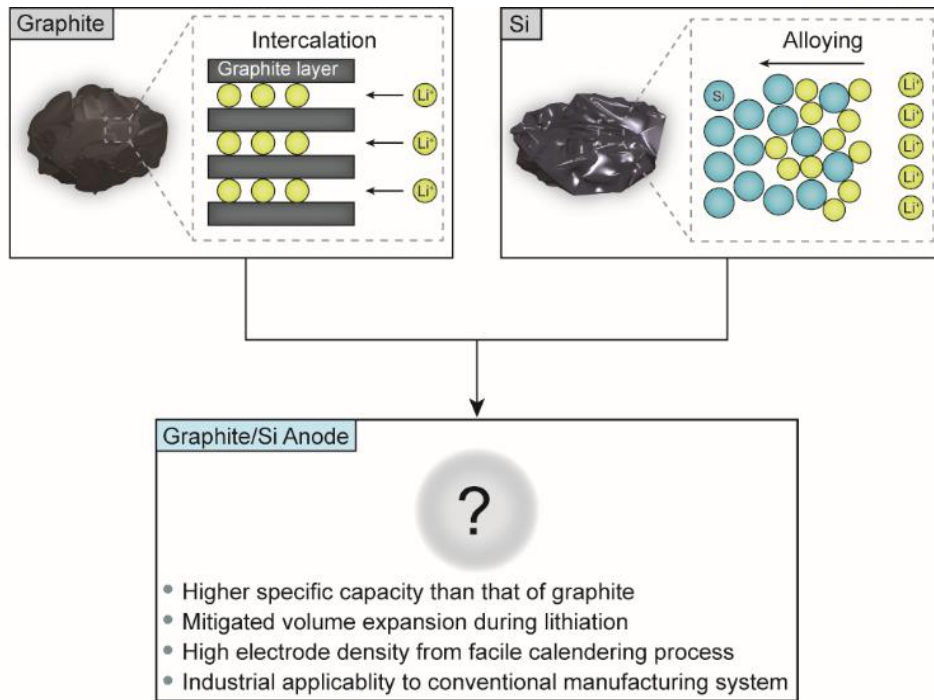


Figure 1. 3. Schematic illustration for graphite/Si anode. The co-utilization of graphite and Si strengthens the advantages and makes up for the weakness of graphite and Si, in short, demonstrating their synergy effects.

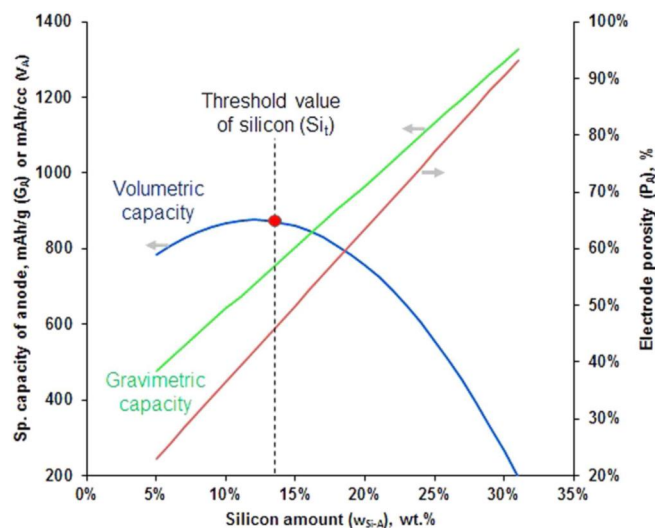


Figure 1. 4. The relationship between Si amount in the anode and the specific volumetric capacity, where the electrode includes 5 wt% of binder and no conductive materials. Copyright: Nature Publishing Group, 2016.

1. 3. Research progress in co-utilization of graphite and Si

The co-utilization of graphite and Si can be carried out by blending the high-capacity Si anode with graphite in the electrode fabrication process or building the single graphite/Si composite (Fig. 1. 5). In this section, we have reviewed the research progress of graphite-blended Si anode and graphite/Si composite with diverse studies. The following extensive discussion on the research progress will allow researchers to better understand the development of graphite/Si anodes.

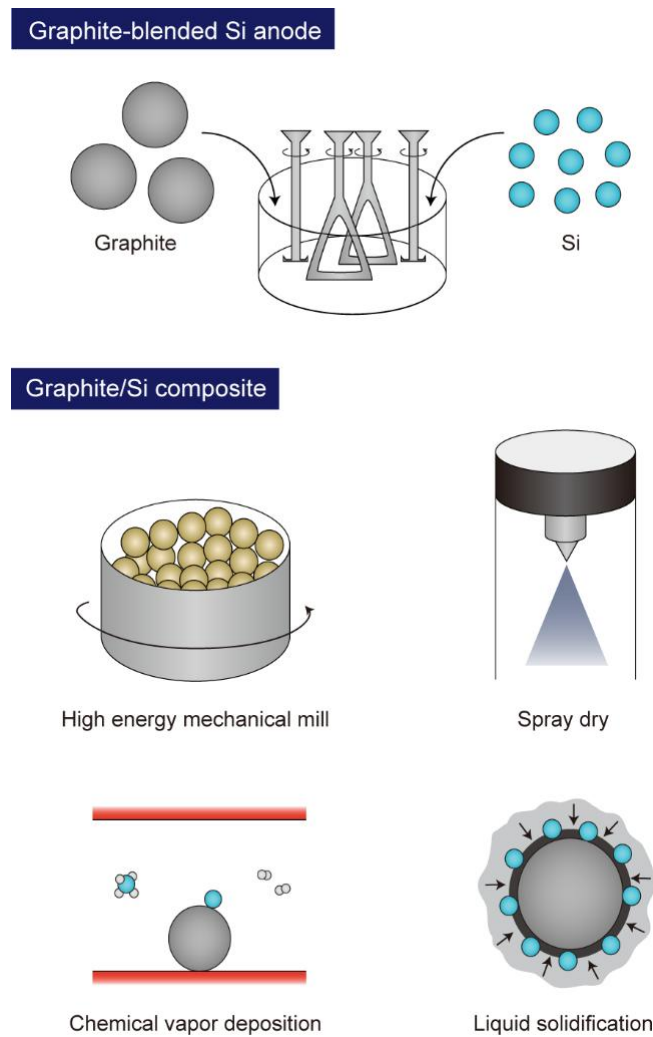


Figure 1. 5. Schematic illustration of various synthetic methods for graphite-blended Si anode and graphite/Si composite

1. 3.1 Graphite-blended Si anodes

Considering practical application, various kinds of high-capacity Si materials have been investigated with fabricating the graphite-blended electrode. Here, we introduce several representative studies for graphite-blended Si anode including a combination between active Si and the inactive matrix such as silicon monoxide (SiO_x)⁸³⁻⁸⁴, Si-metal alloys,⁸⁵⁻⁸⁸ and porous Si.^{52, 89} The studies have aimed at alleviating volume changes with following common strategies: 1) introduction of mechanical buffer matrix and 2) formation of void spaces for accommodating Si expansion. It is noted that the huge difference in volume change of active materials would result in electrical contact loss of graphite, leading to additional deterioration. Hence, the alleviation of volume expansion allows not only to secure cycling stability of high-capacity Si anodes, but also to improve the compatibility with the graphite.

It has been widely known that SiO_x and Si-metal alloys exhibit high specific capacity of 1300-1500 and 800-1300 mAh g^{-1} , respectively.⁸³⁻⁸⁸ They effectively alleviate the volume change by surrounding nano-Si with mechanical buffer matrix (amorphous SiO_2 or metal silicides) on (de)lithiation. For SiO_x , amorphous SiO_2 generates undesirable irreversible byproducts including Li_2O ⁹⁰ and Li_4SiO_4 ,⁹¹⁻⁹² so optimization of the oxygen contents in SiO_x has been a major issue to determine its cycling behavior. For example, with granulated SiO_x particle (**Fig. 1. 6a**), S.-S. Suh et al. reported that the optimal amount of oxygen in SiO_x is 1.06.⁹³ Under high areal capacity (~ 3 mAh cm^{-2}) and the high ratio of active materials (90 wt%), blending 3 wt% of $\text{SiO}_{1.06}$ with graphite demonstrated the initial specific capacity of 397 mAh g^{-1} with capacity retention of 76% after 200 cycles in full-cell configuration (**Fig. 1. 6b**).

Similar with amorphous SiO_2 in SiO_x , Si-metal alloys employ inactive silicide as a buffer matrix by the homogeneous formation of alloy phase in their structure, where the silicides contain both high mechanical stability and electrical conductivity.⁹⁴⁻⁹⁵ It is noticeable that the phase transition and crystallite size of silicide are strongly dependent on the annealing condition, which affects the electrochemical performance. S.-M. Lee and co-workers reported Ti-Si binary alloy@porous Si core-shell structure (C/S) composites.⁷⁸ C/S composites were prepared by annealing Ti-Si alloys and following reaction with hydrofluoric acid to form porous Si at the interfacial region. As a result, C/S composites consist of a core which active Si and inactive binary silicide (TiSi_2), and porous Si shell. The formation of TiSi_2 and the crystallite size of Si were tuned by annealing C/S composites at 600, 700 and 800 °C, which affected the pore sizes on the shell (**Fig. 1. 6c-e**) as well. The C/S composite annealed at 600 °C (denoted as MAE600) demonstrated the superior performance as shown in Figure 6f. To investigate the effect of the size of the graphite in the graphite-blended system, MAE600 was blended with spherical natural graphite SG1 ($D_{50} = 7$ μm) and SG2 ($D_{50} = 12$ μm). MAE600 exhibited the initial specific capacity of 1006.2 mAh g^{-1} with the initial efficiency of 83.4%. The graphite-blended MAE600 electrodes with SG1 and SG2 demonstrated the enhanced cycling stabilities by virtue of

graphite. Interestingly, the electrode with SG1 showed superior capacity retention than that of the electrode with SG2 during 50 cycles (Fig. 1. 6g). It was attributed to the similar particle size between MAE600 ($D_{50} = 8 \mu\text{m}$) with graphite, thereby leading to the uniform distribution of MAE600 and graphite in the electrode. This result implies that the compatibility of graphite and high-capacity Si anodes would have a considerable influence on the battery performances. Furthermore, it was obviously demonstrated that the cycle life was gradually improved as the content of graphite in the electrode increased (Fig. 1. 6h).

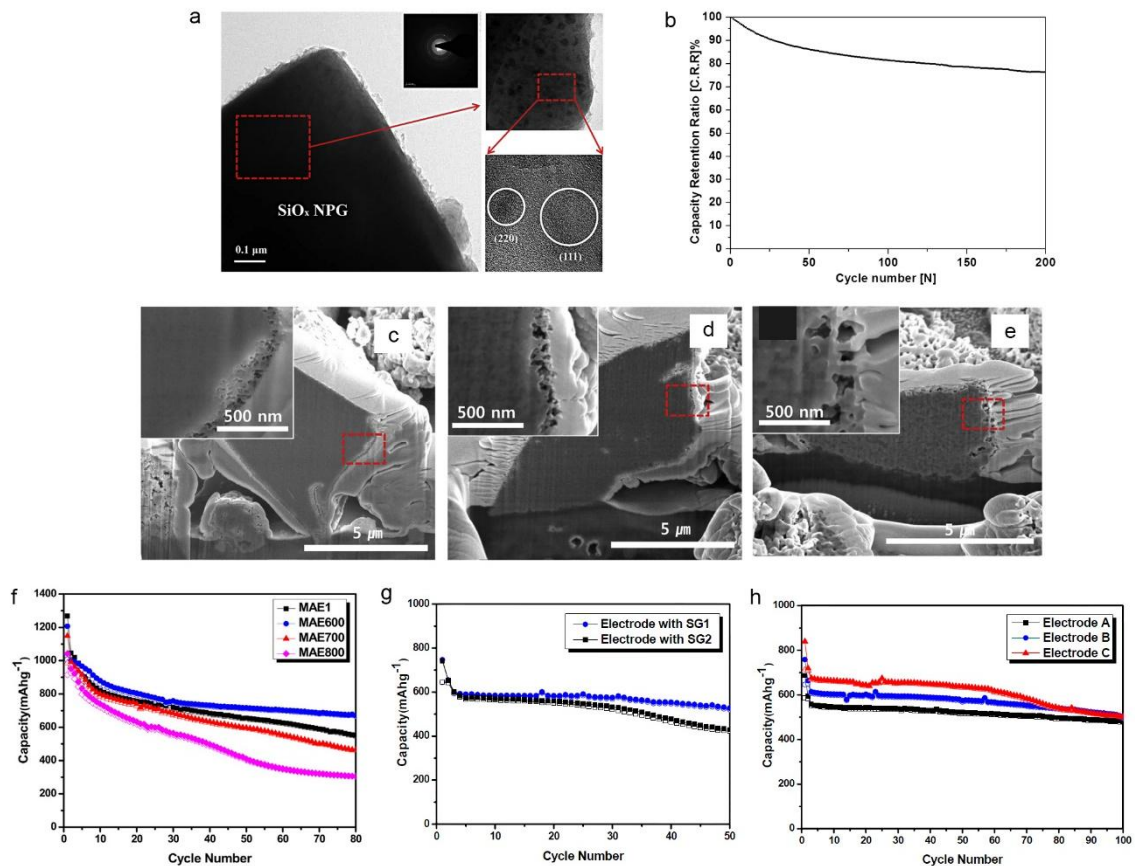


Figure 1. 6. SiO_x and Si-metal alloys for graphite-blended Si anode. a) TEM images and selective area electron diffraction patterns (SAED) of granulated SiO_x particle. b) Discharge capacities of graphite-blended SiO_x in full-cell for 200 cycles. Copyright: Elsevier, 2014. c-e) Cross-sectional SEM images of Ti-Si binary alloy@porous Si core-shell (C/S) composites annealed at (c) 600 °C, (d) 700 °C, and (e) 800 °C, respectively. Inset gives the magnified images. f) Discharge capacities versus cycle numbers showing effects of annealing temperature. g) Discharge capacities of blended electrodes including MAE600 and graphite (SG1 and SG2). h) Discharge capacities of blended electrodes including MAE600 and SG1 with various ratio (A: 35/65, B: 45/55, and C: 55/45). Copyright: Elsevier, 2015.

Besides, M. N. Obrovac and co-workers attempted to investigate the role of graphite in the graphite-blended Si anode where the commercial Si-based alloy, 3M alloy (L-20772 V6, denoted as V6), was utilized.⁹ Despite high cycle efficiency and stable microstructure of V6,⁵⁰ calendaring causes to the particle fracture (**Fig. 1. 7a, b**) and poor capacity retention as in **Figure 1. 7c**. Instead, in the graphite-blended electrode, the additional graphite (MAG-E and SFG6L) could buffer against calendaring, thereby preventing particle fracture, mitigating volume expansion and enhancing cycling performance (**Fig. 1. 7d, e**). Therefore, even under high loading (4.5 mg cm^{-2}) and mass ratio of active material ($> 88 \text{ wt}\%$), the graphite-blended electrodes achieved improved electrochemical properties and volumetric energy density, compared to the graphite-free V6 electrode (**Fig. 1. 7f**). Additionally, the smaller-sized SFG6L graphite, with average particle size of $3 \mu\text{m}$, also improves the cycling performance, which is attributed to the homogeneous distribution and better interconnectivity among particles during calendaring (**Fig 1. 7g**). As a result, V6/graphite electrode attained the estimated full-cell stack energy density approximately 15% higher than $\text{LiCoO}_2/\text{graphite}$ cell, confirming the possibility of commercial utilization (**Fig 1. 7h**). This work concretely shows the advantage of the co-utilization of graphite and Si for the practical implementation of Si anode with improved cycle life and volumetric energy density.

Porous Si has been also recognized as an attractive strategy in terms of accommodating volume expansion.⁹⁶⁻⁹⁷ As an investigation of the practical application, X. Li et al. fabricated the graphite-blended anode with their developed porous Si/C composite (**Fig. 1. 8a**).⁵² They attempted to design the electrode which can satisfy below strict requirements: 1) higher specific capacity than graphite (372 mAh g^{-1}); 2) high capacity retention ($> 80\%$ over ~ 500 cycles); 3) limited electrode swelling as low as graphite ($\sim 10\%$); 4) practical loading level ($\sim 3 \text{ mAh cm}^{-2}$). The electrode, where the blending ratio of porous Si/C to graphite was 1:2, exhibited a specific capacity of $\sim 650 \text{ mAh g}^{-1}$ with a high areal capacity (3 mAh cm^{-2}) and low coulombic efficiency of $\sim 63\%$ (**Fig. 1. 8b**). Although there was a rapid capacity drop during early cycles, after then, it demonstrated excellent capacity retention of 90% over 200 cycles as shown in **Figure 1. 8c**. Interestingly, they inspected the effect of calendaring on the porous Si/C composite. After the calendaring process, the porous Si/C composite retained their own morphology (**Fig. 1. 8d, e**). However, in the calendared electrode, the polarization was increased by the reduced accessibility of the electrolyte, where only $85\text{-}90\%$ of specific capacity was exhibited. Finally, with the graphite-blended electrode, the commercial feasibility of porous Si/C composite in the graphite-blended electrode was successfully demonstrated with outstanding cycle life ($> 84\%$ for 300 cycles) in the full-cell (**Fig. 1. 8f**), where the prelithiation was carried out for compensating the initial capacity loss.

Recently, our group reported Fe-Cu-Si composites (FeCuSi) which were fabricated by spray drying and subsequent heat treatment (**Fig. 1. 9a**).⁴⁸ With the particle size ($D_{50} = 6.5 \mu\text{m}$, **Fig. 1. 9b**) compatible to graphite, FeCuSi have spherical secondary particles where Si nanoparticles ($< 150 \text{ nm}$) are

surrounded by metal silicides (FeSi_2 and $\text{Cu}_{3.17}\text{Si}$) and void spaces (**Fig. 1. 9c, d**). Metal silicides act as glue binding Si nanoparticles to reinforce the secondary structure and reduce the volume change of each material by diluting the active phase. In addition, the high porosity in the secondary structure accommodates the volume expansion upon lithiation.^{35, 42} FeCuSi exhibited the initial specific capacity of 1287 mAh g^{-1} with the high initial Coulombic efficiency of 91%. To investigate its commercial feasibility, the graphite-blended electrode was adopted to perform rational comparison with other benchmarking samples (SiO and FeSi_2) under industrial standards such as high areal capacity (3.44 mAh cm^{-2}), high electrode density (1.6 g cc^{-1}), and large amounts of active materials (total 96 wt%). By adjusting the blending ratio, the specific capacities of the three samples were fixed with 420 mAh g^{-1} for a fair comparison, as shown in **Figure 1. 9e**. Among three graphite-blended electrodes, FeCuSi showed the highest discharge capacities and Coulombic efficiencies during long-term cycling in both half- and full-cell configurations (**Fig. 1. 9f, g**). Therefore, this work implies that the fabrication of graphite-blended electrode allows the rational comparison of high-capacity Si anodes for commercial feasibility.

In summary, industrially-developed Si materials, such as SiO_x ,^{49, 93} Si-metal alloys,^{9, 48, 50, 78} and porous Si^{52, 89} have mostly demonstrated their commercial viability in the graphite-blended anode. Graphite plays a role in not only improving the electrochemical stability but also making various Si anodes applicable to conventional battery manufacturing process. We consider the evaluation method with graphite-blended Si anode, where the parameters for volumetric energy density are surely taken into account, will play important roles in the rational performance comparison and the feasibility study of emerging Si anode for high-energy LIBs.

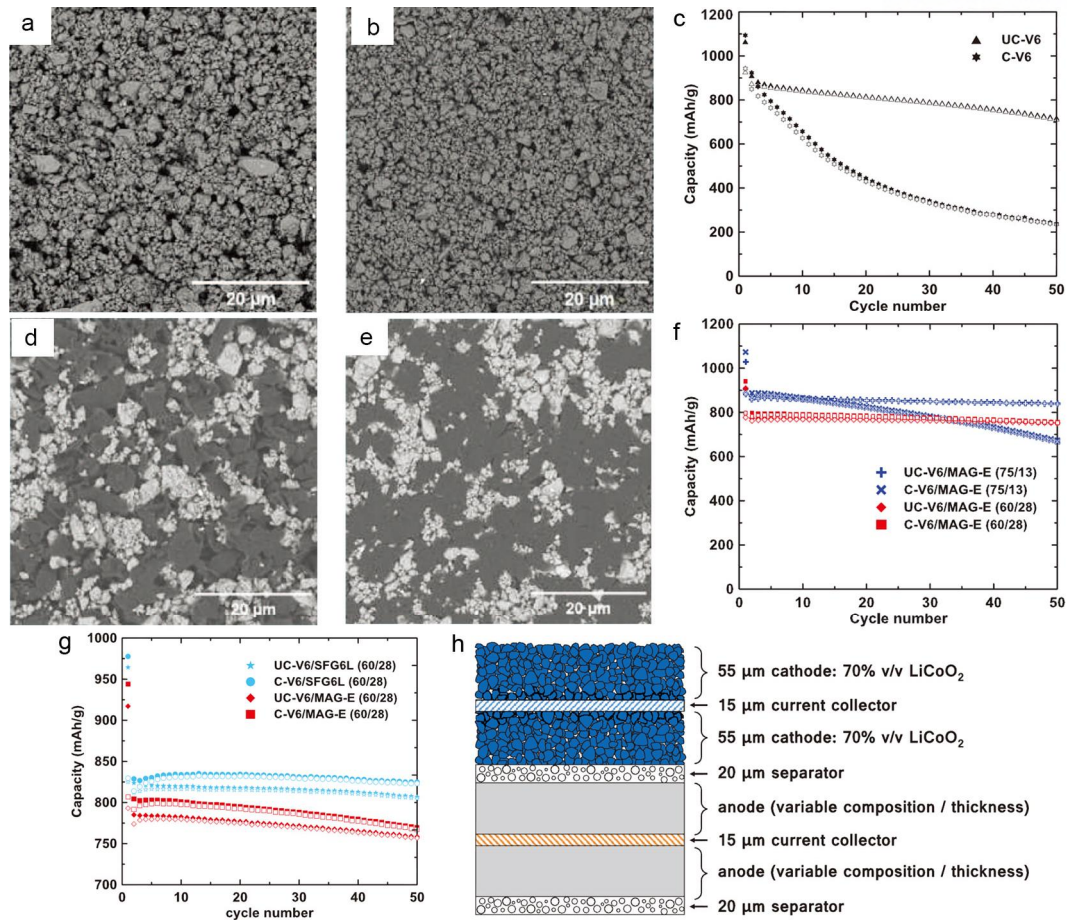


Figure 1.7. 3M Si alloy (V6) for graphite-blended Si anode. a), b) SEM images of (a) uncalendered and (b) calendered V6 electrodes, respectively. c) Discharge capacities of uncalendered and calendered V6 electrodes. d), e) SEM images of (d) uncalendered and (e) calendered V6/SFG6L electrode, respectively. f) Discharge capacities of uncalendered and calendered V6/MAG-E electrode with different amounts of MAG-E. g) Discharge capacities of uncalendered and calendered V6/MAG-E and V6/SFG6L electrodes. h) Schematic design of cell stack model. Copyright: the Electrochemical Society, 2014.

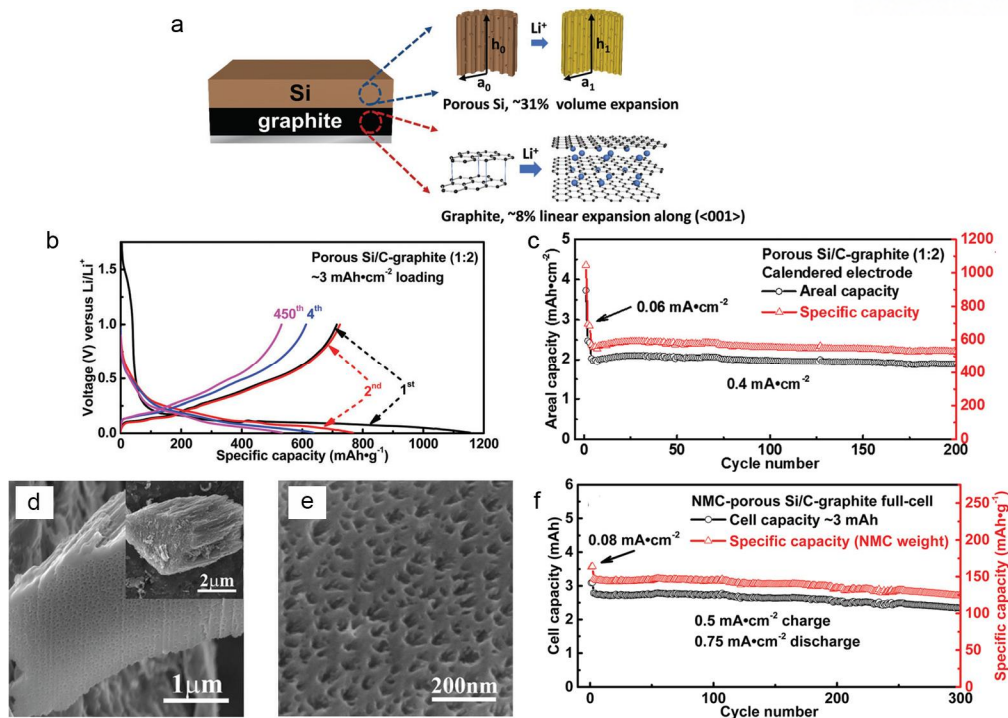


Figure 1. 8. Porous Si for graphite-blended Si anode. a) Schematic design of porous Si/C-graphite electrode. b) Voltage profiles of porous Si/C-graphite electrode (1:2) at the first cycle. c) Discharge capacities of the calendared porous Si/C-graphite electrode (1:2) in the half-cell. d) Cross-sectional SEM image of porous Si/C particle in calendared electrode. Inset indicates corresponding low magnification SEM image. e) High magnification SEM image of (d). f) Discharge capacities of full-cell building with $\text{Li}(\text{Ni}_{1/3}\text{Mn}_{1/3}\text{Co}_{1/3})\text{O}_2$ cathode and pre-lithiated anode over 300 cycles. Copyright: Royal Society of Chemistry, 2017.

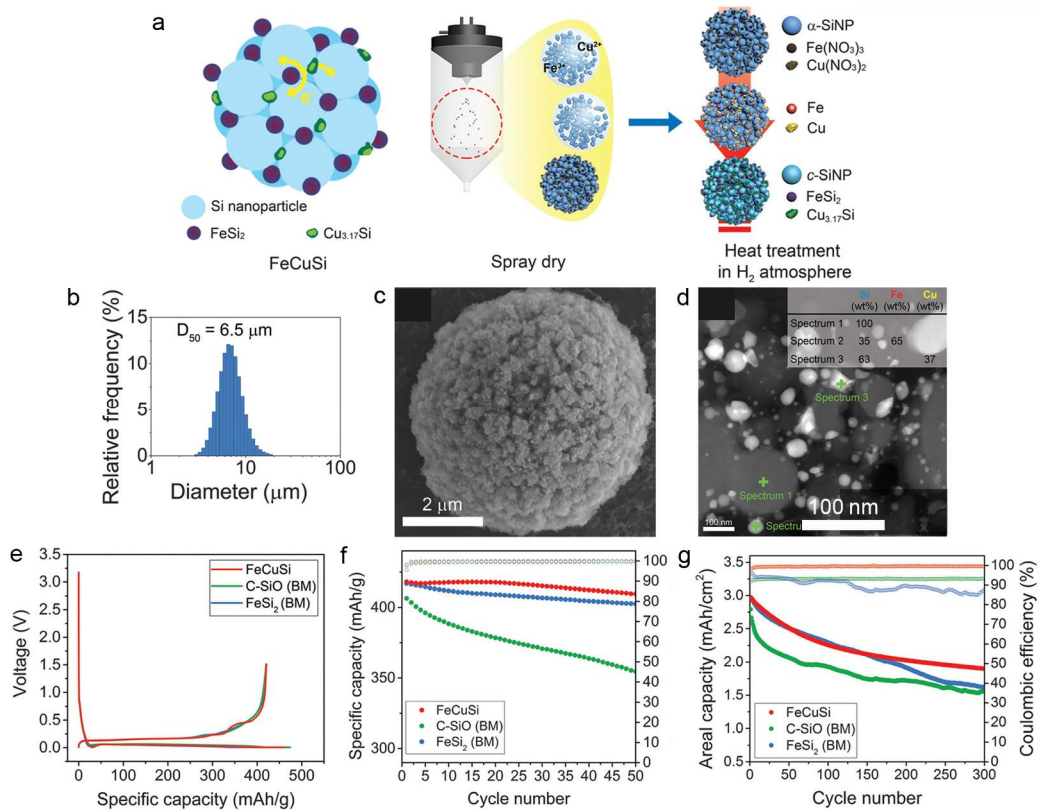


Figure 1. 9. Fe-Cu-Si ternary composites (FeCuSi). a) Schematic illustration of the structure of FeCuSi and its synthetic process. b) Particle size distribution of FeCuSi. c) SEM image of FeCuSi. d) Magnified cross-sectional HAADF-STEM image of FeCuSi and elemental analysis at Si and metal silicides phase in FeCuSi particle. e) Voltage profiles of graphite-blended FeCuSi and other benchmarking samples (C-SiO_x, and FeSi₂) at the first cycle. f) Discharge capacities and cycling CEs of the graphite-blended anodes for 50 cycles in half-cell configuration. g) Discharge capacities and cycling CEs of the graphite-blended anodes with LiCoO₂ cathode for 300 cycles. Copyright: Royal Society of Chemistry, 2016.

1.3.2. Various synthetic methods for the graphite/Si composite

Since the first graphite/Si composite by Wang et al. in 1998,⁹⁸ various strategies were suggested to fabricate the graphite/Si composite to address issues coming from the massive volume changes of Si anodes during cycling. In this section, we categorized various graphite/Si composites according to synthetic methods, including ball-milling, spray drying, chemical vapor deposition (CVD), and liquid solidification. From the viewpoint of commercial feasibility, various representative graphite/Si composites synthesized by such methods were reviewed in terms of productivity, morphological features, electrochemical performances and current limitation.

1.3.2.1 High energy mechanical milling

The high energy mechanical milling including ball-milling has been used to pulverize bulk materials into fine particles through the collisions with high energy rotating balls.⁹⁹ Additionally, these collisions could lead to the formation of the secondary particle *via* repeated flattening, fracturing, and rewelding of the particles.^{94, 100-102} Such a method is highly attractive because of its simplicity, cost-effectiveness, and facile procedure compared to synthetic chemical routes, and it also has a potential of scale up to mass production.^{46, 103-107} However, excessive milling with high-energy could destroy the crystallinity of graphite and additional surface area, leading to unfavorable side reaction.

In 1998, C. S. Wang et al. firstly reported the graphite/Si composite synthesized by the ball-milling method for 150 h under Ar atmosphere.⁹⁸ The authors demonstrated a composite with well-distributed Si nanoparticles on graphite, which could utilize both the high gravimetric capacity of Si and excellent electrochemical stability of graphite as shown in **Figure 1. 10a**. From the microstructure observation, the ball-milled graphite has wrinkled layers with irregular thickness and a distribution of interlayer spacing (**Fig. 1. 10b**). It was expected that the unorganized carbon and microcavities could be formed along the edge of structural units. The ball-milled graphite in the composite piles up as distorted columns, and it encapsulates the Si as a form of amorphous layer (**Fig. 1. 10c, d**).

With various input ratios between graphite and Si, kinds of $C_{1-x}Si_x$ ($x = 0, 0.1, 0.2, \text{ and } 0.25$) demonstrated reversible specific capacities from 437 mAh g^{-1} (pulverized graphite) to 1039 mAh g^{-1} ($C_{0.8}Si_{0.2}$). In particular, $C_{0.8}Si_{0.2}$ demonstrated good capacity retention after 20 cycles than that of the unmilled graphite/Si mixture (**Fig. 1. 10e**).

In comparison with electrochemical performances of unmilled graphite/Si mixture, those of ball-milled graphite/Si composites could be improved on account of nano-sized Si mitigating a lithiation-induced strain and graphite providing an electrical network to Si as a conductive matrix. However, electrochemical instability, which originated in degradation of Si and insufficient adhesion between Si and graphite, still has hindered their practical application resulting from Si delamination and collapse of electrical networks during long-term cycles.^{101, 108}

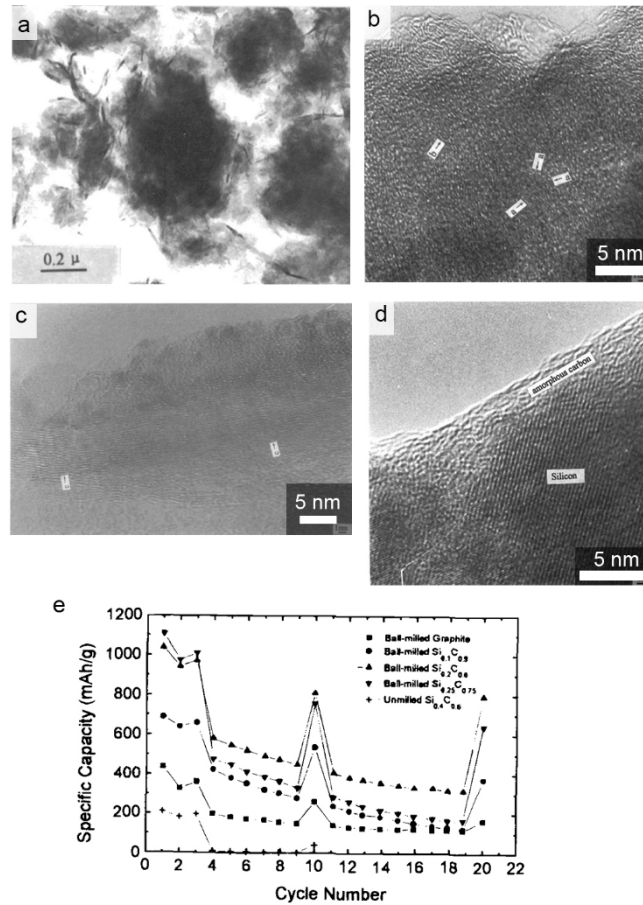


Figure 1. 10. Graphite/Si composite fabricated by ball-milling. a) SEM image of the graphite/Si composites ($C_{0.8}Si_{0.2}$). b) HR-TEM image of the ball-milled graphite for 150 h. c) HR-TEM image of the ball-milled $C_{1-x}Si_x$ composite. d) HR-TEM image at the surface region of ball-milled $C_{1-x}Si_x$ composites. e) Discharge capacities of ball-milled $C_{1-x}Si_x$ ($x=0, 0.1, 0.2, \text{ and } 0.25$) and unmilled $C_{0.6}Si_{0.4}$. Copyright: the Electrochemical Society, 1998.

To address the demolition issue of graphite in the high energy mechanical milling process, Y.S. Yoon et al. utilized spherical natural graphite, Si nanoparticles and pitch carbon as a glue layer with mild rotation speed and time (60 rpm and 2h).¹⁰⁹ As shown in **Figure 1. 11a, b**, Si nanoparticles were uniformly attached on the graphite surface. However, secondary Si particles which were agglomerated during ball-milling were observed in some regions at the surface of graphite. The pitch-derived carbon bonds the Si nanoparticles with the graphite strongly (**Fig. 1. 11c**).

The relatively low milling time, the addition of Si nanoparticles, and pitch carbon successfully kept graphite intact. It was proved by X-ray diffraction pattern (XRD) (**Fig. 1. 11d**), where the interlayer distance (d_{002}) of the graphite was determined to be 3.37 Å which is close to the ideal crystalline graphite (3.36 Å). Furthermore, the intercalation and de-intercalation of lithium with graphite were detected in the differential voltage curve (dQ/dV vs. V), which corresponds to the small and broad peak at ~0.13 V during the 1st discharge and the three peaks at ~0.11 V, ~0.15 V and ~0.23 V during charging (**Fig. 1. 11e**). Accordingly, the preservation of the original form of graphite let the graphite/Si composite have a high reversible capacity of 655 mAh g⁻¹ with initial Coulombic efficiency (CE) of 86% with avoiding the additional side reaction. The composite also achieved outstanding capacity retention of 71.4% over 300 cycles in 100 mAh grade full-cell configuration with LiCoO₂ cathode (**Fig. 1. 11f**).

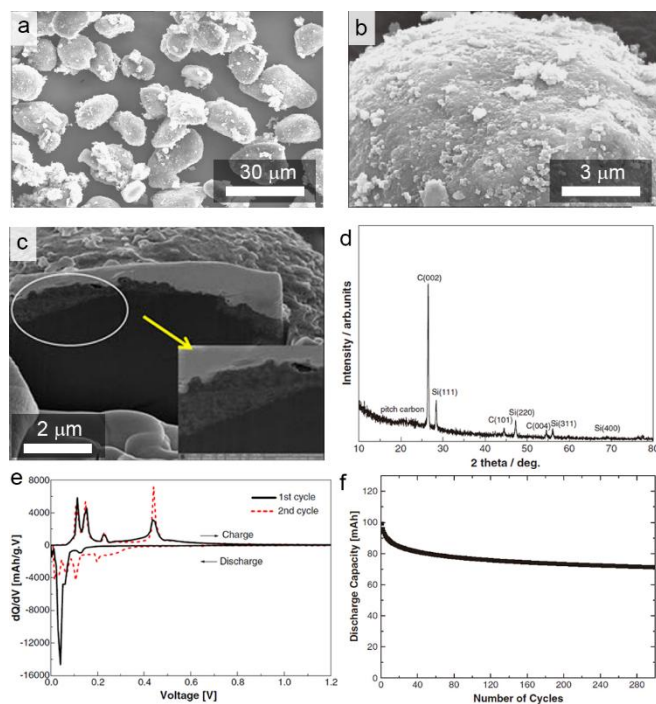


Figure 1. 11. Natural graphite/Si/pitch composite by ball-milling. a), b) SEM images of Si-coated natural graphite composites. c) Cross-sectional view of Si-coated natural graphite composites, where the homogeneous and smooth coating layer of Si was formed on the graphite. d) XRD pattern of the natural graphite/Si/pitch composite. e) dQ/dV plots for the 1st and 2nd cycles. f) Discharge capacities in the prototype full-cell system for 300 cycles. Copyright: Elsevier, 2011.

Recently, various Si/inactive matrix anodes, such as SiO_x,¹⁰³ Si-Fe,¹¹⁰ Si-Ni,¹⁰⁷ and Si-P,¹⁰⁴ were utilized to build a composite with graphite by the high energy mechanical milling method (**Fig. 1. 12**). They used the graphite as an outer shell for imparting the high electrical conductivity and shielding the Si anodes from additional side reactions. Owing to the synergistic effect of the inactive matrix and the graphite in the composite, the composites exhibited stable cycling behavior with high specific capacity. However, the severe demolition of graphite including pulverization and crystal transformation is remaining issue, causing inevitable side reactions between the graphite and electrolyte. It would be required to carry out the high energy mechanical milling delicately for minimizing the additional side reaction.

In terms of industrial approach, ball-milling method is one of the most advantageous techniques to synthesize graphite/Si composite owing to its simple cost-effective process and feasibility of mass production for commercialization.^{46, 103-107} Besides, ball-milling can be strong method in the point that it the introduction of, improves not only adhesion strength between graphite and Si but also electrical conductivity with the formation of the continuous electrical network.¹¹¹⁻¹¹⁹ Furthermore, implantation of the inactive matrix into Si suppresses a severe side reaction with electrolyte, as well as the strain induced by the volume change of Si.^{46, 102-104, 107, 110, 120-121} However, in spite of these noticeable merits, several challenges of ball-milling technique still have remained as a practical limitation for commercial application, such as structurally damaged graphite or an immoderately increased surface area, which brings about an excessive irreversible capacity and lowering initial CE.

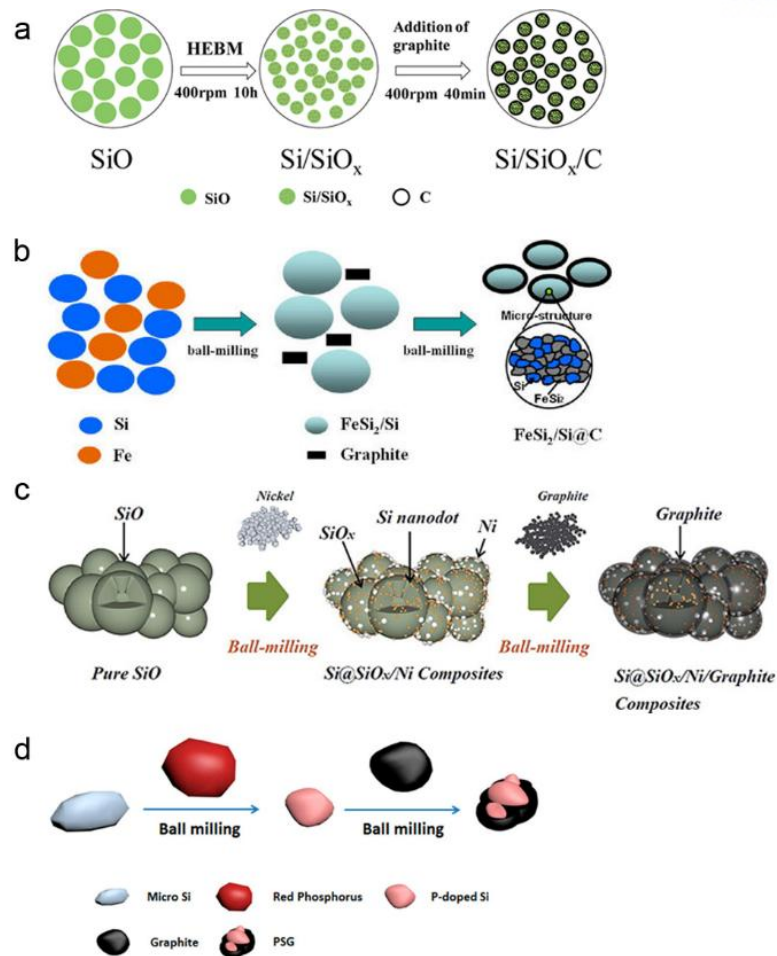


Figure 1. 12. Si/inactive matrix/graphite composites by ball-milling. a) Schematic illustration of fabrication process of Si/SiO_x/C composite. Copyright: Royal Society of Chemistry, 2017. b) Schematic illustration of fabrication process of FeSi₂/Si@C composite. Copyright: American Chemical Society, 2012. c) Schematic illustration of the fabrication process for SiO_x/Ni/graphite composites. Copyright: Wiley-VCH, 2015. d) Schematic illustration of the synthetic process for nanostructured P-doped Si/graphite composite. Copyright: American Chemical Society, 2017.

1.3.2.2 Spray drying

Spray drying is a method of manufacturing a dry powder from a liquid solution by rapidly drying with a heated gas.¹²² The input solution is sprayed through a spray nozzle into a heated vapor stream and evaporated, and then dried powder is formed from the droplets. According to the diameter of the nozzle, the solution is dispersed into a variously controlled drop size spray, and it allows for uniform size distribution of dried particle.¹²³ The spray drying process rapidly produces a dried product from a liquid solution in a single step, and it could be also carried out continuously, which is advantageous for facile synthesis and mass production.¹²⁴⁻¹²⁷

In LIB application, numerous researches have been reported that the electrochemical performance of the graphite/Si composites could be improved by applying characteristic carbonaceous materials *via* the spray drying technique.¹²⁸⁻¹³¹ Lei Gan et al. reported a spherical graphite/Si/graphene (graphite/Si@reGO) composites through a spray drying.¹³² To prepare a homogeneous solution, Si nanoparticles and flake graphite were dispersed in as-prepared graphene oxide (GO) suspension with the ultra-sonication for 2 h. The weight ratio of graphite, nano-Si, and GO was controlled as 9:1:1.4. After that, the homogeneous solution was spray dried at inlet and outlet temperatures of 150 and 100 °C, respectively. Then, calcination of the dried precursor (graphite/Si@GO) was carried out at 600 °C for 2 h under Ar atmosphere in order to obtain a final product denoted as spherical graphite/Si@reGO by thermal reduction of GO into reGO. As shown in **Figure 1. 13a**, the surface of graphite/Si@reGO composite was mainly composed of flake graphite sheets, and nano-Si was uniformly distributed into the inner structure of the composite, which of the whole structure is encapsulated by reGO (**Fig. 1. 13b**). Flake graphites in the composite could act as a buffer matrix for lithiation-induced volume expansion of Si, and reGO coated on the whole structure provides a long-range electrical network and good structural integrity with strong adhesion between Si and graphite. Thus, the graphite/Si@reGO showed the initial reversible capacity of 575.1 mAh g⁻¹ with better cycle stability (73.1% after 50 cycles) compared with mechanical blended graphite/Si composite.

Min Li and coworkers suggested a core-shell structure of graphite/Si-porous carbon (denoted as core-shell porous Si/C) composite by spray drying with various carbonaceous additives including PVP, pitch, and citric acid.¹³³ The mass ratio of graphite to Si to carbonaceous additives in the raw materials was designed as 72:10:18, and the homogeneous suspension including the raw materials was spray dried at 120 and 80 °C of inlet and outlet temperature, respectively. The primary precursor was further spray-dried with a pitch-based carbon solution. Then, the obtained powder was calcinated at 900 °C for 3 h to fabricate the core-shell porous Si/C composite. According to SEM images in **Figure 1. 13c, d**, the composite built up with a dense graphite core and a porous amorphous carbon shell with a thickness of 1–3 μm. Moreover, Si nanoparticles were embedded into the porous carbon shell which not only

accommodates the volume change during (de)lithiation process of Si but also impregnates liquid electrolyte into the graphite core ensuring a high electric active surface area for the graphite. As a result, Si/C composites exhibited good cycle retention of 81.8% over 100 cycles despite its relatively high initial capacity of 723.8 mAh g⁻¹ (**Fig. 1. 13e**).

Dopamine is a kind of nitrogen doped organic material which can provide a superior electrical conductivity after carbonization.¹³⁴ In addition, it is easily transformed into polydopamine (PDA) by oxidative polymerization, which tends to be strongly adsorbed on the surface of various substances.¹³⁵⁻¹³⁶ These interesting properties of PDA were studied as an additive for graphite/Si composite by Rong Zhou and coworkers.¹³⁷⁻¹³⁸ The authors employed PDA as carbon coating source on the as-prepared spray-dried Si/graphite (Si/G) composite, resulting in the fabrication of Si/graphite/PDA-C (Si/G/PDA-C) composite after carbonization process. As presented in the SEM and EDS mapping images in **Figure 1. 13f, g**, the Si/G/PDA-C composite was comprised of homogeneously distributed Si nanoparticles on the surface of graphite, and the nano-Si and graphite were well connected each other by the uniform coating layer of PDA-C. Additionally, such coating layer could prevent the composite from direct exposure to the liquid electrolyte, as well as function as a buffer matrix for severe volume expansion of Si. Furthermore, owing to the N-doping chemistry of PDA-C showing a high electrical conductivity, the Si/G/PDA-C composite achieved an enhanced cycling behavior and rate capability in electrochemical evaluation as shown in **Figure 1. 13h**. Surprisingly, Si/G/PDA-C electrode remained structural integrity of the particles without any cracks even after 100 cycles while severe cracks occurred in case of Si/G electrode, which can cause the loss of electrical contact among particles.

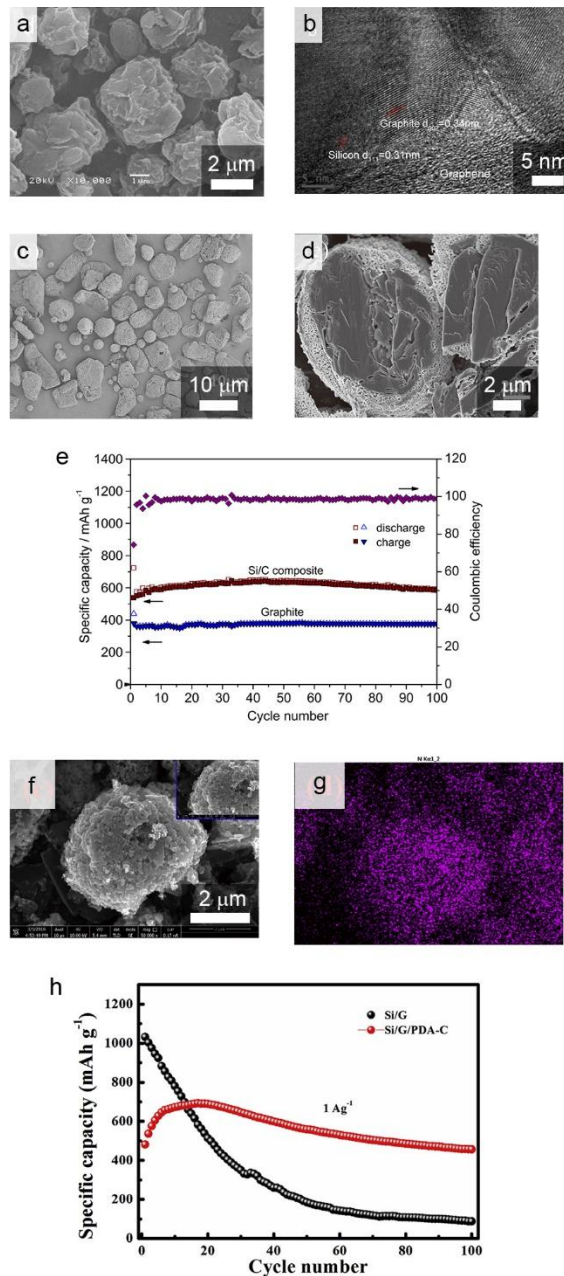


Figure 1. 13. Graphite/Si composites fabricated by spray drying. a), b) SEM and TEM image of graphite/Si@reGO composite. Copyright: Elsevier, 2013. c) SEM image of Si/C composites. d) Magnified cross-sectional image of Si/C composites. e) Discharge capacities and cycling CEs of Si/C composites, demonstrating its comparability with that of graphite. Copyright: Elsevier, 2014. f) SEM image of Si/G/PDA-C composites. g) EDS mapping image of N for Si/G/PDA-C composites depicting the presence of the polydopamine on the surface. h) Discharge capacities of Si/G and Si/G/PDA-C composites. Copyright: Elsevier, 2016.

Recently, Yu-Guo Guo et al. proposed a watermelon-inspired Si/C microsphere *via* spray drying method with flake graphite and carbon coated nano-Si (C-coated nano-Si).⁶⁷ The watermelon-inspired Si/C microsphere is formed as a secondary structure consisted of the C coated nano-Si well dispersed in the ball-milled flake graphite. Such a novel Si/C design as described in **Figure 1. 14a, b** exhibits the following advantages. Firstly, the graphite framework acts as an electrical network and suppresses the aggregation of nano-Si. Secondly, carbon coating on nano-Si mitigates the volume change of Si during repeated (de)alloying process and improves the ionic/electric conductivity between graphite and Si. Thirdly, numerous internal pores of the composite produced from the spray drying provides additional space for the accommodation of the volume change. Finally, relatively high tap density (0.88 g cm^{-3}) of the Si/C composite is advantageous to prepare densely packed anodes for practical application. As a result, the Si/C microspheres presented an excellent initial CE of 89.2% with the reversible capacity of 620 mAh g^{-1} and achieved outstanding capacity retention (75.2%) over 500 cycles under the high areal capacity of 2.54 mAh cm^{-2} (**Fig. 1. 14c, d**).

In summary, spray drying has been utilized for fabricating graphite/Si composites with the combination of graphite, Si nanoparticles, and carbonaceous additives. Their assembly exhibits several advantages. Internal pores forming in spray drying effectively relieve the volume change of Si.^{131, 133, 139-141} Furthermore, The large particle size distribution and spherical shape of high tap density increase the packing density, which is favorable to high volumetric energy density.^{67, 128} Also, the facile, continuous and scalable synthesis gives the practical application of Si anodes.¹²⁴⁻¹²⁷ Such advantages will be used practically by battery researchers for fabricating next-generation graphite/Si composites.

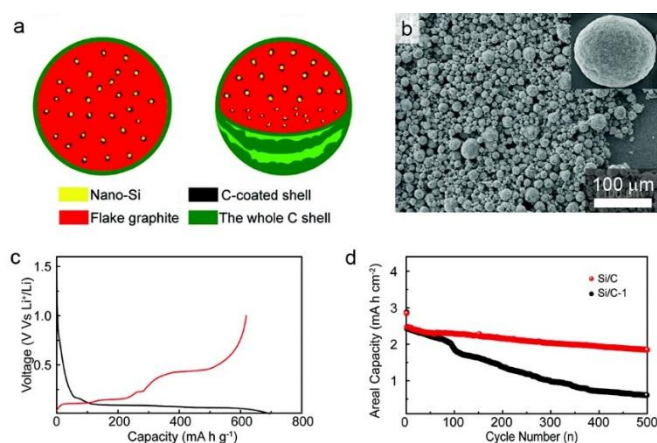


Figure 1. 14. Si/C microspheres fabricated by spray drying with Si nanoparticles and ball-milled flake graphite. a) Schematic illustration of the overall structure of watermelon-inspired Si/C microspheres. b) SEM image of hierarchical buffer structured Si/C microspheres. The inset gives the magnified SEM image of the single microparticle. c) Voltage profiles of Si/C microspheres at the first cycle. d) Areal capacities of Si/C microspheres for 500 cycles. Copyright: Wiley-VCH, 2017.

1.3.2.3 CVD

CVD is a chemical method used to produce high purity solid materials by decomposition of volatile precursors.¹⁴² In a typical CVD process, the substrate is exposed to gaseous precursors which can be decomposed by applying energy such as heat or plasma to produce a thin film type of deposit. The CVD method is favorable to the synthesis of high-quality deposition, controllability of nano-scale deposition thickness, and its relative simplicity of the process. On the basis of these merits, many researchers have attempted to fabricate graphite/Si composite *via* CVD method using silane (SiH_4) gas as Si precursor.

In 2004, J. Xie, et al. primarily synthesized Si-coated mesocarbon microbeads (MCMB) through thermal CVD of SiH_4 gas.¹⁴³ The authors placed MCMB powder in the middle of the reactor, and the CVD process was conducted with the flow of gaseous precursor at 450 and 500 °C, respectively. According to the SEM image in **Figure 1. 15a, b**, the smooth surface of pristine MCMB became coarse after Si deposition on the outermost surface. From the Raman spectroscopy in Figure 15c, it was confirmed that the small amount of Si was coated on the surface of MCMB, where the crystalline Si peak at 520 cm^{-1} was observed with the graphitic D- and G- peaks (1360 and 1590 cm^{-1}). In the Si-coated MCMB, the graphite core can effectively relieve the stress which arises from the volume variation of Si layer upon cycling. Thereby, the composite accomplished competitive cycling stability with a higher reversible capacity compared with that of pristine MCMB (**Fig. 1. 15d**).

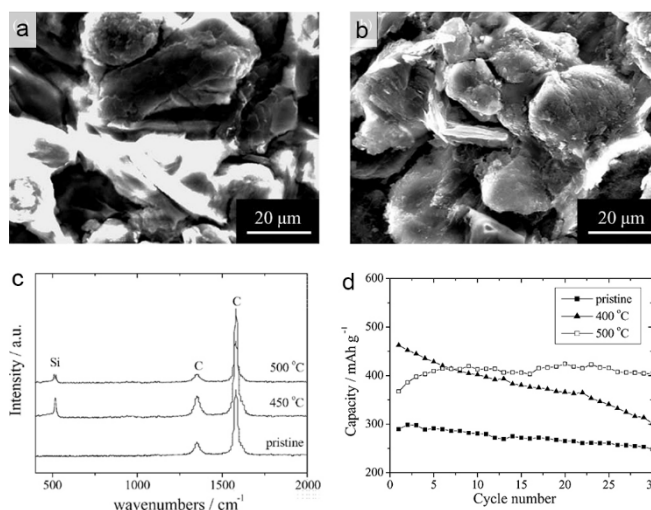


Figure 1. 15. Graphite/Si composites fabricated by CVD. a), b) SEM images of (a) pristine MCMB and (b) Si-coated MCMB. c) Raman spectra of pristine and Si-coated MCMB. d) Discharge capacities with different treating temperature of Si coating on MCMB. Copyright: Elsevier, 2004.

In-Chul Kim et al. reported the copper silicide-coated graphite composite through plasma enhanced chemical vapor deposition (PECVD) and radio-frequency (RF) magnetron sputtering.¹⁴⁴⁻¹⁴⁵ The PECVD was performed to deposit the Si on the graphite, and then copper film was subsequently coated on the surface of Si-coated graphite by RF magnetron sputtering. According to the SEM images in **Figure 1. 16a-c**, the graphite was well covered by Si and copper silicide, which is too similar to be distinguishable. The author acknowledged that their particle mixing system was not effective for producing uniform coating on the graphite surface, but the contents of Si and copper silicide in the bulk scale was regarded as uniform. Instead, the Cu 2p and four types of Siⁿ⁺ spectra observed by XPS measurement imply the presence of copper silicide layer on the surface of graphite (**Fig. 1. 16e, f**). As can be seen in **Figure 1. 16d**, the copper silicide-coated graphite demonstrated the lower resistivity than that of Si-coated. Besides, the copper silicide acts as a buffer layer for the repeated volume change of Si. Consequentially, the copper silicide-coated graphite achieved better electrochemical performances in comparison with those of Si-coated graphite composites, where the initial Coulombic efficiency and the capacity retention at 30th cycle were improved by 7% and 39%, respectively (**Fig. 1. 16g**).

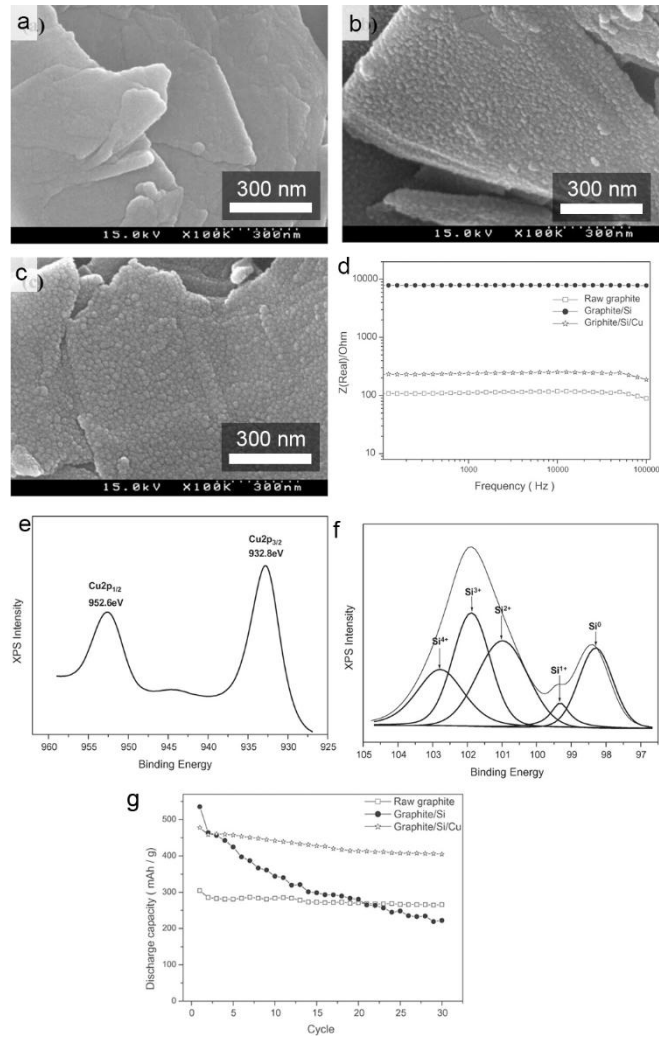


Figure 1. 16. copper silicide-coated graphite fabricated by PECVD and RF magnetron sputtering. a-c) SEM images showing the surface of (a) raw graphite, (b) Si-coated graphite, (c) copper silicide-coated graphite, respectively. d) AC current plot the conductivity for raw graphite, Si-coated graphite and copper silicide-coated graphite. e), f) XPS spectra of copper silicide-coated graphite for (e) Cu 2p and (f) Si 2p. (g) Discharge capacities of raw graphite, Si-coated graphite and copper silicide-coated graphite for 30 cycles. Copyright: Elsevier, 2006.

Recently, our group suggested the scalable Si-nanolayer-embedded graphite/carbon (SGC) composite via a simple thermal CVD using the customized rotatable furnace (**Fig. 1. 17a**).⁴⁷ This composite successfully achieved a homogeneous distribution of Si nanolayers on the whole surface of graphite, and it was also demonstrated to produce 5 kg per one batch (**Fig. 1. 17b**). As shown in the EDS mapping image in scanning TEM (STEM) (**Fig. 1. 17c**), the Si nanolayer is homogeneously deposited on both the graphite surface and beneath its inner pores. The amorphous carbon subsequently coats the Si nanolayer. The nano-sized Si layer effectively mitigates the lithiation-induced stress, as well as allowing an enhanced Li⁺ diffusivity and a good electrical contact derived from a strong adhesion on the graphite. Furthermore, the subsequent carbon coating layer promotes electric and ionic conductivity, and leads to stable SEI formation. As a result, the SGC composite achieved an excellent capacity retention (96% over 100 cycles) with an exceptional initial CE of 92%, even under challenging electrode conditions of high electrode density (1.6 g/cc), high areal capacity (> 3.3 mAh/cm²), and small amounts of binder (< 4 wt%) (**Fig. 1. 17d**). Furthermore, the lithiation mechanism of Si nanolayer coated-graphite was firstly investigated with *in situ* TEM (**Fig. 1. 17e, f**). It demonstrated that the lithiation of Si on the graphite could progress regardless of the mechanical interaction with the adjunct graphite layers, implying that the graphite layer supports lithium transport effectively along the carbon matrix without blocking the expansion of Si. With the modification of graphite, the Si nanolayer coating has been utilized to build better graphite/Si composite.

In summary, the application of CVD process is a facile method to synthesize a high-performance graphite/Si composites because of the following advantages^{47, 68, 145-147}: (1) High purity Si can be deposited on the graphite surface in nano-scale, uniformly. (2) Nano-sized Si provides a high Li⁺ reactivity and relieves the induced stress for repeated cycles. (3) These Si nanoparticles are strongly bonded to graphite matrix. (4) The graphite also acts as a buffer matrix for the accommodation of the volume expansion and offers a good electrochemical reversibility.

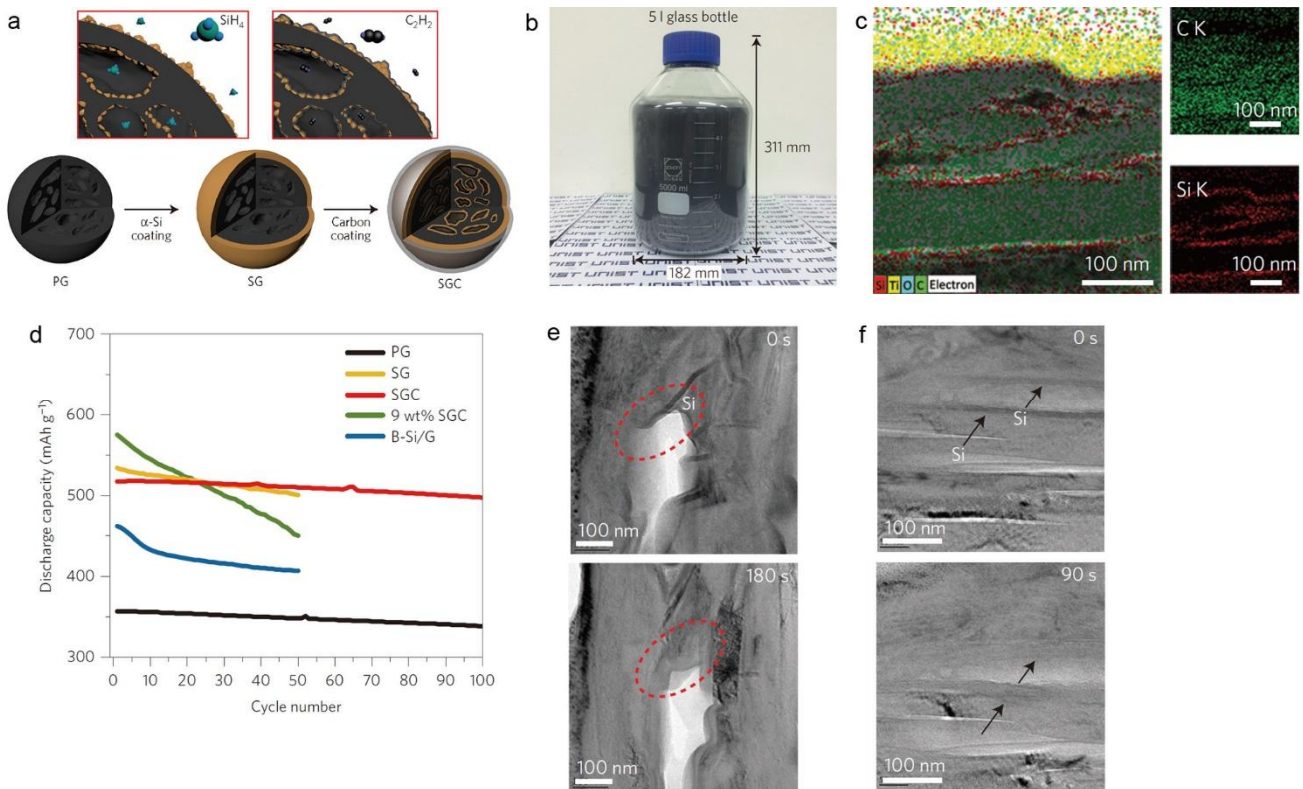


Figure 1. 17. Si-nanolayer-embedded graphite/carbon (SGC) composite. a) Schematic illustration of the fabrication process of SGC composite. b) Photograph of the fabricated SGC composite per batch. c) Cross-sectional STEM image for EDS mapping of SGC composite. d) Discharge capacities of SGC composite for 100 cycles, containing PG, SG, 9wt% SGC, and B-Si/G. e, f) Captured *in situ* TEM images for expansion of Si (e) on the surface of empty space and (f) between graphite layer, respectively. Copyright: Nature Publishing Group, 2016.

1.3.2.4 Liquid solidification method

The liquid solidification method has been widely used to synthesize the composite with more than two different materials. Briefly, two or more different solids are dispersed in the solvent with vigorous stirring to form a homogeneous suspension. As the solvent is evaporated, the solids are gradually agglomerated each other, and then the composite is formed.¹⁴⁸ In general, the homogeneous solution composed of the graphite, Si nanoparticle, and binding additives or conductive agents is used to synthesize the graphite/Si composite by this method. Such liquid solidification is relatively straightforward and simple method.^{64, 149-150} However, several parameters related to physical properties of input materials and synthetic processes have considerable influence on the particle size distribution and the morphology homogeneity of the composite, which are directly related to the electrochemical performances. Hence, comprehensive studies on these variables are necessary for the optimization of the graphite/Si composite.

To investigate the effect of synthetic parameters on the quality of composite and its electrochemical performance, Hiroyuki et al. synthesized the Si/carbon/graphite composites using different methods.¹⁵¹ In this study, the author demonstrated three types of the graphite/Si composite by mixing the Si nanopowder with a pitch, and then adding the graphite (Sample A), mixing the Si nanopowder, pitch, and graphite at once (Sample B), and milling after mixing all at once (Sample C). **Figure 1. 18a-c** exhibited the SEM images of each sample with the schematic of the composite. In case of sample A, Si particles embedded in the carbon and partially covered the surfaces of the graphite and carbon matrix. Sample B showed the weakly bonded Si and graphite to carbon matrix, and some of Si and graphite were detached from the composite. Whereas, sample C showed a homogeneous mixture consisted of Si and graphite with carbon matrix. In the electrochemical evaluation (**Fig. 1. 18d**), sample A exhibited the better capacity retention with higher initial CE among three types of the composite. The highest initial CE of sample A was attributed to the low surface area originated from carbon coated Si particles. Such results demonstrate that mixing Si and pitch before adding graphite makes Si entirely wrapped by carbon shell, and this coated carbon brings about relieved mechanical stress during cycling.

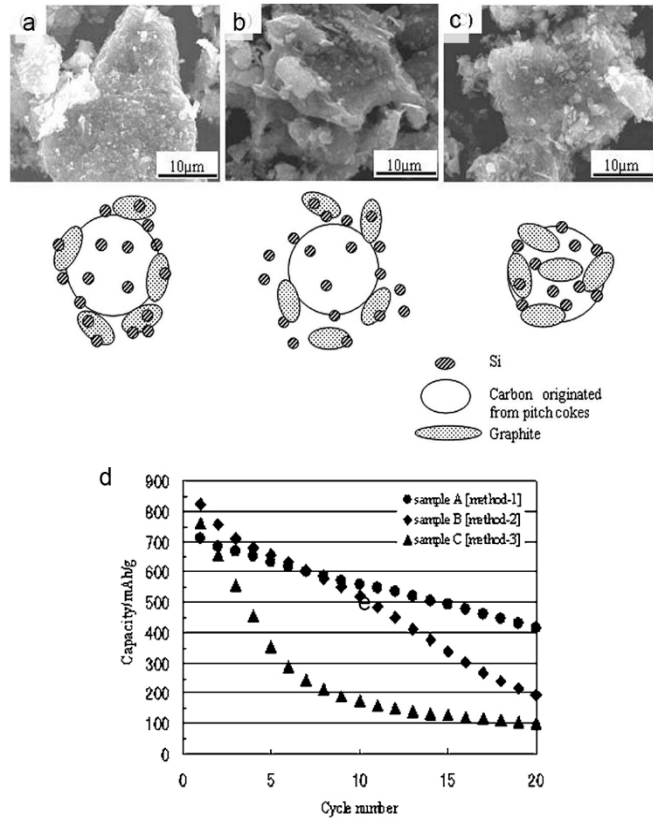


Figure 1. 18. The optimized structure of Si/carbon/graphite composite *via* liquid solidification method. a-c) SEM images with schematic morphologies for composites according to the different mixing order of Si, graphite, and pitch. d) Electrochemical cycle performance showing the effect of mixing order of Si, graphite, and pitch. Copyright: the Electrochemical Society, 2006.

As for the industrial approach, nano-Si/pitch/graphite composite has emerged as a feasible candidate. So Yeun Kim et al. synthesized Si/graphite composite using pitch-based carbon (Si-C-G) by the liquid solidification method with subsequent carbonization, in order to identify the effect of pitch-based carbon additive on the composite.⁶⁴ **Figure 1. 19a, b** presented the surface of Si-C-G composites and it demonstrates that Si nanopowders were uniformly embedded in the pitch carbon and attached to the graphite surface without any crack. In particular, the pitch carbon had several benefits in the graphite/Si composite system. Firstly, pitch exhibits the good elasticity which can accommodate severe volume change of Si for repeated cycling, thereby making it still attached to the graphite after several cycles.¹⁵² Moreover, pitch can provide an electrical network between graphite and Si by its good electrical conductivity.¹⁵³ In addition, microvoids, which were created during carbonization, facilitate the Li⁺ diffusion in the charge and discharge process. On the basis of these favorable influence of pitch-based carbon, the Si-C-G composites showed a stable electrode integrity, an excellent capacity retention with high initial CE, and an improved rate capability.

The commercial anode material company, BTR, also reported nano-Si/pitch/graphite composite with considering the practical material design factors including the specific capacity, the coulombic efficiency, and the cost.¹⁵⁴ They utilized the polyvinyl pyrrolidone (PVP) as a binder for agglomerating nano-Si, graphite, and pitch in ethanol. The dried products were made a spherical shape by a fusion machine, which was followed by the heat treatment at 900 °C for 3 h under N₂ atmosphere as shown in **Figure 1. 19c**. They successfully demonstrated its commercial feasibility with ~3000 mAh full-cell, where the composite was blended with graphite during fabrication of the electrode for a specific capacity of 480 mAh/g. It showed high initial Coulombic efficiency of 88.9% and stable cycling behavior with the capacity retention of 81% after 1200 cycles (**Fig. 19d, e**).

In short, the morphological and electrochemical properties of the composites synthesized by the liquid solidification can be easily varied depending on the mixing order, particle size of input materials, and the characteristics of additives. Therefore, elaborate optimization is required for improving the electrochemical performance.^{64, 151} Owing to the simplicity of the liquid solidification method, it has got a remarkable attention in terms of the commercialization of graphite/Si composite anodes.

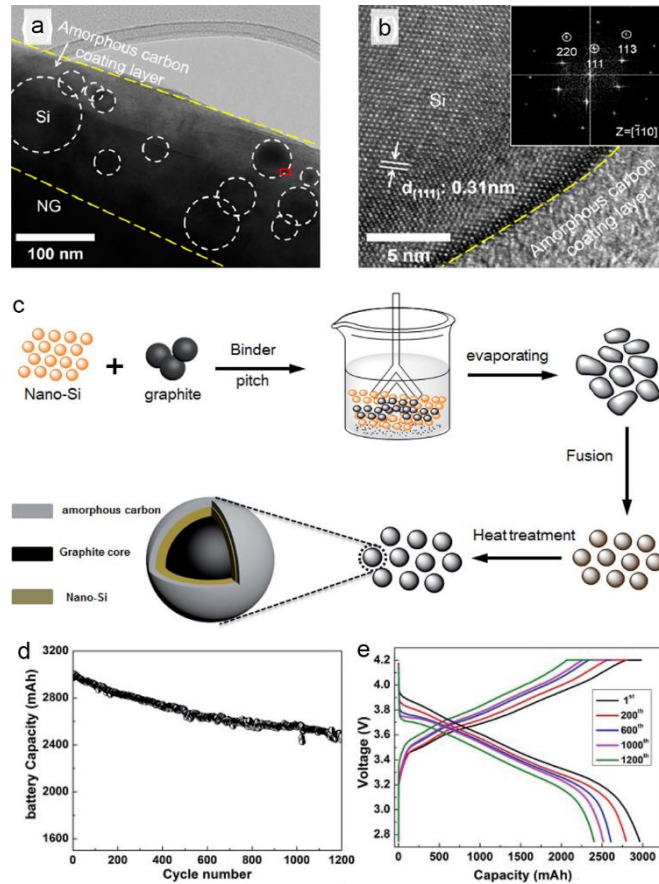


Figure 1. 19. Graphite/Si composites fabricated by liquid solidification method. a) HR-TEM image at the interfacial region of Si-C-G composites. b) HR-TEM image at the boundaries between Si and amorphous carbon coating layer of Si-C-G composites, with FFT patterns (inset). Copyright: American Chemical Society, 2016. c) Schematic illustration of fabrication process for the nano-Si/pitch/graphite composite. d) Discharge capacities of the nano-Si/pitch/graphite composite for 1200 cycles. e) Voltage profiles of the prototype full-cells at 1st, 200th, 600th, 1000th, and 1200th cycles. Copyright: Royal Society of Chemistry, 2018.

1.4. Critical factors for co-utilization of graphite and Si

How to better use graphite and Si in one electrode starts with comprehending each property of graphite and Si and their synergy effects. The co-utilization of graphite and Si is complicated because the property of Si is significantly different from that of graphite in every way and the way for the co-utilization significantly influences on the battery performance. Hence, in this section, the critical factors will be discussed with two categories, the material property and the co-utilization (**Fig. 1. 20**).

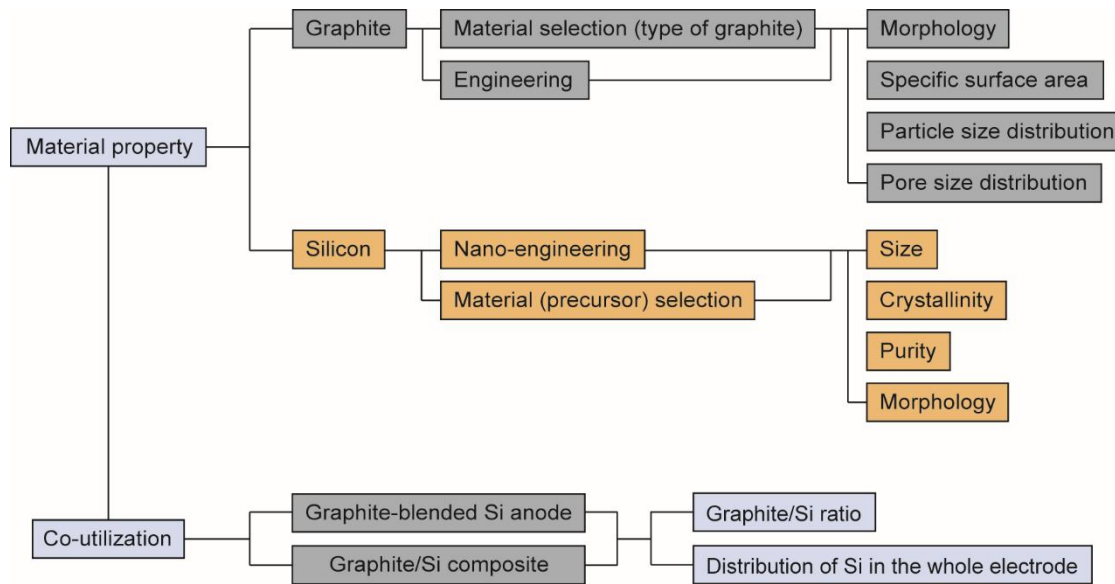


Figure 1. 20. Critical factors for designing graphite/Si composite and graphite-blended Si anode.

1.4.1 Material Property

1.4.1.1 Graphite

Graphite has been developed enough to be called as the miraculous anode material in every way including the low price and high performance. Accordingly, graphite plays a crucial role in improving the stability of the graphite/Si composite along with improving the electrical conductivity. When it comes to building the graphite/Si composite, graphite not only contributes to the capacity of the composite but also can become the matrix for Si with dispersing the volume expansion of Si and providing electrical contacts. The contribution of graphite to the electrochemical performance in graphite/Si composite could depend on its several properties, such as the type originated from the manufacturing process, the surface area, the porosity, and the size distribution.

Graphite can be classified into natural graphite and artificial graphite according to its manufacturing process. Natural graphite is mined in its natural state, so it is necessary to be purified and milled for the application on the battery electrode.¹⁵⁵ Generally, after the refining process, the natural graphite has

large surface area, where the electrochemically active edge planes can be easily exposed to the electrolyte. This morphology is kinetically beneficial for storing Li-ion in the structure, however, it would cause large amounts of the side reaction with the electrolyte because of the functional groups on the edge plane and residual impurities. In this regard, to reduce the unfavorable side reaction, the surface of the natural graphite is controlled by assembling the crushed natural graphite or transforming the morphology into the spherical shape.¹⁵⁶⁻¹⁵⁷ Additionally, the highly reactive surface is protected by the coating with other carbonaceous materials such as pitch, which could lower the surface area and alleviate the side reactions.¹⁵⁸⁻¹⁵⁹

On the other hand, the artificial graphite is synthesized by heating the cokes with tar and pitch at the high temperature (>2500 °C).¹⁶⁰⁻¹⁶² Owing to the synthetic process including hot isostatic pressing, the artificial graphite has smaller amounts of pores and specific surface area than that of natural graphite. Owing to this morphological characteristic, the edge plane of the artificial graphite is less exposed to the electrolyte, which results in slightly lower specific capacity than that of the natural graphite. However, obviously, it suffers less side reactions with electrolyte, leading to high initial CE and excellent cycling performance during cycling. Meanwhile, it is notable that the dense morphology of the artificial graphite is unfavorable to the calendaring process for high energy density. Therefore, in contrast to the natural graphite, the flake-shape is preferred for the facile calendaring process.

Meanwhile, the size of graphite can be controlled depending on its application. For example, the small-sized graphite is favorable to the high rate capability.¹⁶³⁻¹⁶⁴ The surface area originated from the size of graphite, where the small size one generally has large surface area, would affect the lithiation kinetics and the side reaction with the electrolyte as we discussed before. In summary, the performance contribution of graphite in graphite/Si composite can be diversely controlled with several factors such as morphology, specific surface, particle size distribution, and pore size distribution, which are derived from the type of graphite or its engineering.

1.4.1.2 Silicon

Owing to the high specific capacity of Si, Si has a major influence on the electrochemical performance of graphite/Si composites even with small contents because the deterioration of Si derived from the severe volume change governs the overall failure mechanism of graphite/Si composite. Therefore, addressing the failure mechanism of Si anodes within the graphite/Si composite is indispensable to develop better graphite/Si composite. In this regard, the established nano-engineering for Si anodes can be applied when fabricating the graphite/Si composite. It is widely acknowledged that the stress and strain from the volume change can be mitigated when the particle size becomes smaller.¹⁶⁵⁻¹⁶⁶ From the in situ TEM analysis, it turned out that Si nanoparticle did not fracture upon a single lithiation up to 150 nm³⁶ and 870 nm¹⁶⁷ for crystalline and amorphous one, respectively. Furthermore,

Si nanoparticle under 10 nm exhibited the elastic volume change after 40 cycles.¹⁶⁸ Therefore, the size control can address the failure mechanism of Si which starts with the mechanical degradation from huge volume change.

Recently, the relation between the particle size and the parasitic reaction of c-Li₁₅Si₄ with electrolytes was investigated.¹⁶⁹ The formation of c-Li₁₅Si₄ phase upon full lithiation has a detrimental effect on the battery performance, accompanying with high internal stresses and even particle cracking. The metastable c-Li₁₅Si₄ is rather reactive toward the alkyl carbonate based electrolytes, which results in the chemical parasitic reactions. Gao et al. successfully demonstrated the use of smaller Si nanoparticles (~60 nm) and fluoroethylene carbonate (FEC) additive stimulates the parasitic reactions of c-Li₁₅Si₄ with electrolytes, thereby leading to improved cycling performance with decreased specific capacity.

Dealing with the nano-sized Si accompanies two issues of the impurity and the oxidation. The typical scalable synthetic method of nano-sized Si is the top-down approach, which is mechanically milling Si particles into nanoparticles with extremely high-energy. In the mechanical milling process, the residual impurities in Si such as Al, Mn, Co, and so on, can make an alloy with Si which is electrochemically inactive.^{17, 170-172} Therefore, the elaborate impurity control is required to utilize the high specific capacity of Si effectively. Furthermore, the high-energy mechanical mill inevitably causes the oxidation of Si even if the process is conducted under the inert atmosphere. While the oxidation at the surface of Si can act as a buffer against the volume expansion, it sacrifices the specific capacity and brings about low initial Coulombic efficiency with irreversible side reaction. To remove silicon oxide at the surface, etching process is frequently carried out with hydrofluoric acid in the lab scale. However, it should be noted that the hydrofluoric acid bears the safety issue in the scale-up process.^{35, 42, 173} In this regards, the synthesis of nano-sized Si with silane gases, such as thermal pyrolysis, thermal vapor deposition, and laser ablation, can be promising method, which have advantages in the facile size control and high purity. The material cost for silane gases could be regarded as rather expensive. However, the scalable and simple synthetic process could present price competitiveness.

The morphology of Si has been variously designed in order to address the mechanical degradation from huge volume change. The porous or void-containing structure can mitigate the intensification of strain and giving additional space for expansion, thereby keeping the material intact and improving the electrode stability. However, it should be considered that the calendaring process should be accompanied to achieve high electrode density, which is essential for commercial high energy LIBs. The calendaring process can damage the morphology even in the graphite-blended electrode, specifically the intended porous structure or void spaces. In this regards, on the one hand, the compact structure, where the void spaces are filled up with the carbon matrix or Si is surrounded by other inactive phases, has deemed feasible in high energy density design.¹⁷⁴ The elaborate morphology design with

considering the calendaring is necessary for improving both of cycling performance and volumetric energy density.

1.4.2. Co-utilization

First of all, the ratio of Si to graphite determines the specific capacity. The high specific capacity can improve the volumetric energy density by reducing the use of active materials and electrode thickness with comparable electrode density. However, it is obvious that the increase of specific capacity has a risk of severe electrode swelling and electrode instability during repeated cycling. Besides, owing to the different (de)lithiation potentials of graphite and Si, the operation voltage depends on the utilized capacity ratio from Si to graphite. The high content of Si in the electrode tends to have lower operation voltage in the full cell. Therefore, in order to achieve high volumetric energy density in commercial LIBs, it is important to determine the proper ratio for the material design of Si/graphite composite and the cell design in the graphite-blended Si anode.

With the same content of Si in the electrode, the electrode swelling highly depends on the distribution of Si. If Si is localized in a certain location of the electrode, the volume expansion of Si is intensified, leading to huge electrode swelling. In order to verify this relation, we have explored how the size of Si, and distribution of Si and graphite in an electrode affect the battery performance. Two types of typical graphite/Si composites were synthesized *via* liquid solidification (denoted as LSG) and thermal CVD methods (denoted as CSG), respectively, which have different Si distribution in composites. The detailed sample preparation can be found in Supporting Information. On the other hand, the high-capacity Si material for graphite-blending was fabricated by the spray-drying of a mixture containing Si nanoparticles and pitch carbon (denoted as SSP), which exhibits initial specific capacity of 1830 mAh g⁻¹ with initial CE of 87.7%. For a rational comparison, all electrodes were fixed with a specific reversible capacity of 535 mAh g⁻¹, and the electrochemical evaluation was carried out under the industrial condition with high electrode density (1.6 g/cc), high areal capacity (> 3.5 mAh/cm²), and small amounts of binder (3 wt%). For SSP anode, the commercial graphite was blended with SSP at a ratio of 8.5 wt% (denoted as SSP/G).

As shown in **Figure 1. 21a,b**, SSP/G, LSG, and CSG exhibited capacity retention of 90.8%, 94.2%, and 95.7% after 50 cycles, with the initial CE of 87.4%, 87.6%, and 92.6% respectively. Cycling CE, which acts as an indicator of electrochemical reversibility at each cycle, was presented in **Figure 1. 21c**. According to the plot, cycling CE of LSG and SSP/G reached at 99.5% around 30 cycles with sluggish increment, and the average CE of them was 99.0% and 99.1% for 50 cycles, respectively. On the other hand, the SGC attained CE of 99.5% after only 9 cycles with a steep rise in the cycling CE and also recorded average CE of 99.5% for 50 cycles with retaining the highest value during all cycles.

In addition, we have investigated the macroscopic variation of the electrode expansion and the microstructural changes of the active materials after cycling. As presented in **Figure 1. 21d**, SSP/G showed the highest electrode thickness change of 141% at 50th lithiated state. The electrode swelling behavior indicates that the electrode was rapidly distorted during early 10 cycles with electrical isolation, then the cell degradation proceeded with gradual electrode swelling for prolonged cycling. While both LSG and CSG exhibited relatively gentle electrode expansion trends than SSP/G, CSG showed a slightly lower thickness change (80.8%) than that of LSG (98.8%) and it is well accorded with the cycle performance.

Furthermore, the post-cycling microstructural changes of electrodes were observed. As shown in the cross-sectional SEM image of SSP/G (**Fig. 1. 22a, b**), SSP/G became severely rugged with immoderately expanded SSP, leading to loss of the electrical network between active materials. Besides, the thick SEI layer was formed on the localized cracks around SSP particles and distorted graphite. For the LSG electrode (**Fig. 1. 22c, d**), the solidified layer of pitch/Si on the graphite surface was torn and swelled after cycling. Especially on the solidified layer, SEI layer is piled up which would interrupt the transport of Li⁺ and electron transfer. Meanwhile, it is difficult for the CSG electrode to find bumpiness or disordered surface (**Fig. 1. 22e, f**). The cross-sectional view of CSG shows that Si nanolayer is located both on the surface and inner pores of graphite, indicating homogeneous distribution of Si in composites. Accordingly, CSG succeeded in exhibiting mitigated electrode swelling and stable SEI formation.

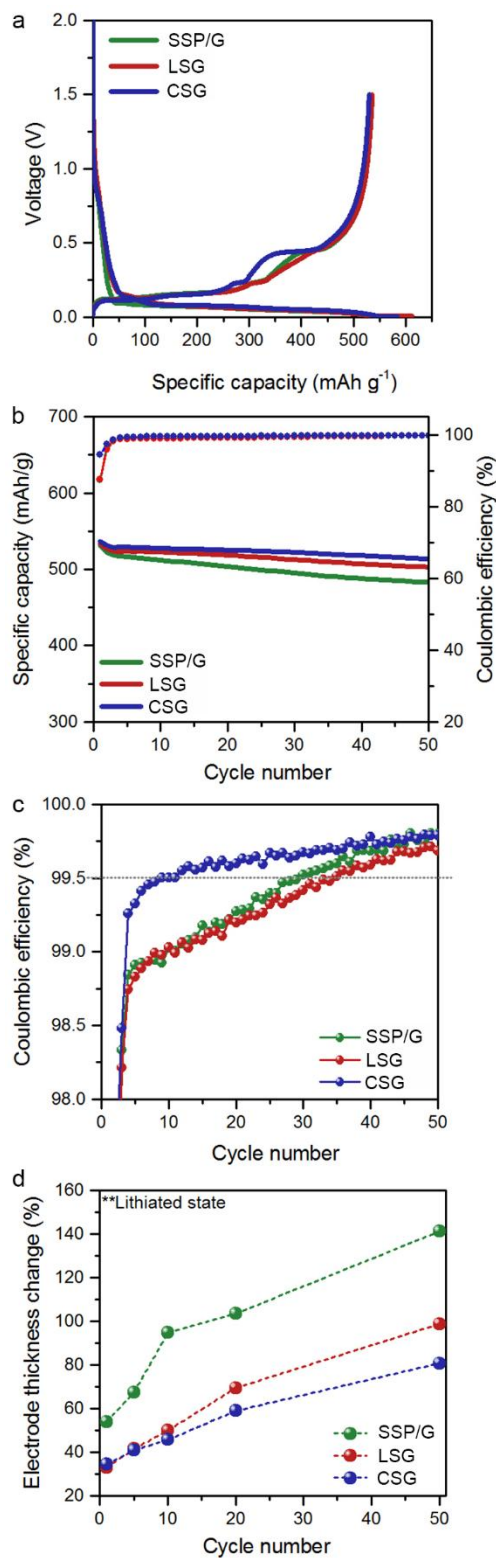


Figure 1. 21. Electrochemical characterization of SSP/G, LSG, and CSG. a) Voltage profiles at the first cycle measured at 0.1 C. b) Discharge capacities and cycling CEs of the anodes for 50 cycles. c) Magnified CEs at each cycle plotted from 98 to 100% of (b). d) Change of electrode thickness at lithiated state during 50 cycles.

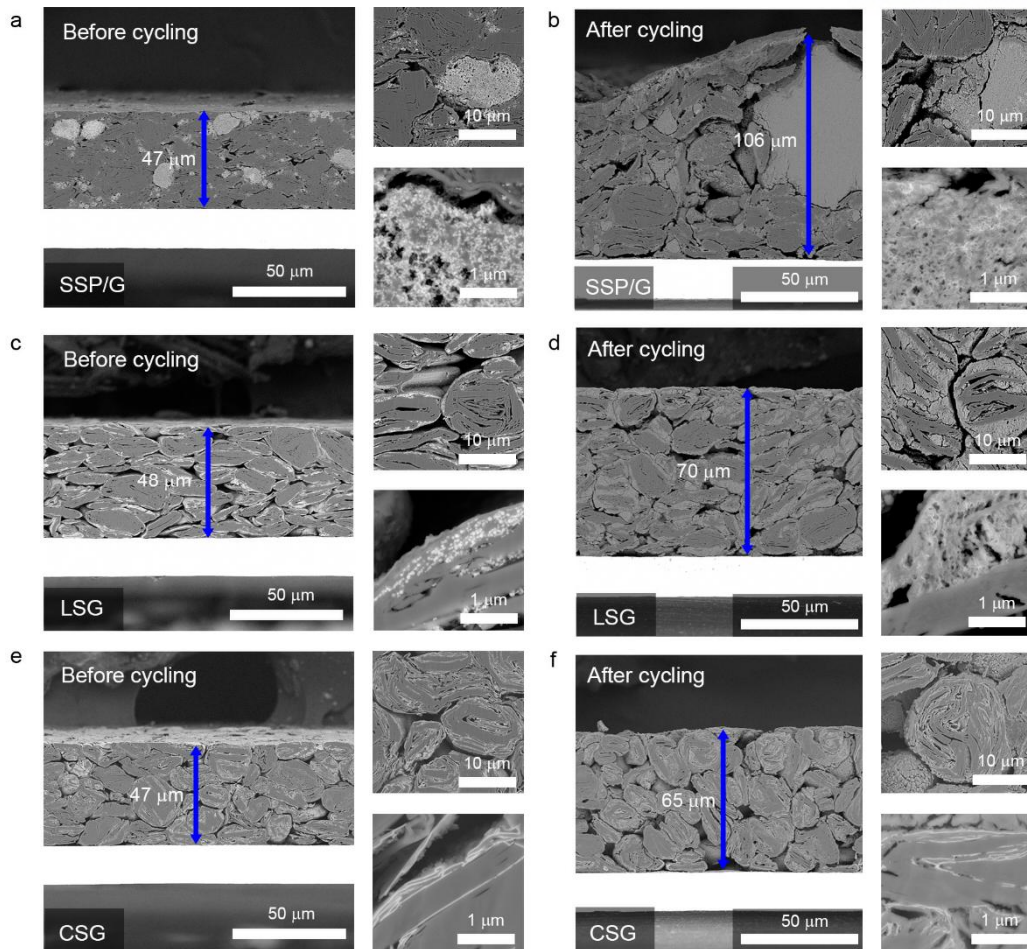


Figure 1. 22. SEM images of electrode changes before and after 50 cycles regarding SSP/G, LSG, and CSG. a-f) Cross-sectional views before cycling and after 50 cycles with magnified images.

Our experimental verification demonstrates that the electrode swelling and electrochemical performance are strongly dependent on the Si distribution in the electrode. The specific relation is illustrated in **Figure 1. 23**. In summary, the homogeneously distributed Si in the electrode results in the mild electrode swelling compared to that of the localized Si in the electrode, consequently influencing on the battery. Accordingly, the material design for the homogeneous distribution of Si in the electrode is required to achieve low electrode swelling. For high-capacity Si anode, the fine particle size is favorable which can be effectively dispersed with graphite. With regard to the graphite/Si composite, the distribution of Si in the electrode could be more homogeneous than that of graphite-blended Si anode. Besides, if the specific capacity of graphite/Si composite is designed to be similar with the target capacity, the homogeneity could be improved and thereby achieve low electrode swelling.

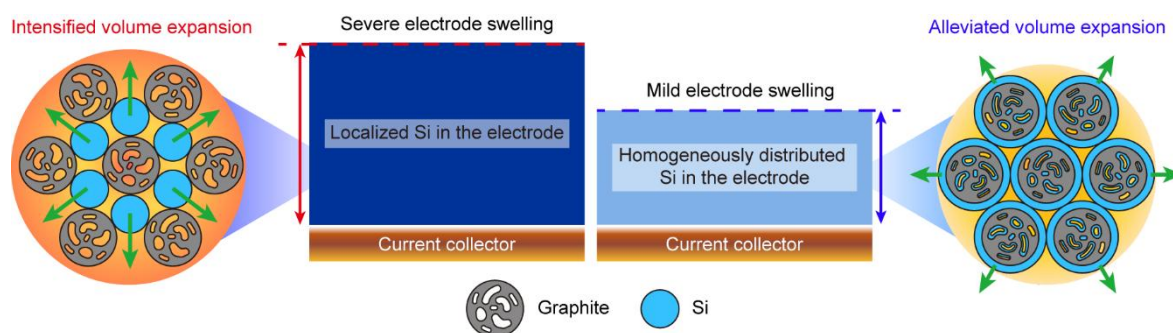


Figure 1. 23. A Schematic illustration of electrode swelling behavior depending on Si distribution.

1.5. Conclusion and outlook

In this review, we have highlighted the necessity for the co-utilization of graphite and Si in terms of commercialization and reviewed the research progress of the graphite/Si anode. Finally, we have discussed the critical factors regarding the co-utilization of graphite and Si for commercial high energy LIBs. We have presented the experimental comparison between three kinds of graphite/Si anode for elucidating the influence of the different size and distribution Si on electrochemical performance. Several suggestions with respect to the co-utilization of graphite and Si for the commercialization are presented as follows:

1) Until now, graphite/Si anodes have been mainly suggested for demonstrating their innovative strategies with superior performances. However, in order to facilitate the further progress of the graphite/Si anode, it is also necessary to investigate the interaction of graphite and Si with their electrochemical behavior in detail. Furthermore, the electrochemical properties of graphite/Si anodes under diverse operating conditions such as a temperature, a (dis)charging rate, and a type of cell packaging needs to be studied. The elaborate examination will give a new direction for the development

of commercially viable graphite/Si anodes.

2) Regarding the development of the graphite/Si anode for high-energy LIB, both graphite and Si should be engineered aiming at finding their suitable properties when blended with the other or built in the composite. Together with the electrochemical property of each material, the compatibility would play a crucial role in determining its performance, which has not been intensively studied so far. Extending with the critical factors which we have covered, comprehensive studies for the co-utilization of graphite and Si are necessary.

3) In order to commercialize the graphite/Si anode, the strict requirement for the electrochemical performance and the material price must be satisfied. The short-term objective for the graphite/Si anode is to achieve competitive electrochemical performances with the specific capacity of 500mAh/g compared to those of commercial graphite. Specifically, it can include the improved volumetric capacity (800 mAh/cc), high initial CE (> 90%), cycle life (full-cell capacity retention of 80% @ 500 cycles), and low electrode swelling (initial swelling of 20% and stabilized behavior during cycling). This target The target of material price is considered as the similar level with artificial graphite in terms of the price over specific capacity (USD g mAh⁻¹).

4) Finally, to confirm a true advance in this field, the electrochemical testing should be carried out in constant manners for high volumetric energy density. Besides, the related information should be thoroughly provided to avoid ambiguity because the electrochemical performance in each laboratory is highly sensitive to subsidiary factors such as other cell components and manufacturing skill. In this regard, the mutual consent of battery researchers on testing protocol would be required.

1.6. References

1. Dunn, B.; Kamath, H.; Tarascon, J.-M., Electrical Energy Storage for the Grid: A Battery of Choices. *Science* **2011**, *334* (6058), 928-935.
2. Blomgren, G. E., The Development and Future of Lithium Ion Batteries. *J Electrochem Soc* **2017**, *164* (1), A5019-A5025.
3. Armand, M.; Tarascon, J.-M., Building better batteries. *Nature* **2008**, *451* (7179), 652-657.
4. Cano, Z. P.; Banham, D.; Ye, S.; Hintennach, A.; Lu, J.; Fowler, M.; Chen, Z., Batteries and fuel cells for emerging electric vehicle markets. *Nature Energy* **2018**, *3* (4), 279-289.
5. Tarascon, J. M.; Armand, M., Issues and challenges facing rechargeable lithium batteries. *Nature* **2001**, *414* (6861), 359-67.
6. Aricò, A. S.; Bruce, P.; Scrosati, B.; Tarascon, J. M.; Van Schalkwijk, W., Nanostructured materials for advanced energy conversion and storage devices. *Nat Mater* **2005**, *4* (5), 366-377.
7. Goodenough, J. B.; Kim, Y., Challenges for Rechargeable Li Batteries. *Chem Mater* **2010**, *22* (3), 587-603.
8. Yim, C. H.; Niketic, S.; Salem, N.; Naboka, O.; Abu-Lebdeh, Y., Towards improving the practical energy density of Li-Ion batteries: Optimization & evaluation of silicon:graphite composites in full cells. *J Electrochem Soc* **2017**, *164* (1), A6294-A6302.
9. Du, Z.; Dunlap, R. A.; Obrovac, M. N., High Energy Density Calendered Si Alloy/Graphite Anodes. *Journal of The Electrochemical Society* **2014**, *161* (10), A1698-A1705.
10. Chae, S.; Ko, M.; Kim, K.; Ahn, K.; Cho, J., Confronting Issues of the Practical Implementation of Si Anode in High-Energy Lithium-Ion Batteries. *Joule* **2017**, *1* (1), 47-60.
11. Freunberger, S. A., True performance metrics in beyond-intercalation batteries. *Nature Energy* **2017**, *2*, 17091.
12. Kwade, A.; Haselrieder, W.; Leithoff, R.; Modlinger, A.; Dietrich, F.; Droeder, K., Current status and challenges for automotive battery production technologies. *Nature Energy* **2018**, *3* (4), 290-300.
13. Obrovac, M. N.; Krause, L. J., Reversible cycling of crystalline silicon powder. *Journal of the Electrochemical Society* **2007**, *154* (2), A103-A108.
14. Obrovac, M. N.; Christensen, L., Structural Changes in Silicon Anodes during Lithium Insertion/Extraction. *Electrochemical and Solid-State Letters* **2004**, *7* (5), A93-A96.
15. Manev, V.; Naidenov, I.; Puresheva, B.; Zlatilova, P.; Pistoia, G., Electrochemical performance of natural Brazilian graphite as anode material for lithium-ion rechargeable cells. *J Power Sources* **1995**, *55* (2), 211-215.
16. Yazami, R.; Zaghbi, K.; Deschamps, M., Carbon fibres and natural graphite as negative

- electrodes for lithium ion-type batteries. *J Power Sources* **1994**, 52 (1), 55-59.
17. Jin, Y.; Zhu, B.; Lu, Z.; Liu, N.; Zhu, J., Challenges and Recent Progress in the Development of Si Anodes for Lithium-Ion Battery. *Adv. Energy Mater.* **2017**.
 18. Park, C.-M.; Kim, J.-H.; Kim, H.; Sohn, H.-J., Li-alloy based anode materials for Li secondary batteries. *Chemical Society Reviews* **2010**, 39 (8), 3115-3141.
 19. Zhang, W.-J., A review of the electrochemical performance of alloy anodes for lithium-ion batteries. *Journal of Power Sources* **2011**, 196 (1), 13-24.
 20. McDowell, M. T.; Lee, S. W.; Harris, J. T.; Korgel, B. A.; Wang, C.; Nix, W. D.; Cui, Y., In Situ TEM of Two-Phase Lithiation of Amorphous Silicon Nanospheres. *Nano Letters* **2013**, 13 (2), 758-764.
 21. Ko, M.; Chae, S.; Cho, J., Challenges in Accommodating Volume Change of Si Anodes for Li-Ion Batteries. *ChemElectroChem* **2015**, 2 (11), 1645-1651.
 22. McDowell, M. T.; Lee, S. W.; Nix, W. D.; Cui, Y., 25th Anniversary Article: Understanding the Lithiation of Silicon and Other Alloying Anodes for Lithium-Ion Batteries. *Advanced Materials* **2013**, 25 (36), 4966-4985.
 23. Kalnaus, S.; Rhodes, K.; Daniel, C., A study of lithium ion intercalation induced fracture of silicon particles used as anode material in Li-ion battery. *Journal of Power Sources* **2011**, 196 (19), 8116-8124.
 24. Yoon, T.; Nguyen, C. C.; Seo, D. M.; Lucht, B. L., Capacity Fading Mechanisms of Silicon Nanoparticle Negative Electrodes for Lithium Ion Batteries. *J Electrochem Soc* **2015**, 162 (12), A2325-A2330.
 25. Aurbach, D., Review of selected electrode–solution interactions which determine the performance of Li and Li ion batteries. *J Power Sources* **2000**, 89 (2), 206-218.
 26. Chan, C. K.; Ruffo, R.; Hong, S. S.; Cui, Y., Surface chemistry and morphology of the solid electrolyte interphase on silicon nanowire lithium-ion battery anodes. *J Power Sources* **2009**, 189 (2), 1132-1140.
 27. Verma, P.; Maire, P.; Novák, P., A review of the features and analyses of the solid electrolyte interphase in Li-ion batteries. *Electrochim Acta* **2010**, 55 (22), 6332-6341.
 28. Wu, H.; Cui, Y., Designing nanostructured Si anodes for high energy lithium ion batteries. *Nano Today* **2012**, 7 (5), 414-429.
 29. Li, J.-Y.; Xu, Q.; Li, G.; Yin, Y.-X.; Wan, L.-J.; Guo, Y.-G., Research progress regarding Si-based anode materials towards practical application in high energy density Li-ion batteries. *Materials Chemistry Frontiers* **2017**, 1 (9), 1691-1708.
 30. Ko, M.; Oh, P.; Chae, S.; Cho, W.; Cho, J., Considering Critical Factors of Li-rich Cathode and Si Anode Materials for Practical Li-ion Cell Applications. *Small* **2015**, 11 (33), 4058-4073.

31. Kim, H.; Lee, E.-J.; Sun, Y.-K., Recent advances in the Si-based nanocomposite materials as high capacity anode materials for lithium ion batteries. *Materials Today* **2014**, *17* (6), 285-297.
32. Ryu, J. H.; Kim, J. W.; Sung, Y.-E.; Oh, S. M., Failure Modes of Silicon Powder Negative Electrode in Lithium Secondary Batteries. *Electrochemical and Solid-State Letters* **2004**, *7* (10), A306-A309.
33. Gor, G. Y.; Cannarella, J.; Prévost, J. H.; Arnold, C. B., A Model for the Behavior of Battery Separators in Compression at Different Strain/Charge Rates. *J Electrochem Soc* **2014**, *161* (11), F3065-F3071.
34. Li, M.; Lu, J.; Chen, Z.; Amine, K., 30 Years of Lithium-Ion Batteries. *Adv. Mater.* **2018**, *30* (33).
35. Lin, D.; Lu, Z.; Hsu, P.-C.; Lee, H. R.; Liu, N.; Zhao, J.; Wang, H.; Liu, C.; Cui, Y., A high tap density secondary silicon particle anode fabricated by scalable mechanical pressing for lithium-ion batteries. *Energy & Environmental Science* **2015**, *8* (8), 2371-2376.
36. Liu, X. H.; Zhong, L.; Huang, S.; Mao, S. X.; Zhu, T.; Huang, J. Y., Size-dependent fracture of silicon nanoparticles during lithiation. *ACS Nano* **2012**, *6* (2), 1522-1531.
37. Jeong, G.; Kim, J.-G.; Park, M.-S.; Seo, M.; Hwang, S. M.; Kim, Y.-U.; Kim, Y.-J.; Kim, J. H.; Dou, S. X., Core-Shell Structured Silicon Nanoparticles@TiO_{2-x}/Carbon Mesoporous Microfiber Composite as a Safe and High-Performance Lithium-Ion Battery Anode. *Acs Nano* **2014**, *8* (3), 2977-2985.
38. Lee, J. I.; Ko, Y.; Shin, M.; Song, H. K.; Choi, N. S.; Kim, M. G.; Park, S., High-performance silicon-based multicomponent battery anodes produced via synergistic coupling of multifunctional coating layers. *Energy and Environmental Science* **2015**, *8* (7), 2075-2084.
39. Chan, C. K.; Peng, H.; Liu, G.; McIlwrath, K.; Zhang, X. F.; Huggins, R. A.; Cui, Y., High-performance lithium battery anodes using silicon nanowires. *Nat Nanotechnol* **2007**, *3*, 31.
40. Wu, H.; Chan, G.; Choi, J. W.; Ryu, I.; Yao, Y.; McDowell, M. T.; Lee, S. W.; Jackson, A.; Yang, Y.; Hu, L.; Cui, Y., Stable cycling of double-walled silicon nanotube battery anodes through solid-electrolyte interphase control. *Nat Nanotechnol* **2012**, *7*, 310.
41. Liu, N.; Wu, H.; McDowell, M. T.; Yao, Y.; Wang, C.; Cui, Y., A Yolk-Shell Design for Stabilized and Scalable Li-Ion Battery Alloy Anodes. *Nano Letters* **2012**, *12* (6), 3315-3321.
42. Liu, N.; Lu, Z.; Zhao, J.; McDowell, M. T.; Lee, H.-W.; Zhao, W.; Cui, Y., A pomegranate-inspired nanoscale design for large-volume-change lithium battery anodes. *Nat Nanotechnol* **2014**, *9*, 187.
43. Yao, Y.; McDowell, M. T.; Ryu, I.; Wu, H.; Liu, N.; Hu, L.; Nix, W. D.; Cui, Y., Interconnected Silicon Hollow Nanospheres for Lithium-Ion Battery Anodes with Long Cycle Life. *Nano Letters* **2011**, *11* (7), 2949-2954.

44. Lu, Z.; Liu, N.; Lee, H.-W.; Zhao, J.; Li, W.; Li, Y.; Cui, Y., Nonfilling Carbon Coating of Porous Silicon Micrometer-Sized Particles for High-Performance Lithium Battery Anodes. *ACS Nano* **2015**, *9* (3), 2540-2547.
45. Szczech, J. R.; Jin, S., Nanostructured silicon for high capacity lithium battery anodes. *Energy & Environmental Science* **2011**, *4* (1), 56-72.
46. Kim, S.-O.; Manthiram, A., A facile, low-cost synthesis of high-performance silicon-based composite anodes with high tap density for lithium-ion batteries. *J Mater Chem A* **2015**, *3* (5), 2399-2406.
47. Ko, M.; Chae, S.; Ma, J.; Kim, N.; Lee, H.-W.; Cui, Y.; Cho, J., Scalable synthesis of silicon-nanolayer-embedded graphite for high-energy lithium-ion batteries. *Nature Energy* **2016**, *1*, 16113.
48. Chae, S.; Ko, M.; Park, S.; Kim, N.; Ma, J.; Cho, J., Micron-sized Fe–Cu–Si ternary composite anodes for high energy Li-ion batteries. *Energy & Environmental Science* **2016**, *9* (4), 1251-1257.
49. Chae, S.; Kim, N.; Ma, J.; Cho, J.; Ko, M., One-to-One Comparison of Graphite-Blended Negative Electrodes Using Silicon Nanolayer-Embedded Graphite versus Commercial Benchmarking Materials for High-Energy Lithium-Ion Batteries. *Adv. Energy Mater.* **2017**, *7* (15), 1700071.
50. Chevrier, V. L.; Liu, L.; Le, D. B.; Lund, J.; Molla, B.; Reimer, K.; Krause, L. J.; Jensen, L. D.; Figgemeier, E.; Eberman, K. W., Evaluating Si-Based Materials for Li-Ion Batteries in Commercially Relevant Negative Electrodes. *J Electrochem Soc* **2014**, *161* (5), A783-A791.
51. Dash, R.; Pannala, S., Theoretical Limits of Energy Density in Silicon-Carbon Composite Anode Based Lithium Ion Batteries. *Scientific Reports* **2016**, *6*, 27449.
52. Li, X.; Yan, P.; Xiao, X.; Woo, J. H.; Wang, C.; Liu, J.; Zhang, J.-G., Design of porous Si/C-graphite electrodes with long cycle stability and controlled swelling. *Energy Environ Sci* **2017**, *10* (6), 1427-1434.
53. Liang, B.; Liu, Y.; Xu, Y., Silicon-based materials as high capacity anodes for next generation lithium ion batteries. *J Power Sources* **2014**, *267*, 469-490.
54. Casimir, A.; Zhang, H.; Ogoke, O.; Amine, J. C.; Lu, J.; Wu, G., Silicon-based anodes for lithium-ion batteries: Effectiveness of materials synthesis and electrode preparation. *Nano Energy* **2016**, *27*, 359-376.
55. Terranova, M. L.; Orlanducci, S.; Tamburri, E.; Guglielmotti, V.; Rossi, M., Si/C hybrid nanostructures for Li-ion anodes: An overview. *J Power Sources* **2014**, *246*, 167-177.
56. Philipp, A., Editorial: The Energy Challenge, Batteries, and Why Simple Math Matters. *Angewandte Chemie International Edition* **2018**, *57* (23), 6710-6711.

57. Schmuch, R.; Wagner, R.; Hörpel, G.; Placke, T.; Winter, M., Performance and cost of materials for lithium-based rechargeable automotive batteries. *Nature Energy* **2018**, *3* (4), 267-278.
58. Jeong, G.; Kim, Y.-U.; Kim, H.; Kim, Y.-J.; Sohn, H.-J., Prospective materials and applications for Li secondary batteries. *Energy & Environmental Science* **2011**, *4* (6), 1986-2002.
59. Gogotsi, Y.; Simon, P., True Performance Metrics in Electrochemical Energy Storage. *Science* **2011**, *334* (6058), 917-918.
60. Obrovac, M. N.; Chevrier, V. L., Alloy Negative Electrodes for Li-Ion Batteries. *Chemical Reviews* **2014**, *114* (23), 11444-11502.
61. Lin, L.; Xu, X.; Chu, C.; Majeed, M. K.; Yang, J., Mesoporous Amorphous Silicon: A Simple Synthesis of a High-Rate and Long-Life Anode Material for Lithium-Ion Batteries. *Angewandte Chemie International Edition* **2016**, *55* (45), 14063-14066.
62. Ryu, J.; Hong, D.; Choi, S.; Park, S., Synthesis of Ultrathin Si Nanosheets from Natural Clays for Lithium-Ion Battery Anodes. *Acs Nano* **2016**, *10* (2), 2843-2851.
63. Lee, B. S.; Yoon, J.; Jung, C.; Kim, D. Y.; Jeon, S. Y.; Kim, K. H.; Park, J. H.; Park, H.; Lee, K. H.; Kang, Y. S.; Park, J. H.; Jung, H.; Yu, W. R.; Doo, S. G., Silicon/Carbon Nanotube/BaTiO₃ Nanocomposite Anode: Evidence for Enhanced Lithium-Ion Mobility Induced by the Local Piezoelectric Potential. *Acs Nano* **2016**, *10* (2), 2617-2627.
64. Kim, S. Y.; Lee, J.; Kim, B.-H.; Kim, Y.-J.; Yang, K. S.; Park, M.-S., Facile Synthesis of Carbon-Coated Silicon/Graphite Spherical Composites for High-Performance Lithium-Ion Batteries. *ACS Applied Materials & Interfaces* **2016**, *8* (19), 12109-12117.
65. Chen, Y.; Li, Y.; Wang, Y.; Fu, K.; Danner, V. A.; Dai, J.; Lacey, S. D.; Yao, Y.; Hu, L., Rapid, in Situ Synthesis of High Capacity Battery Anodes through High Temperature Radiation-Based Thermal Shock. *Nano Letters* **2016**, *16* (9), 5553-5558.
66. Li, Y.; Yan, K.; Lee, H.-W.; Lu, Z.; Liu, N.; Cui, Y., Growth of conformal graphene cages on micrometre-sized silicon particles as stable battery anodes. *Nature Energy* **2016**, *1*, 15029.
67. Xu, Q.; Li, J. Y.; Sun, J. K.; Yin, Y. X.; Wan, L. J.; Guo, Y. G., Watermelon-Inspired Si/C Microspheres with Hierarchical Buffer Structures for Densely Compacted Lithium-Ion Battery Anodes. *Adv. Energy Mater.* **2017**, *7* (3).
68. Kim, N.; Chae, S.; Ma, J.; Ko, M.; Cho, J., Fast-charging high-energy lithium-ion batteries via implantation of amorphous silicon nanolayer in edge-plane activated graphite anodes. *Nature Communications* **2017**, *8* (1), 812.
69. Zhang, X.; Qiu, X.; Kong, D.; Zhou, L.; Li, Z.; Li, X.; Zhi, L., Silicene Flowers: A Dual Stabilized Silicon Building Block for High-Performance Lithium Battery Anodes. *Acs Nano* **2017**, *11* (7), 7476-7484.

70. Jin, Y.; Li, S.; Kushima, A.; Zheng, X.; Sun, Y.; Xie, J.; Sun, J.; Xue, W.; Zhou, G.; Wu, J.; Shi, F.; Zhang, R.; Zhu, Z.; So, K.; Cui, Y.; Li, J., Self-healing SEI enables full-cell cycling of a silicon-majority anode with a coulombic efficiency exceeding 99.9%. *Energy & Environmental Science* **2017**, *10* (2), 580-592.
71. Shi, L.; Pang, C.; Chen, S.; Wang, M.; Wang, K.; Tan, Z.; Gao, P.; Ren, J.; Huang, Y.; Peng, H.; Liu, Z., Vertical Graphene Growth on SiO Microparticles for Stable Lithium Ion Battery Anodes. *Nano Letters* **2017**, *17* (6), 3681-3687.
72. Nie, P.; Liu, X.; Fu, R.; Wu, Y.; Jiang, J.; Dou, H.; Zhang, X., Mesoporous Silicon Anodes by Using Polybenzimidazole Derived Pyrrolic N-Enriched Carbon toward High-Energy Li-Ion Batteries. *ACS Energy Letters* **2017**, *2* (6), 1279-1287.
73. Lee, S. J.; Kim, H. J.; Hwang, T. H.; Choi, S.; Park, S. H.; Deniz, E.; Jung, D. S.; Choi, J. W., Delicate Structural Control of Si-SiO_x-C Composite via High-Speed Spray Pyrolysis for Li-Ion Battery Anodes. *Nano Letters* **2017**, *17* (3), 1870-1876.
74. Fang, S.; Tong, Z.; Nie, P.; Liu, G.; Zhang, X., Raspberry-like Nanostructured Silicon Composite Anode for High-Performance Lithium-Ion Batteries. *ACS Applied Materials and Interfaces* **2017**, *9* (22), 18766-18773.
75. Kim, N.; Park, H.; Yoon, N.; Lee, J. K., Zeolite-Templated Mesoporous Silicon Particles for Advanced Lithium-Ion Battery Anodes. *Acs Nano* **2018**, *12* (4), 3853-3864.
76. Lee, P. K.; Tan, T.; Wang, S.; Kang, W.; Lee, C. S.; Yu, D. Y. W., Robust Micron-Sized Silicon Secondary Particles Anchored by Polyimide as High-Capacity, High-Stability Li-Ion Battery Anode. *ACS Applied Materials and Interfaces* **2018**, *10* (40), 34132-34139.
77. Xu, Q.; Sun, J. K.; Yin, Y. X.; Guo, Y. G., Facile Synthesis of Blocky SiO_x/C with Graphite-Like Structure for High-Performance Lithium-Ion Battery Anodes. *Adv. Funct Mater.* **2018**, *28* (8).
78. Park, J.-B.; Ham, J.-S.; Shin, M.-S.; Park, H.-K.; Lee, Y.-J.; Lee, S.-M., Synthesis and electrochemical characterization of anode material with titanium-silicon alloy solid core/nanoporous silicon shell structures for lithium rechargeable batteries. *J Power Sources* **2015**, *299*, 537-543.
79. Winter, M.; Besenhard, J. O.; Spahr, M. E.; Novák, P., Insertion Electrode Materials for Rechargeable Lithium Batteries. *Adv. Mater.* **1998**, *10* (10), 725-763.
80. Wetjen, M.; Pritzl, D.; Jung, R.; Solchenbach, S.; Ghadimi, R.; Gasteiger, H. A., Differentiating the Degradation Phenomena in Silicon-Graphite Electrodes for Lithium-Ion Batteries. *J Electrochem Soc* **2017**, *164* (12), A2840-A2852.
81. Kim, S. Y.; Lee, J.; Kim, B. H.; Kim, Y. J.; Yang, K. S.; Park, M. S., Facile Synthesis of Carbon-Coated Silicon/Graphite Spherical Composites for High-Performance Lithium-Ion Batteries.

- ACS Applied Materials and Interfaces* **2016**, 8 (19), 12109-12117.
82. Petibon, R.; Chevrier, V. L.; Aiken, C. P.; Hall, D. S.; Hyatt, S. R.; Shunmugasundaram, R.; Dahn, J. R., Studies of the Capacity Fade Mechanisms of LiCoO₂/Si-Alloy: Graphite Cells. *Journal of The Electrochemical Society* **2016**, 163 (7), A1146-A1156.
 83. Yang, J.; Takeda, Y.; Imanishi, N.; Capiglia, C.; Xie, J. Y.; Yamamoto, O., SiO_x-based anodes for secondary lithium batteries. *Solid State Ionics* **2002**, 152-153, 125-129.
 84. Kim, T.; Park, S.; Oh, S. M., Solid-State NMR and Electrochemical Dilatometry Study on Li⁺ Uptake/Extraction Mechanism in SiO Electrode. *Journal of The Electrochemical Society* **2007**, 154 (12), A1112-A1117.
 85. Park, M.-S.; Rajendran, S.; Kang, Y.-M.; Han, K.-S.; Han, Y.-S.; Lee, J.-Y., Si-Ni alloy-graphite composite synthesized by arc-melting and high-energy mechanical milling for use as an anode in lithium-ion batteries. *Journal of Power Sources* **2006**, 158 (1), 650-653.
 86. Jung, H.; Kim, Y.-U.; Sung, M.-S.; Hwa, Y.; Jeong, G.; Kim, G.-B.; Sohn, H.-J., Nanosize Si anode embedded in super-elastic nitinol (Ni-Ti) shape memory alloy matrix for Li rechargeable batteries. *J Mater Chem* **2011**, 21 (30), 11213-11216.
 87. Deng, L.; Wu, Z.-Y.; Yin, Z.-W.; Lu, Y.-Q.; Huang, Z.-G.; You, J.-H.; Li, J.-T.; Huang, L.; Sun, S.-G., High-performance SiMn/C composite anodes with integrating inactive Mn₄Si₇ alloy for lithium-ion batteries. *Electrochim Acta* **2018**, 260, 830-837.
 88. Ladam, A.; Bibent, N.; Cénac-Morthé, C.; Aldon, L.; Olivier-Fourcade, J.; Jumas, J.-C.; Lippens, P.-E., One-pot ball-milling synthesis of a Ni-Ti-Si based composite as anode material for Li-ion batteries. *Electrochim Acta* **2017**, 245, 497-504.
 89. Sohn, M.; Lee, D. G.; Park, H.-I.; Park, C.; Choi, J.-H.; Kim, H., Microstructure Controlled Porous Silicon Particles as a High Capacity Lithium Storage Material via Dual Step Pore Engineering. *Adv. Funct Mater.* **2018**, 28 (23), 1800855.
 90. Al-Maghrabi, M. A.; Suzuki, J.; Sanderson, R. J.; Chevrier, V. L.; Dunlap, R. A.; Dahn, J. R., Combinatorial Studies of Si_{1-x}O_x as a Potential Negative Electrode Material for Li-Ion Battery Applications. *J Electrochem Soc* **2013**, 160 (9), A1587-A1593.
 91. Netz, A.; Huggins, R. A.; Weppner, W., The formation and properties of amorphous silicon as negative electrode reactant in lithium systems. *Journal of Power Sources* **2003**, 119-121, 95-100.
 92. Netz, A.; Huggins, R. A., Amorphous silicon formed in situ as negative electrode reactant in lithium cells. *Solid State Ionics* **2004**, 175 (1), 215-219.
 93. Suh, S. S.; Yoon, W. Y.; Kim, D. H.; Kwon, S. U.; Kim, J. H.; Kim, Y. U.; Jeong, C. U.; Chan, Y. Y.; Kang, S. H.; Lee, J. K., Electrochemical behavior of SiO_x anodes with variation of oxygen ratio for Li-ion batteries. *Electrochimica Acta* **2014**, 148, 111-117.

94. Wang, P.; NuLi, Y.; Yang, J.; Zheng, Y., Carbon-coated Si-Cu/graphite composite as anode material for lithium-ion batteries. *International Journal of Electrochemical Science* **2006**, *1* (3), 122-129.
95. Usui, H.; Meabara, K.; Nakai, K.; Sakaguchi, H., Anode properties of composite thick-film electrodes consisted of Si and various metal silicides. *International Journal of Electrochemical Science* **2011**, *6* (6), 2246-2254.
96. Bang, B. M.; Kim, H.; Song, H. K.; Cho, J.; Park, S., Scalable approach to multi-dimensional bulk Si anodes via metal-assisted chemical etching. *Energy and Environmental Science* **2011**, *4* (12), 5013-5019.
97. Ge, M.; Rong, J.; Fang, X.; Zhang, A.; Lu, Y.; Zhou, C., Scalable preparation of porous silicon nanoparticles and their application for lithium-ion battery anodes. *Nano Res* **2013**, *6* (3), 174-181.
98. Wang, C. S.; Wu, G. T.; Zhang, X. B.; Qi, Z. F.; Li, W. Z., Lithium Insertion in Carbon-Silicon Composite Materials Produced by Mechanical Milling. *Journal of The Electrochemical Society* **1998**, *145* (8), 2751-2758.
99. Takacs, L., Self-sustaining reactions induced by ball milling. *Progress in Materials Science* **2002**, *47* (4), 355-414.
100. Li, X.; Yang, D.; Hou, X.; Shi, J.; Peng, Y.; Yang, H., Scalable preparation of mesoporous Silicon@C/graphite hybrid as stable anodes for lithium-ion batteries. *J Alloy Compd* **2017**, *728*, 1-9.
101. Yoshio, M.; Tsumura, T.; Dimov, N., Silicon/graphite composites as an anode material for lithium ion batteries. *J Power Sources* **2006**, *163* (1), 215-218.
102. Zhang, J.; Liang, Y.; Zhou, Q.; Peng, Y.; Yang, H., Enhancing electrochemical properties of silicon-graphite anodes by the introduction of cobalt for lithium-ion batteries. *J Power Sources* **2015**, *290*, 71-79.
103. Qian, L.; Lan, J.-L.; Xue, M.; Yu, Y.; Yang, X., Two-step ball-milling synthesis of a Si/SiO_x/C composite electrode for lithium ion batteries with excellent long-term cycling stability. *RSC Advances* **2017**, *7* (58), 36697-36704.
104. Huang, S.; Cheong, L.-Z.; Wang, D.; Shen, C., Nanostructured Phosphorus Doped Silicon/Graphite Composite as Anode for High-Performance Lithium-Ion Batteries. *ACS Applied Materials & Interfaces* **2017**, *9* (28), 23672-23678.
105. Sui, D.; Xie, Y.; Zhao, W.; Zhang, H.; Zhou, Y.; Qin, X.; Ma, Y.; Yang, Y.; Chen, Y., A high-performance ternary Si composite anode material with crystal graphite core and amorphous carbon shell. *J Power Sources* **2018**, *384*, 328-333.
106. Wang, H.; Xie, J.; Zhang, S.; Cao, G.; Zhao, X., Scalable preparation of

- silicon@graphite/carbon microspheres as high-performance lithium-ion battery anode materials. *RSC Advances* **2016**, *6* (74), 69882-69888.
107. Wang, J.; Bao, W.; Ma, L.; Tan, G.; Su, Y.; Chen, S.; Wu, F.; Lu, J.; Amine, K., Scalable Preparation of Ternary Hierarchical Silicon Oxide–Nickel–Graphite Composites for Lithium-Ion Batteries. *ChemSusChem* **2015**, *8* (23), 4073-4080.
 108. Cetinkaya, T.; Cevher, O.; Tocoglu, U.; Guler, M. O.; Akbulut, H., Electrochemical characterization of the powder silicon anodes reinforced with graphite using planetary ball milling. *Acta Physica Polonica A* **2013**, *123* (2), 393-395.
 109. Yoon, Y. S.; Jee, S. H.; Lee, S. H.; Nam, S. C., Nano Si-coated graphite composite anode synthesized by semi-mass production ball milling for lithium secondary batteries. *Surface and Coatings Technology* **2011**, *206* (2), 553-558.
 110. Chen, Y.; Qian, J.; Cao, Y.; Yang, H.; Ai, X., Green Synthesis and Stable Li-Storage Performance of FeSi₂/Si@C Nanocomposite for Lithium-Ion Batteries. *ACS Appl. Mater. Interfaces* **2012**, *4* (7), 3753-3758.
 111. Zhang, Y.; Zhang, X. G.; Zhang, H. L.; Zhao, Z. G.; Li, F.; Liu, C.; Cheng, H. M., Composite anode material of silicon/graphite/carbon nanotubes for Li-ion batteries. *Electrochimica Acta* **2006**, *51* (23), 4994-5000.
 112. Ren, Y.; Ding, J.; Yuan, N.; Jia, S.; Qu, M.; Yu, Z., Preparation and characterization of silicon monoxide/graphite/carbon nanotubes composite as anode for lithium-ion batteries. *J Solid State Electr* **2012**, *16* (4), 1453-1460.
 113. Yang, X.; Wen, Z.; Xu, X.; Lin, B.; Lin, Z., High-Performance Silicon/Carbon/Graphite Composites as Anode Materials for Lithium Ion Batteries. *J Electrochem Soc* **2006**, *153* (7), A1341-A1344.
 114. Lee, J.-H.; Kim, W.-J.; Kim, J.-Y.; Lim, S.-H.; Lee, S.-M., Spherical silicon/graphite/carbon composites as anode material for lithium-ion batteries. *Journal of Power Sources* **2008**, *176* (1), 353-358.
 115. Jo, Y. N.; Kim, Y.; Kim, J. S.; Song, J. H.; Kim, K. J.; Kwag, C. Y.; Lee, D. J.; Park, C. W.; Kim, Y. J., Si–graphite composites as anode materials for lithium secondary batteries. *Journal of Power Sources* **2010**, *195* (18), 6031-6036.
 116. Kuksenko, S. P.; Kovalenko, I. O., Synthesis of a silicon-graphite composite for the hybrid electrode of lithium-ion batteries. *Russian Journal of Applied Chemistry* **2010**, *83* (10), 1811-1815.
 117. Liu, H. M.; Jiang, X. Y., Electrochemical lithium storage performance of Si/C based anode materials prepared by mechanical alloying. *Materials Research Innovations* **2014**, *18* (sup4), S4-10-S4-14.

118. Li, X.; Zhang, G.; Zhang, L.; Zhong, M.; Yuan, X., Silicon/graphite/carbon nanotubes composite as anode for lithium ion battery. *Int J Electrochem Sc* **2015**, *10* (4), 2802-2811.
119. Liu, W.; Zhong, Y.; Yang, S.; Zhang, S.; Yu, X.; Wang, H.; Li, Q.; Li, J.; Cai, X.; Fang, Y., Electro spray synthesis of nano-Si encapsulated in graphite/carbon microplates as robust anodes for high performance lithium-ion batteries. *Sustainable Energy & Fuels* **2018**, *2* (3), 679-687.
120. Yen, J.-P.; Chang, C.-C.; Lin, Y.-R.; Shen, S.-T.; Hong, J.-L., Sputtered copper coating on silicon/graphite composite anode for lithium ion batteries. *J Alloy Compd* **2014**, *598*, 184-190.
121. Yom, J. H.; Lee, J. K.; Yoon, W. Y., Improved electrochemical behavior of W-coated SiO-graphite composite anode in lithium-ion secondary battery. *J Appl Electrochem* **2015**, *45* (5), 397-403.
122. Rattes, A. L. R.; Oliveira, W. P., Spray drying conditions and encapsulating composition effects on formation and properties of sodium diclofenac microparticles. *Powder Technol* **2007**, *171* (1), 7-14.
123. Sosnik, A.; Seremeta, K. P., Advantages and challenges of the spray-drying technology for the production of pure drug particles and drug-loaded polymeric carriers. *Advances in Colloid and Interface Science* **2015**, *223*, 40-54.
124. Cheow, W. S.; Li, S.; Hadinoto, K., Spray drying formulation of hollow spherical aggregates of silica nanoparticles by experimental design. *Chemical Engineering Research and Design* **2010**, *88* (5-6), 673-685.
125. NiÓgáin, O.; Tajber, L.; Corrigan, O. I.; Healy, A. M., Spray drying from organic solvents to prepare nanoporous/nanoparticulate microparticles of protein: Excipient composites designed for oral inhalation. *Journal of Pharmacy and Pharmacology* **2012**, *64* (9), 1275-1290.
126. Jung, D. S.; Hwang, T. H.; Park, S. B.; Choi, J. W., Spray Drying Method for Large-Scale and High-Performance Silicon Negative Electrodes in Li-Ion Batteries. *Nano Letters* **2013**, *13* (5), 2092-2097.
127. Carné-Sánchez, A.; Imaz, I.; Cano-Sarabia, M.; Maspoch, D., A spray-drying strategy for synthesis of nanoscale metal-organic frameworks and their assembly into hollow superstructures. *Nat Chem* **2013**, *5*, 203.
128. Su, M.; Wang, Z.; Guo, H.; Li, X.; Huang, S.; Xiao, W.; Gan, L., Enhancement of the Cyclability of a Si/Graphite@Graphene composite as anode for Lithium-ion batteries. *Electrochimica Acta* **2014**, *116*, 230-236.
129. Yang, Y.; Wang, Z.; Zhou, Y.; Guo, H.; Li, X., Synthesis of porous Si/graphite/carbon nanotubes@C composites as a practical high-capacity anode for lithium-ion batteries. *Mater Lett* **2017**, *199*, 84-87.

130. Wang, A.; Liu, F.; Wang, Z.; Liu, X., Self-assembly of silicon/carbon hybrids and natural graphite as anode materials for lithium-ion batteries. *RSC Advances* **2016**, *6* (107), 104995-105002.
131. Wang, Z.; Mao, Z.; Lai, L.; Okubo, M.; Song, Y.; Zhou, Y.; Liu, X.; Huang, W., Sub-micron silicon/pyrolyzed carbon@natural graphite self-assembly composite anode material for lithium-ion batteries. *Chemical Engineering Journal* **2017**, *313*, 187-196.
132. Gan, L.; Guo, H.; Wang, Z.; Li, X.; Peng, W.; Wang, J.; Huang, S.; Su, M., A facile synthesis of graphite/silicon/graphene spherical composite anode for lithium-ion batteries. *Electrochim Acta* **2013**, *104*, 117-123.
133. Li, M.; Hou, X.; Sha, Y.; Wang, J.; Hu, S.; Liu, X.; Shao, Z., Facile spray-drying/pyrolysis synthesis of core-shell structure graphite/silicon-porous carbon composite as a superior anode for Li-ion batteries. *J Power Sources* **2014**, *248*, 721-728.
134. Kong, J.; Yee, W. A.; Yang, L.; Wei, Y.; Phua, S. L.; Ong, H. G.; Ang, J. M.; Li, X.; Lu, X., Highly electrically conductive layered carbon derived from polydopamine and its functions in SnO₂-based lithium ion battery anodes. *Chem. Commun.* **2012**, *48* (83), 10316-10318.
135. Lee, H.; Dellatore, S. M.; Miller, W. M.; Messersmith, P. B., Mussel-Inspired Surface Chemistry for Multifunctional Coatings. *Science* **2007**, *318* (5849), 426-430.
136. Kang, S. M.; Hwang, N. S.; Yeom, J.; Park, S. Y.; Messersmith, P. B.; Choi, I. S.; Langer, R.; Anderson, D. G.; Lee, H., One-Step Multipurpose Surface Functionalization by Adhesive Catecholamine. *Adv. Funct Mater.* **2012**, *22* (14), 2949-2955.
137. Zhou, R.; Guo, H.; Yang, Y.; Wang, Z.; Li, X.; Zhou, Y., N-doped carbon layer derived from polydopamine to improve the electrochemical performance of spray-dried Si/graphite composite anode material for lithium ion batteries. *J Alloy Compd* **2016**, *689*, 130-137.
138. Wu, J.; Tu, W.; Zhang, Y.; Guo, B.; Li, S.; Zhang, Y.; Wang, Y.; Pan, M., Poly-dopamine coated graphite oxide/silicon composite as anode of lithium ion batteries. *Powder Technol* **2017**, *311*, 200-205.
139. Chen, H.; Hou, X.; Chen, F.; Wang, S.; Wu, B.; Ru, Q.; Qin, H.; Xia, Y., Milled flake graphite/plasma nano-silicon@carbon composite with void sandwich structure for high performance as lithium ion battery anode at high temperature. *Carbon* **2018**, *130*, 433-440.
140. Lai, J.; Guo, H.; Wang, Z.; Li, X.; Zhang, X.; Wu, F.; Yue, P., Preparation and characterization of flake graphite/silicon/carbon spherical composite as anode materials for lithium-ion batteries. *J Alloy Compd* **2012**, *530*, 30-35.
141. Li, J.; Wang, J.; Yang, J.; Ma, X.; Lu, S., Scalable synthesis of a novel structured graphite/silicon/pyrolyzed-carbon composite as anode material for high-performance lithium-ion batteries. *J Alloy Compd* **2016**, *688*, 1072-1079.

142. Choy, K. L., Chemical vapour deposition of coatings. *Progress in Materials Science* **2003**, *48* (2), 57-170.
143. Xie, J.; Cao, G. S.; Zhao, X. B., Electrochemical performances of Si-coated MCMB as anode material in lithium-ion cells. *Materials Chemistry and Physics* **2004**, *88* (2), 295-299.
144. Kim, I.-C.; Byun, D.; Lee, S.; Lee, J. K., Electrochemical characteristics of copper silicide-coated graphite as an anode material of lithium secondary batteries. *Electrochim Acta* **2006**, *52* (4), 1532-1537.
145. Kim, I.-C.; Byun, D.; Lee, J. K., Electrochemical characteristics of silicon-metals coated graphites for anode materials of lithium secondary batteries. *Journal of Electroceramics* **2006**, *17* (2), 661-665.
146. Kim, C.; Ko, M.; Yoo, S.; Chae, S.; Choi, S.; Lee, E.-H.; Ko, S.; Lee, S.-Y.; Cho, J.; Park, S., Novel design of ultra-fast Si anodes for Li-ion batteries: crystalline Si@amorphous Si encapsulating hard carbon. *Nanoscale* **2014**, *6* (18), 10604-10610.
147. Jeong, S.; Lee, J. P.; Ko, M.; Kim, G.; Park, S.; Cho, J., Etched graphite with internally grown Si nanowires from pores as an anode for high density Li-ion batteries. *Nano Letters* **2013**, *13* (7), 3403-3407.
148. Lu, M.; Tian, Y.; Zheng, X.; Gao, G.; Huang, B., Preparation, characterization and electrochemical performance of silicon coated natural graphite as anode for lithium ion batteries. *Int J Electrochem Sc* **2012**, *7* (7), 6180-6190.
149. Su, M.; Wang, Z.; Guo, H.; Li, X.; Huang, S.; Gan, L., Silicon, flake graphite and phenolic resin-pyrolyzed carbon based Si/C composites as anode material for lithium-ion batteries. *Advanced Powder Technology* **2013**, *24* (6), 921-925.
150. Jeong, S.; Li, X.; Zheng, J.; Yan, P.; Cao, R.; Jung, H. J.; Wang, C.; Liu, J.; Zhang, J.-G., Hard carbon coated nano-Si/graphite composite as a high performance anode for Li-ion batteries. *Journal of Power Sources* **2016**, *329*, 323-329.
151. Uono, H.; Kim, B.-C.; Fuse, T.; Ue, M.; Yamaki, J.-i., Optimized Structure of Silicon/Carbon/Graphite Composites as an Anode Material for Li-Ion Batteries. *Journal of The Electrochemical Society* **2006**, *153* (9), A1708-A1713.
152. Wang, Y.-X.; Chou, S.-L.; Kim, J. H.; Liu, H.-K.; Dou, S.-X., Nanocomposites of silicon and carbon derived from coal tar pitch: Cheap anode materials for lithium-ion batteries with long cycle life and enhanced capacity. *Electrochim Acta* **2013**, *93*, 213-221.
153. Yang, Y.; Wang, Z.; Yan, G.; Guo, H.; Wang, J.; Li, X.; Zhou, Y.; Zhou, R., *Pitch carbon and LiF co-modified Si-based anode material for lithium ion batteries*. 2017.
154. Xiao, C.; He, P.; Ren, J.; Yue, M.; Huang, Y.; He, X., Walnut-structure Si-G/C materials with high coulombic efficiency for long-life lithium ion batteries. *RSC Advances* **2018**, *8* (48),

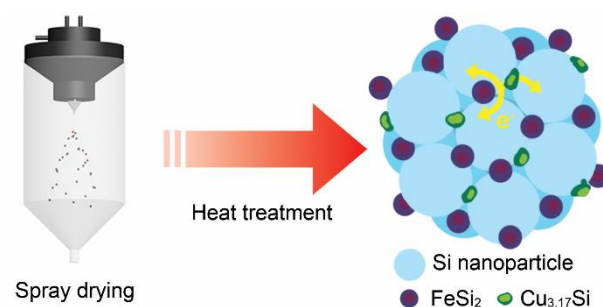
27580-27586.

155. Kenji, F.; Kazuhiko, K.; Kennichi, I.; Masaki, Y., Foliated natural graphite as the anode material for rechargeable lithium-ion cells. *J Power Sources* **1997**, *69* (1), 165-168.
156. Yoshio, M.; Wang, H. Y.; Fukuda, K.; Umeno, T.; Abe, T.; Ogumi, Z., Improvement of natural graphite as a lithium-ion battery anode material, from raw flake to carbon-coated sphere. *J Mater Chem* **2004**, *14* (11), 1754-1758.
157. Yoshio, M.; Wang, H.; Fukuda, K., Spherical carbon-coated natural graphite as a lithium-ion battery-anode material. *Angew Chem Int Ed Engl* **2003**, *42* (35), 4203-6.
158. Han, Y.-J.; Kim, J.; Yeo, J.-S.; An, J. C.; Hong, I.-P.; Nakabayashi, K.; Miyawaki, J.; Jung, J.-D.; Yoon, S.-H., Coating of graphite anode with coal tar pitch as an effective precursor for enhancing the rate performance in Li-ion batteries: Effects of composition and softening points of coal tar pitch. *Carbon* **2015**, *94*, 432-438.
159. Zhou, Y.-y.; Li, X.-h.; Guo, H.-j.; Wang, Z.-x.; Yang, Y.; Xie, Q.-l., Modification of natural graphite using pitch through dynamical melt-carbonization. *Journal of Central South University of Technology* **2007**, *14* (5), 651-655.
160. Nakajima, T.; Shibata, S.; Naga, K.; Ohzawa, Y.; Tressaud, A.; Durand, E.; Groult, H.; Warmont, F., Surface structure and electrochemical characteristics of plasma-fluorinated petroleum cokes for lithium ion battery. *J Power Sources* **2007**, *168* (1), 265-271.
161. Wallouch, R. W.; Murty, H. N.; Heintz, E. A., Pyrolysis of coal tar pitch binders. *Carbon* **1972**, *10* (6), 729-735.
162. Zhecheva, E.; Stoyanova, R.; Jiménez-Mateos, J. M.; Alcántara, R.; Lavela, P.; Tirado, J. L., EPR study on petroleum cokes annealed at different temperatures and used in lithium and sodium batteries. *Carbon* **2002**, *40* (13), 2301-2306.
163. Zaghbi, K.; Brochu, F.; Guerfi, A.; Kinoshita, K., Effect of particle size on lithium intercalation rates in natural graphite. *J Power Sources* **2001**, *103* (1), 140-146.
164. Sivakkumar, S. R.; Nerkar, J. Y.; Pandolfo, A. G., Rate capability of graphite materials as negative electrodes in lithium-ion capacitors. *Electrochim Acta* **2010**, *55* (9), 3330-3335.
165. Wolfenstine, J., Critical grain size for microcracking during lithium insertion. *J Power Sources* **1999**, *79* (1), 111-113.
166. Yang, J.; Winter, M.; Besenhard, J. O., Small particle size multiphase Li-alloy anodes for lithium-ion batteries. *Solid State Ionics* **1996**, *90* (1), 281-287.
167. McDowell, M. T.; Lee, S. W.; Harris, J. T.; Korgel, B. A.; Wang, C.; Nix, W. D.; Cui, Y., In situ TEM of two-phase lithiation of amorphous silicon nanospheres. *Nano Lett* **2013**, *13* (2), 758-64.
168. Kim, H.; Seo, M.; Park, M. H.; Cho, J., A Critical Size of Silicon Nano-Anodes for Lithium

- Rechargeable Batteries. *Angewandte Chemie, International Edition* **2010**, *49* (12), 2146-2149.
169. Gao, H.; Xiao, L.; Plümel, I.; Xu, G.-L.; Ren, Y.; Zuo, X.; Liu, Y.; Schulz, C.; Wiggers, H.; Amine, K.; Chen, Z., Parasitic Reactions in Nanosized Silicon Anodes for Lithium-Ion Batteries. *Nano Letters* **2017**, *17* (3), 1512-1519.
170. Ge, M. Y.; Lu, Y. H.; Ercius, P.; Rong, J. P.; Fang, X.; Mecklenburg, M.; Zhou, C. W., Large-Scale Fabrication, 3D Tomography, and Lithium-Ion Battery Application of Porous Silicon. *Nano Letters* **2014**, *14* (1), 261-268.
171. Zhu, B.; Jin, Y.; Tan, Y.; Zong, L.; Hu, Y.; Chen, L.; Chen, Y.; Zhang, Q.; Zhu, J., Scalable Production of Si Nanoparticles Directly from Low Grade Sources for Lithium-Ion Battery Anode. *Nano Letters* **2015**, *15* (9), 5750-5754.
172. Jin, Y.; Zhang, S.; Zhu, B.; Tan, Y.; Hu, X.; Zong, L.; Zhu, J., Simultaneous Purification and Perforation of Low-Grade Si Sources for Lithium-Ion Battery Anode. *Nano Letters* **2015**, *15* (11), 7742-7747.
173. Liu, N.; Wu, H.; McDowell, M. T.; Yao, Y.; Wang, C. M.; Cui, Y., A Yolk-Shell Design for Stabilized and Scalable Li-Ion Battery Alloy Anodes. *Nano Letters* **2012**, *12* (6), 3315-3321.
174. Luo, F.; Liu, B. N.; Zheng, J. Y.; Chu, G.; Zhong, K. F.; Li, H.; Huang, X. J.; Chen, L. Q., Review-Nano-Silicon/Carbon Composite Anode Materials Towards Practical Application for Next Generation Li-Ion Batteries. *J Electrochem Soc* **2015**, *162* (14), A2509-A2528.

Chapter 2

Micron-Sized Fe-Cu-Si Ternary Composite Anodes for High Energy Li-ion Batteries



Nano-engineering of silicon anodes has contributed to demonstrating a promising potential for high energy lithium ion batteries through addressing degradation of battery performances derived from severe volume changes during cycling. However, practical use of nano-engineered silicon anodes still has been stuck because of remaining challenges, such as low tap density, poor scalability and inferior electrical properties. Herein, we successfully developed new Fe-Cu-Si ternary composite (FeCuSi) by scalable spray drying and facile heat treatment. As a result, FeCuSi exhibited remarkable initial Coulombic efficiency (91%) and specific capacity (1287 mAh/g). In order to exactly characterize electrical properties of FeCuSi and directly compare them with industrially developed benchmarking samples, such as silicon monoxide (SiO) and silicon-metal alloy (Si₂Fe), both of half-cell and full-cell test were performed with high electrode density (1.6 g/cc) and high areal capacity (3.4 mAh/cm²). Overall, FeCuSi showed outperformed discharge capacity and capacity retention in high mass loading for 300 cycles over benchmarking samples.

This chapter has been published.

Reproduced with permission from Chae, S.; Ko, M.; Park, S.; Kim, N.; Ma, J.; Cho, J., Micron-sized Fe–Cu–Si ternary composite anodes for high energy Li-ion batteries. *Energ Environ Sci* **2016**, 9 (4), 1251-1257.

2.1 Introduction

To meet urged energy demands for practical applications in portable electronics and electric vehicles, developing electrode materials with high energy density for lithium ion batteries (LIBs) has become a significant research topic.¹⁻³ On this account, silicon (Si) has been well known for the most promising alternative material as a next-generation LIB anode⁴⁻⁶ owing to its high gravimetric capacity (3579 mAh/g),^{7, 8} low average voltage (~ 370 mV vs Li/Li⁺)^{4, 9, 10} and its rational production cost.^{10, 11} However, its electrochemical performances are drastically deteriorated from electrical isolation and continuous formation of unstable solid electrolyte interphase (SEI) caused by severe volume changes ($\sim 400\%$)^{12, 13} during repeated lithium (de)alloying processes.^{14, 15} At this point, extensive efforts have succeeded in accommodating volume change through various nano-engineering of Si anodes.^{14, 16, 17} However, several challenges of Si nanostructures, such as low tap density, high surface area, and poor electrical properties, have still remained as a practical limitation of LIB applications.^{15, 18, 19}

In terms of the industrial approach for improving an energy density of LIBs, Si-graphite blending has been emerged as a practicable method instead of whole utilization of Si-based anodes.^{20, 21} Graphite plays a role of improving initial Coulombic efficiency (CE) and maintaining good cycling performance even with small amounts of binding materials ($\sim 3\%$), high electrode density (~ 1.6 g/cc), and high areal capacity (≥ 3 mAh/cm²). With graphite blending, incorporation of Si and inactive matrix, such as silicon monoxide (SiO_x)²²⁻²⁵ and Si-metal alloys²⁶⁻³⁰, has been attempted vigorously as up-to-date commercialization anode materials. SiO_x has typically 1300-1500 mAh/g of reversible capacity with about 50% of poor initial CE.²²⁻²⁵ On the other hand, Si-metal alloys, which were synthesized through melt spinning or high-energy mechanical milling process (HEMM), have various reversible capacities (800-1200 mAh/g) and initial CE (80-93%) depending on the kind and proportion of counter metals, such as Al, Ti, Fe, Ni and etc.²⁶⁻³⁰ Both of SiO_x and Si-metal alloys have a common strategy for reducing volume expansion of the electrode via diluting active phases (Si) with inactive phase (Li₄SiO₄³¹ and metal silicides³²⁻³⁴), resulting in enhancement of electrode stability. However, in spite of graphite blending and their strategies of inactive matrix for addressing the challenges of Si, those are still incompetent materials for alternatives of graphite, because SiO_x has large irreversible capacity loss with low initial CE and Si-metal alloys haven't yet demonstrate stable cycling behaviours in full-cell system, in contrast to showing great cycling performances in a half-cell test. Therefore, it is an important task for battery researchers to develop commercially viable Si-based anodes which have superior battery performances than those of benchmarking samples.

2.2 Experimental Detail

Preparation of FeCuSi: The amorphous Si nanoparticles were prepared through decomposition of monosilane (SiH₄) gas at 400 °C. As a first step, 3.5 g of amorphous Si nanoparticles were well dispersed in 0.6 L of distilled water. Then, 7 g of iron nitrate nonahydrate (Fe(NO₃)₃·9H₂O, Aldrich) and 2 g of copper nitrate trihydrate (Cu(NO₃)₂·3H₂O, Aldrich) were added. Under stirring, the mixed solution was then atomized and dried through spray dryer (Mini Spray Dryer B-290, BUCHI Labortechnik) at 200 °C of inlet temperature. Afterwards, spray dried particles were simply heated in a tube furnace at various temperatures and 1 hour of duration time under hydrogen atmosphere.

Material characterization: FeCuSi was investigated with scanning electron microscopy (SEM, Verios 460, FEI), focused ion beam (FIB, Quanta 3D FEG), and X-ray diffraction (XRD, D/MAZX 2500V/PC, Rigaku). In addition, high resolution transmission electron microscopy (HR-TEM, JEM-2100F, JEOL) was utilized for detailed characterization, where sample preparation was carried out using dual-beam focused ion beam (FIB, Helios 450HP, FEI). Statistical analysis for size distribution of FeCuSi was performed with laser diffraction particle size analysis instrument (Microtrac S3500, Microtrac). Tap density was measured by density analyser (GeoPyc 1360, micromeritics) with 1 g of each sample. Specific surface area and pore size distribution were analysed through BET and BJH methods, respectively, with surface area and porosity analyzer (TriStar II, micromeritics). The change of electrode thickness at the lithiation state were measured with micrometer after disassembling coin cells in Ar-filled glove box. The change was estimated with the equation:

$$\frac{(\text{Electrode thickness at } N^{\text{th}} \text{ cycle} - \text{Electrode thickness at } 1^{\text{st}} \text{ cycle})}{\text{Electrode thickness at } 1^{\text{st}} \text{ cycle}} \times 100(\%)$$

Electrochemical characterization

1) Anode materials in half-cell: The electrode was fabricated with active material (FeCuSi, C-SiO_x, and FeSi₂, respectively), carbon black (Super P, TIMCAL), carboxymethyl cellulose (CMC), and styrene butadiene rubber (SBR) with the mass ratio of 80:10:5:5. The homogeneously blended slurry was coated on copper foil with ~1mg/cm² of loading level, dried at 80 °C for 30 minutes, and then went through vacuum drying at 110 °C for 2 hours without calendaring. The electrochemical properties were measured at 25 °C with 2032R coin-type using metallic Li foil as a counter electrode. All the cells were assembled in Argon-filled glove box. Microporous polyethylene, and 1.3 M LiPF₆ in ethylene carbonate (EC)/ethyl methyl carbonate (EMC)/ diethyl carbonate (DEC) (=3/5/2, v/v/v) with 10% fluoroethylene carbonate (FEC) and 0.5% vinylene carbonate (VC) (Panax Starlyte) were used as separator and electrolyte, respectively.

The half-cells were run with constant current (CC) – constant voltage (CV) mode between 0.005 and 1.5 V for the formation cycle and between 0.005 and 1 V for the cycling test with TOSCAT-3100 battery cycler (TOYO SYSTEM). The rate was 0.1C for the formation cycle and 0.5C for the cycling test, while constant voltage was at 0.005V with 13 mA/g, 11 mA/g and 17 mA/g cut off for FeCuSi, C-SiO_x, and FeSi₂, respectively. (1C was set as 1.3 A/g, 1.1 A/g and 1.7 A/g for FeCuSi, C-SiO_x, and FeSi₂, respectively.)

2) Graphite-blended anodes in half-cell: FeCuSi, C-SiO_x, and FeSi₂ were blended with natural graphite (BTR) to obtain 420 mAh/g of specific capacity with 7wt%, 5wt%, and 9wt%, respectively. The electrode was fabricated with active materials composed of Si-based materials and graphite, CMC and SBR with the mass ratio of 97:1.5:1.5 as minimized contents of binding materials. The homogeneously blended slurry was coated on copper foil with 8.5 mg/cm² of loading level which corresponds to 3.44~3.48 mAh/cm², dried at 80 °C for 30 minutes, and then went through vacuum drying at 110 °C for 2 hours with calendaring in order to increase the electrode density up to 1.6 g/cc. The electrochemical properties were measured at 25 °C with 2032R coin-type using Li foil as a counter electrode. The cell assembly and other battery components except anodes were the same with those in above electrochemical characterization.

The half-cells were run with CC-CV mode between 0.005 and 1.5 V for the formation cycle and between 0.005 to 1 V for the cycling test with TOSCAT-3100 battery cycler (TOYO SYSTEM). The rate was 0.1C for the formation cycle and 0.5C for the cycling test, while constant voltage was at 0.005V with 4.2 mA/g cut off. (1C was set as 0.42 A/g for all half-cells).

3) LiCoO₂ in half-cell: The electrode was fabricated with LiCoO₂, carbon black (Super P, TIMCAL), and polyvinylidene fluoride (PVDF) with the mass ratio of 94:3:3. The homogeneously blended slurry was coated on aluminium foil with 20.4 mg/cm² of loading level which corresponds to ~3.42 mAh/cm², dried at 110 °C for 1 hour. Afterwards, the electrode was calendared in order to increase the electrode density up to 3.6 g/cc. The electrochemical properties were measured at 25 °C with 2032R coin-type using Li foil as a counter electrode. All the cells were assembled in Argon-filled glove box. Separator and electrolytes were the same with those of anodes in half-cell.

The half-cells were run with CC-CV mode between 3.0 and 4.45 V with TOSCAT-3100 battery cycler (TOYO SYSTEM). The rate was 0.1C for the formation cycle and 0.5C for the cycling test, while constant voltage was at 4.45 V with 3.6 mA/g cut off. (1C was set as 0.18 A/g.)

4) Full-cells with graphite-blended anodes and LiCoO₂: The electrodes of graphite-blended anodes and LiCoO₂ for half-cell test were identically utilized for full-cell system. The N.P ratio was estimated as 1.11 to 1.14. The electrochemical properties were measured at 25 °C with 2032R coin-type.

All the cells were assembled in Argon-filled glove box. Separator and electrolytes were the same with those of others.

The full-cells were run with CC-CV mode between 2.5 to 4.35 V with TOSCAT-3100 battery cycler (TOYO SYSTEM). The rate was 0.1C for the formation cycle with constant voltage at 4.35V and 0.03mA/cm² cut off. In the cycling test, 0.5C and 1C were set as charging and discharging rate, respectively, while constant voltage was at 4.35 V with 0.06 mA/cm² cut off. (1C was set as 3.0 mA/cm².)

The schematic (Fig. 1b) illustrates fabrication procedure of FeCuSi. The amorphous Si nanoparticles prepared by chemical vapor deposition (CVD) process using monosilane at ~400 °C were homogeneously dispersed in distilled water by ultrasonicator. After the dispersion, iron nitrate nonahydrate (Fe(NO₃)₃·9H₂O) and copper nitrate trihydrate (Cu(NO₃)₂·3H₂O) were added to the solution as metal precursors. Afterwards, the solution was atomized into microdroplets and dried at 200 °C of inlet temperature through spray dryer. As the droplets evaporated in the spray dryer, the amorphous Si nanoparticles built up spherical type of secondary structure with rational void space. Simultaneously, increased precursor concentration at surface of Si secondary structure leads nano-sized iron nitrate (Fe(NO₃)₃) and copper nitrate (Cu(NO₃)₂) to be crystallized. Because the concentration and the ratio of the amorphous Si nanoparticle and metal precursors determine drying degree, morphology of secondary structure and the amount of metal silicides, we elaborately optimized the concentration of the precursors as 1.10 wt%, 0.33 wt%, and 0.57 wt% of Fe(NO₃)₃·9H₂O, Cu(NO₃)₂·3H₂O, and amorphous Si nanoparticles, respectively. As a result, we successfully obtained the secondary structure with fully dried metal nitrides which were properly adhered in the Si secondary structure.

As a following step, the Si secondary particles, where nano-sized metal nitrates were embedded, were simply heated in hydrogen atmosphere to conduct metal nitrides reduction and metal silicides formation. The reduction from Fe(NO₃)₃ and Cu(NO₃)₂ to Fe and Cu began in earnest after 200 °C, which was accelerated with raising heating temperature and heating time.⁴⁴ As the temperature increased, amorphous Si became crystallized and the reduced metals reacted with Si gradually, leading to formation of iron silicides (FeSi₂) and copper silicides (Cu_{3.17}Si). It is noted that the heat treatment condition including time and temperature affects the phase transformation of the secondary structure, which is strongly related with electrochemical properties. We finally optimized the heating temperature at 860 °C.

2.3 Result and discussion

In order to develop the advanced Si material, herein, we present a unique Si secondary structure, Fe-Cu-Si ternary composite (FeCuSi, **Fig. 2. 1a**), through spray drying and heat treatment. Previously, secondary structures composed of nano-sized Si and carbon have been suggested and demonstrated to decrease surface area and to improve tap density and electrical properties.^{18, 19, 35-37} However, previous Si/C secondary structures had a difficulty in achieving high initial CE because the amorphous carbon in secondary structures induced the irreversible capacity losses according to large amounts of trapped lithium ions. In this work, porous Si secondary structures were built up with lithium-inactive metal silicides and Si nanoparticles which were synthesized from monosilane decomposition method from modified CVD process. This distinguished material design brings about multiple fascinating merits. First of all, formation of lithium-inactive metal silicides, such as iron silicide and copper silicide can be easily controlled via simple heat treatment. As a result of decreased amounts of pure Si in the composite, specific capacity can be properly controlled and electrode stability can be improved via decrease of volume change during cycling. Furthermore, metal silicides offer better electrical conductivity,^{38, 39} leading to high CE. Secondly, the crystalline Si nanoparticles from the amorphous are expected to not only prevent fracture, owing to its size under the critical fracture size, but also give better electrochemical properties than industrial crystalline Si nanoparticles.^{12, 40-42} Thirdly, Si secondary structure accompanies several advantages in common with the previous secondary structure approaches, especially addressing the challenges of nanostructures and alleviating volume change of Si electrode during cycling.^{18, 19, 35, 36} Finally, all the fabrication processes including spray drying and simple heat treatment are, moreover, scalable and facile, which are advantageous to cost-effective mass production for commercialization.^{35, 43}

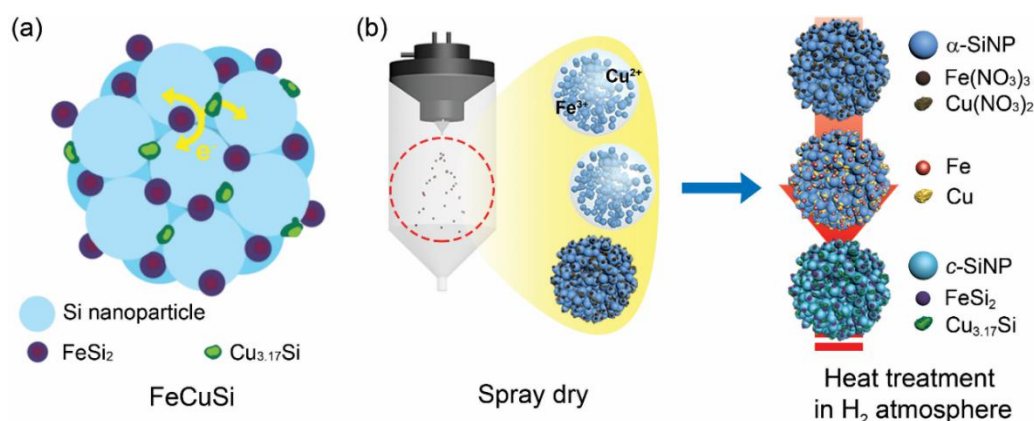


Figure. 2. 1. Schematic illustrations of FeCuSi and its synthesis. (a) Simplified two-dimensional cross-section view of FeCuSi. Silicon nanoparticles build up the secondary particle with metal silicides which can improve electrical conductivity and structural stability. (b) Fabrication process of FeCuSi.

For a detailed material characterization of FeCuSi, we carried out scanning electron microscopy (SEM) with focused ion beam (FIB), the analysis for the size distribution and tap density, Brunauer-Emmett-Teller (BET) analysis, Barrett-Joyner-Halenda (BJH) analysis and X-ray diffraction (XRD) analysis (**Fig. 2. 2**). As shown in SEM images in top and cross sectional views (**Fig. 2. 2a and b**), the shape of FeCuSi is spherical secondary structure which is composed of Si primary particles, where metal silicides are adhered, and void space. Owing to the benefits of nano-size of Si, which is less than 150 nm (**Fig. 2. 3**), lithium-inactive metal silicides and proper void in the structure, FeCuSi can relieve the volume expansion of the composite electrode effectively within its inner void space. The size of FeCuSi varies from 3.0 μm to 18.5 μm with average diameter (D_{50}) of 6.5 μm (**Fig. 2. 2c**). Besides, the tap density (**Fig. 2. 2d**) also measured 0.8 g/cm^3 which is much higher than that of commercially available Si nanoparticles with 0.3 g/cm^3 . The size and high tap density of FeCuSi are expected to be more favorable to conventional electrode fabrication than nanomaterials owing to homogeneous slurry mixing⁴⁵ and increase of volumetric energy density.^{18, 19} With BET and BJH analysis, we got the pore size distribution (**Fig. 2. 4**) and specific surface area as 15.02 m^2/g . XRD pattern (**Fig. 2. 2e**) shows the phase transformation of FeCuSi with raising heating temperature. **Table 2. 1** shows the peak list of Fe, Cu, Si, FeSi₂, and Cu_{3.17}Si in XRD pattern. The samples for the analysis were prepared by heat treatments with 1 hour of duration time and different heating temperatures from 200 °C to 900 °C. Based on the analysis, the intensities of the peaks pointing to Fe and Cu got increased gradually with raising heating temperature from 200 °C, which clearly indicates that the reduction of Fe(NO₃)₃ and Cu(NO₃)₂ proceeded gradually as temperature increases. In addition, the peaks of Fe and Cu considerably diminished and the peaks of Cu_{3.17}Si and FeSi₂ were obviously observed after 800 °C. These metal silicides, which are inactive to lithium,⁵ not only make volume change of the composite controllable through decreasing the amount of lithium-active phase but also supply electrical conducting channels^{38, 39} between Si nanoparticles. Furthermore, with alloy reaction between silicon and metals, metal silicides reinforced the secondary structure by sticking to the junctions between Si nanoparticles. In addition, we can also observe the structural change of Si from amorphous to crystalline phase. From the Halder-wagner method, we can calculate the crystallite size of Si as a function of temperature (**Fig. 2. 5**). The optimized FeCuSi which was treated at 860 °C had 30.5 nm of crystallite size. Compared to FeCuSi at 900 °C, the optimized one can be regarded as more effective on mitigating the localization of stress in its structure when electrochemically (de)alloying with lithium.

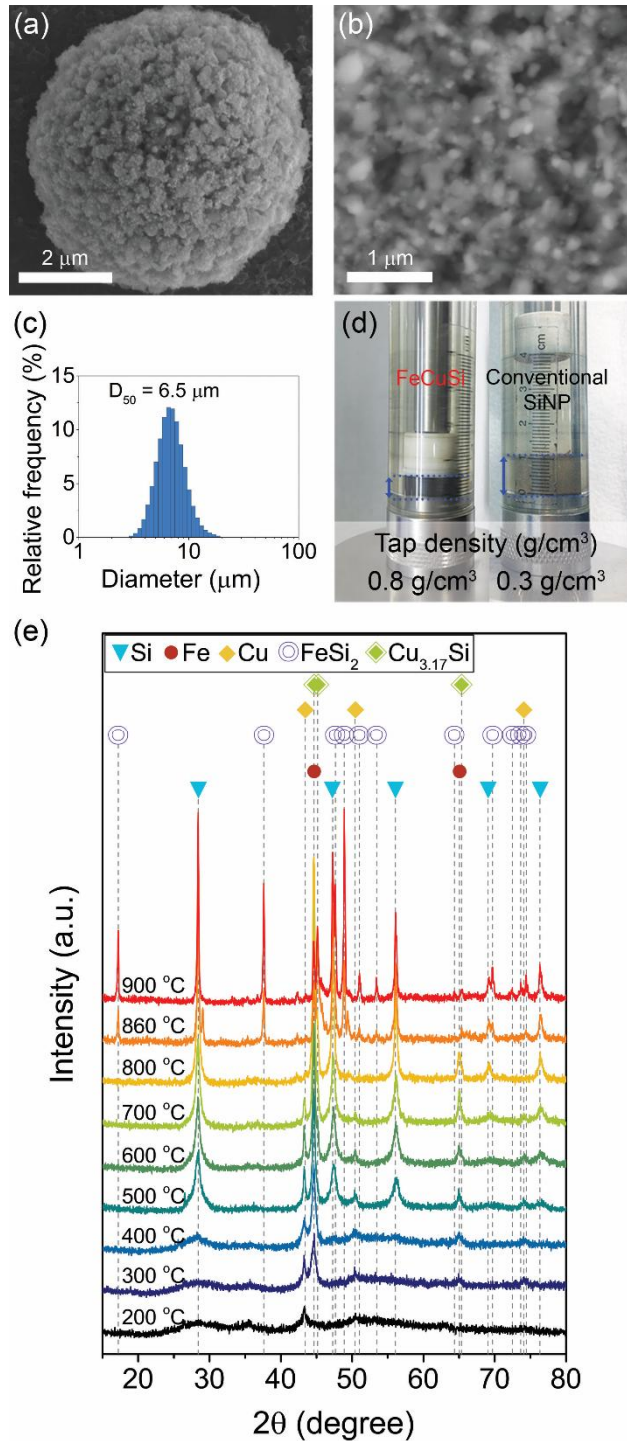


Figure. 2. 2. Characterization of FeCuSi. (a) SEM image of FeCuSi. (b) Magnified cross-sectional SEM images of FeCuSi.(c) Statistical analysis for the size distribution of FeCuSi. (d) Volume comparison between 1 g of FeCuSi and conventional Si nanoparticles after measuring tap density. (e) X-ray diffraction patterns of FeCuSi as a function of heating temperature.

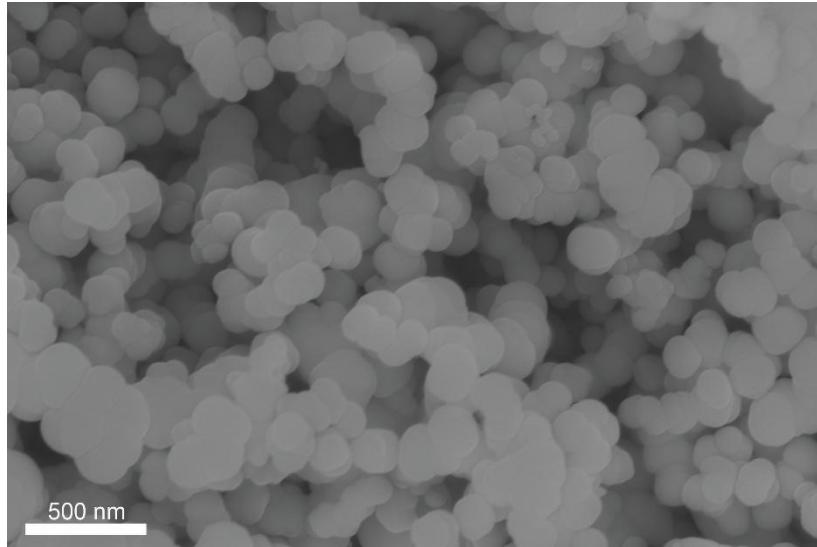


Figure 2. 3. SEM image of amorphous silicon nanoparticles which were synthesized through chemical vapor deposition (CVD) of monosilane (SiH_4).

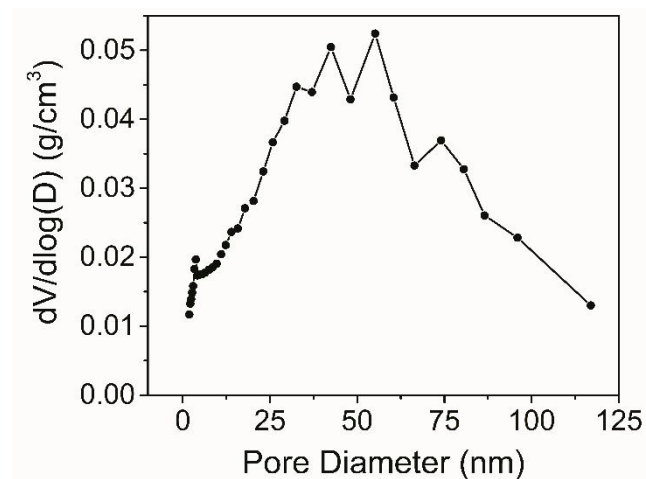


Figure 2. 4. Pore size distribution of FeCuSi. The derivative volume with respect to the pore diameter shows where clusters of pores of a particular diameter occur.

No.	Index	2 θ (deg)
Fe		
1	(011)	44.64
2	(002)	65.04
Cu		
1	(111)	43.40
2	(002)	50.40
3	(022)	74.06
Si		
1	(111)	28.40
2	(022)	47.26
3	(113)	56.06
4	(004)	69.04
5	(133)	76.32
FeSi ₂		
1	(001)	17.20
2	(011)	37.62
3	(110)	47.64
4	(012)	48.90
5	(111)	51.02
6	(003)	53.44
7	(013)	64.36
8	(020)	69.70
9	(021)	72.46
10	(004)	73.64
11	(113)	74.42
Cu _{3.17} Si		
1	(110)	43.40
2	(103)	50.40
3	(023)	74.06

Table 2. 1. The peak list of Fe, Cu, Si, FeSi₂, and Cu_{3.17}Si with the index from the XRD analysis. The references of Fe, Cu, Si, FeSi₂, and Cu_{3.17}Si are ICSD 631729, 627117, 43403, 24360, 160694, respectively.

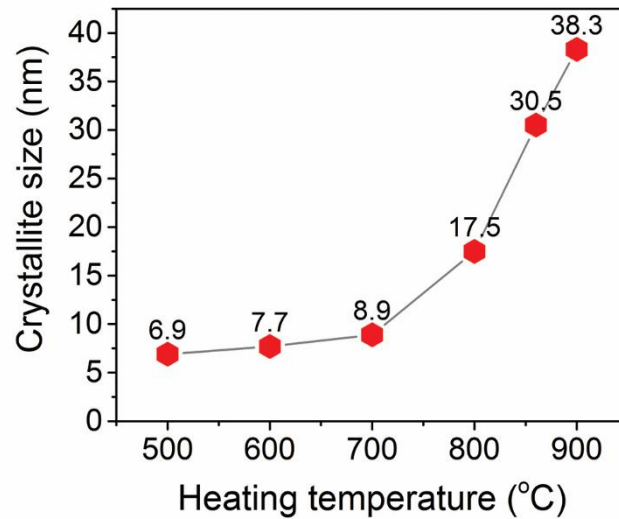


Figure 2. 5. Crystallite sizes of FeCuSi with different heating temperatures.

Crystallite sizes of FeCuSi as a function of heating temperature were estimated with the Halder-Wagner method in PDXL software (Rigaku).

$$\left(\frac{\beta}{\tan \theta}\right)^2 = \frac{K\lambda}{L} \cdot \frac{\beta}{\tan \theta \sin \theta} + 16e^2$$

β = integral breadth

K = shape factor

λ = wave length of the X-ray

L = crystallite size

High resolution transmission electron microscopy (HR-TEM) was performed to investigate the morphology of FeCuSi in detail (**Fig. 2. 6**). The sample for cross-sectional view was prepared by FIB with epoxy soak and carbon deposition in order to make protective layers in the top and void of the sample against the damage derived from Ga ion beam. As seen in high angle annular dark field in a scanning transmission electron microscope (HAADF-STEM) image (**Fig. 2. 6a**), the morphology accurately coincides with that of cross sectional SEM image. In addition, it was confirmed through energy-dispersive X-ray spectroscopy (EDS) analysis that Fe (red) and Cu (yellow) elements are extremely well distributed in the Si (cyan) secondary structure. For the sake of the elemental characterization of Fe, Cu, and Si, point analysis was conducted in high magnification (**Fig. 2. 6b**). It turned out that large circle, small circle, and shapeless one correspond to Si, Fe, and Cu elements, respectively, indicating morphology of metal silicides. Besides, mixed elements detection of Si and Fe at small circle and Si and Cu at shapeless one confirmed the formation of metal silicides. EDS line scan profile also strengthen the basis of coexistence of Fe, Cu, and Si (**Fig. 2. 7**). Therefore, in sum, as described in HAADF-STEM images and EDS analysis, numerous nano-sized metal silicides were adhered to spherical Si secondary structure evenly for the purpose of improving both structural stability and electrical conductivity.

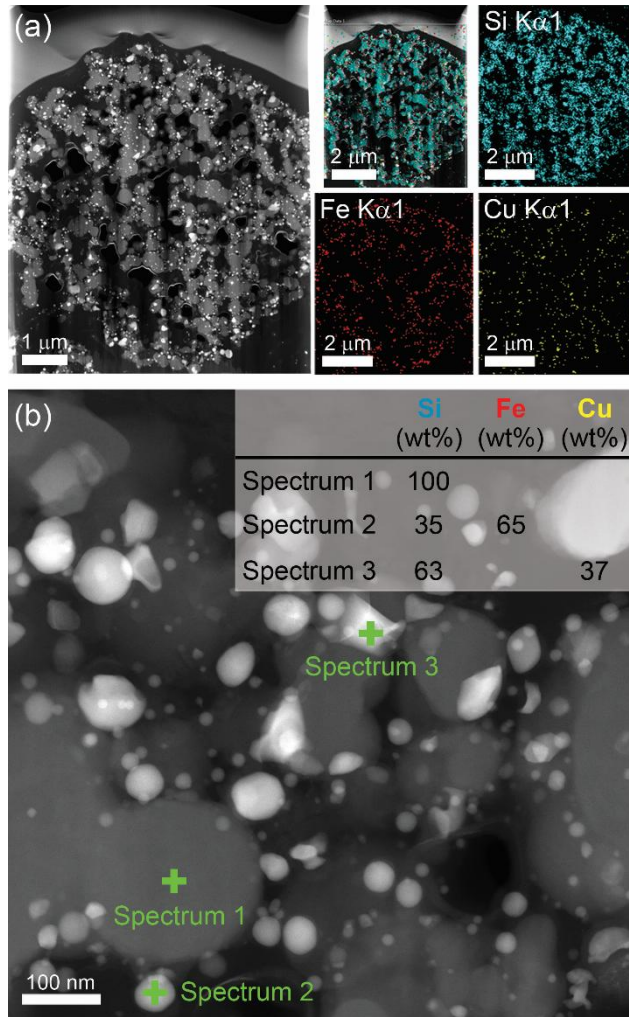


Figure. 2. 6. Detailed investigation of FeCuSi with TEM analysis. (a) HAADF-STEM image and EDS mapping of FeCuSi in cross sectional view. Cyan, red, and yellow indicate Si, Fe, and Cu respectively. (b) Magnified HAADF-STEM image of FeCuSi and EDS point analysis for Si nanoparticle, iron silicide, and copper silicide.

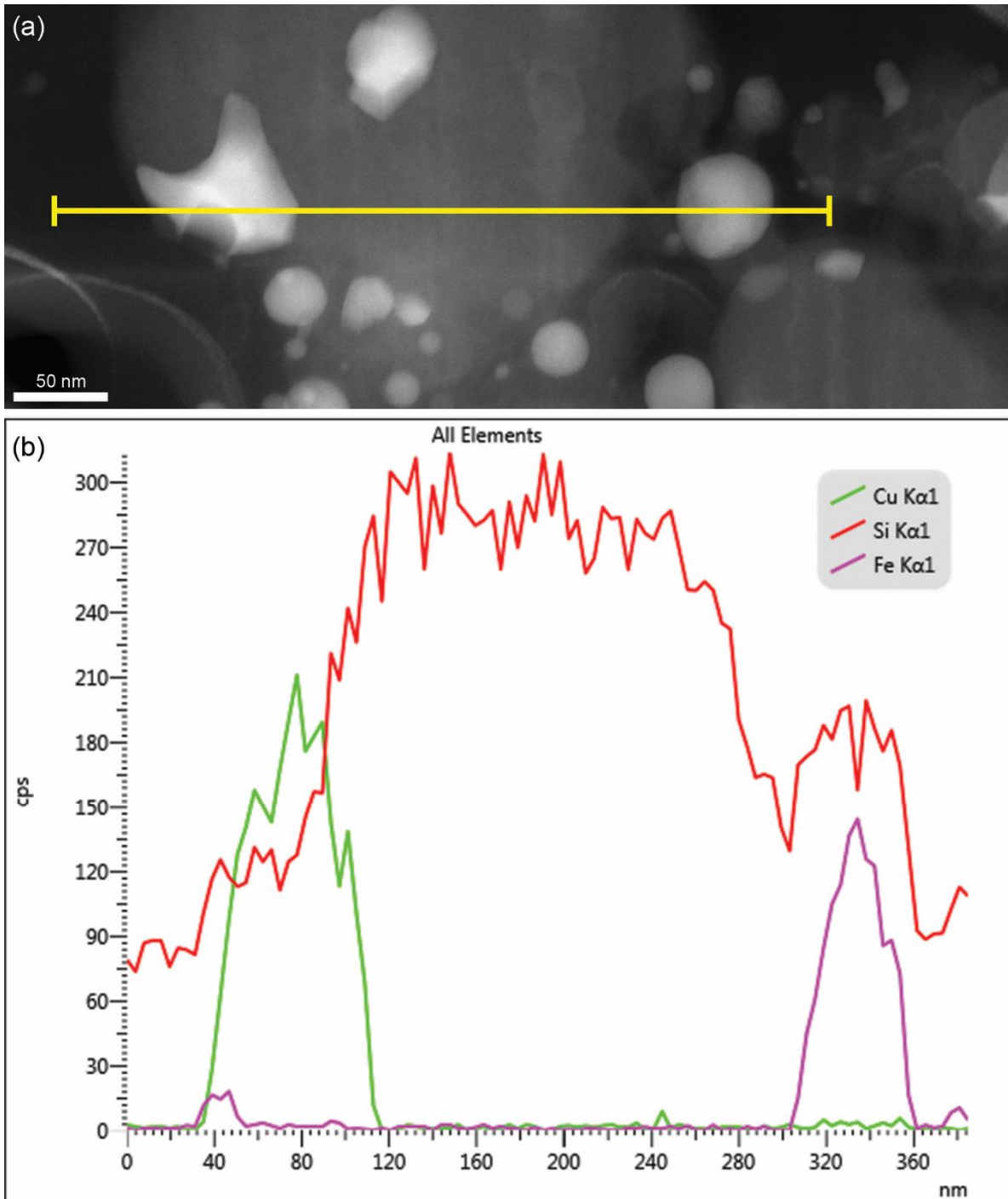


Figure 2. 7. EDS line scan of FeCuSi. (a) Magnified HAADF-STEM image of FeCuSi. (b) Element profile according to line scanning in (a).

As an investigation into the effect of our material design on Si anode, electrochemical properties of FeCuSi were evaluated with coin-type lithium half-cell at 24 °C (**Fig. 2. 8**). FeCuSi exhibited 1287 mAh/g of high specific capacity and 91% of outstanding initial CE at the formation cycle with 0.05C (**Fig. 2. 8a**). In addition, stable cycling for 50 cycles with 90% of capacity retention was also attained at 0.5C (**Fig. 2. 8b**). This excellent performance is attributable to the improved electrical conductivity and structural stability owing to decrease of internal resistance from countless nano-sized metal silicides and robust secondary structure with void space. As shown in Figure 2. 9, the amount of metal silicides which was controlled by the temperature of heat treatment determined both of specific capacity and initial CE, indicating that we successfully found the optimized condition for FeCuSi.

The electrochemical performance of FeCuSi was also evaluated with other industrially developed benchmarking samples (**Fig. 2. 10**), which are carbon coated silicon monoxide (C-SiO_x) and Si embedded in inactive matrix of iron silicide (FeSi₂), in order to see feasibility of the practical application with benchmark comparison. C-SiO_x and FeSi₂ exhibited 1673 and 1148 mAh/g of specific capacities with 77% and 88% of initial CE at the formation cycle with 0.05C, respectively (**Fig. 2. 8a**). Herein, three samples were blended with graphite in the industrial standard electrode condition in order to be tested in real LIB application, where the electrodes have high areal capacity (3.44 mAh/cm²) and high electrode density (1.6 g/cc) with minimized addition of binding materials (1.5 % of each styrene butadiene rubber (SBR) and carboxymethyl cellulose (CMC) in slurry). In these electrodes, graphite enables Si anodes to be readily calendered as a lubricant and conducting agent, which consequentially improves energy density of the battery.^{5,21} Each of the electrodes was adjusted to exhibit same specific capacity as ~420 mAh/g by different blending ratios of Si-based materials and graphite, where the blending ratios were 7 wt%, 5 wt% and 9 wt% for FeCuSi, C-SiO_x, and Si₂Fe, respectively. FeCuSi and FeSi₂ showed 91.4% and 91.1% of high CEs at the formation cycle with 0.1C, whereas C-SiO_x had 88.5% of relatively low CE (**Fig. 2. 10a**). In cycling test at a rate of 0.5C, the most stable cycling behavior was achieved in FeCuSi with 98% of capacity retention after 50 cycles (**Fig. 2. 10b**).

Furthermore, we also performed even full-cell test of three samples with commercialized LiCoO₂ as a cathode in the voltage range of 2.5 – 4.35V (**Fig. 2. 10c and d**). LiCoO₂ which we adopted here is considered as qualified reference cathode owing to its very high initial CE and stable cycling behavior (**Fig. 2. 11**). The ratio of negative to positive charge capacity (*N/P* ratio) was between 1.11 and 1.14 and the areal capacity of cathode was fixed with 3.42 mAh/cm² because the excessive raising of loading level of cathode is restricted by the deterioration of battery performances.⁵⁹ In the formation cycle, FeCuSi and Si₂Fe exhibited 3.08 mAh/cm² of initial areal capacity, however C-SiO_x exhibited only 2.87 mAh/cm² of initial areal capacity derived from its low CE (**Fig. 2. 10c**). Cycling test with a rate of 1C showed that FeCuSi discharged the highest capacity at each cycle during 300 cycles (**Fig. 2. 10d**) and

voltage profiles at 1st, 100th, 200th, and 300th cycle supported the cycling test result (**Fig. 2. 12**). To interpret the result of cycling test in full cells, electrode thickness changes of three samples in half-cell cycling at 0.5C were measured at lithiated state (**Fig. 2. 10e**). The thickness change of the Si electrode, which implies collective volume change of each Si-based material, is strongly related with material pulverization, volume change of whole Si electrode, and SEI accumulation.^{14, 47, 48} Hence, it can be one of simple indices of the battery failure in half-cell and full-cell. The result exhibited that smaller thickness change of FeCuSi than that of FeSi₂, owing to Si secondary structure with surplus void, decisively brought about better capacity retention. Especially, the continuous increase in electrode thickness change of FeSi₂ is regarded as one of main causes for capacity degradation during cycling. Although C-SiO_x behaved stable cycling with the lowest electrode thickness change, the discharge capacity at each cycle was smaller than that of FeCuSi because of the large irreversible capacity losses in initial cycles. The electrochemical performance of FeCuSi and benchmarking samples are summarized in **Table 2. 2**.

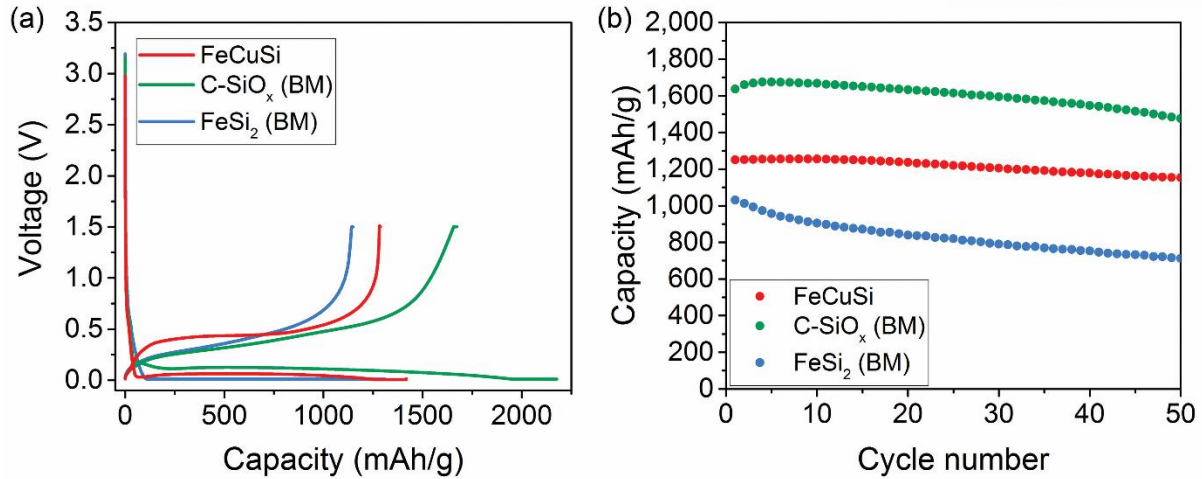


Figure 2. 8. Electrochemical characterization of FeCuSi with benchmarking samples in half-cell. (a) Voltage profiles of FeCuSi, C-SiO_x, and FeSi₂ at the formation cycle. (b) Reversible capacities of FeCuSi, C-SiO_x, and FeSi₂ for 50 cycles. The formation cycle (a) and cycling test (b) were carried out at a rate of 0.1C and 0.5C, respectively. (1C was set as 1.3 A/g, 1.1 A/g and 1.7 A/g for FeCuSi, C-SiO_x, and FeSi₂, respectively.) All electrochemical tests were performed at 25 °C in 2032R coin-type cell.

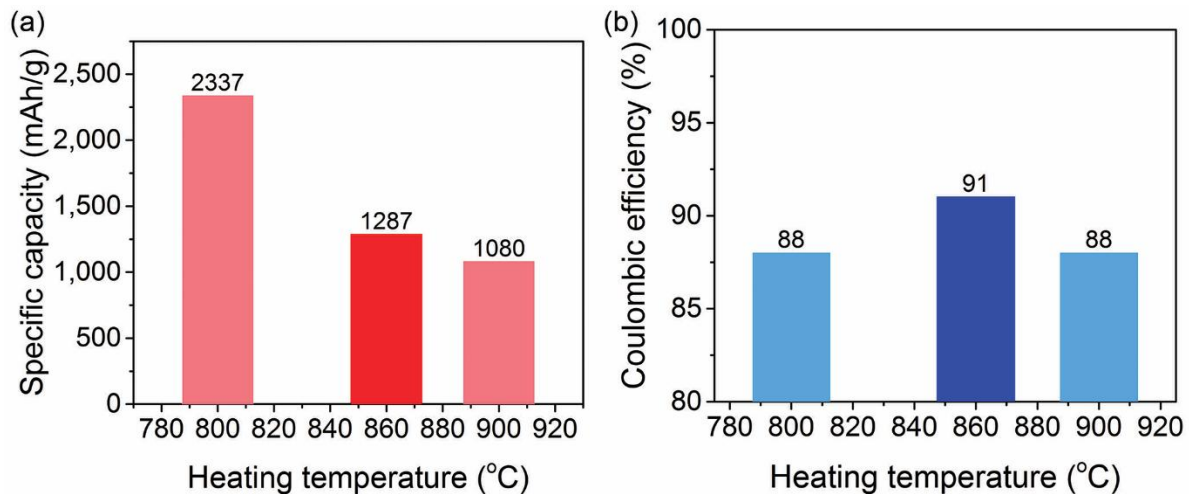


Figure 2. 9. Optimization for heating temperature of FeCuSi. (a) Reversible capacities of FeCuSi as a function of heating temperature. (b) Coulombic efficiencies of FeCuSi with diverse heating temperature. FeCuSi with 860 °C of heating temperature was optimized one.

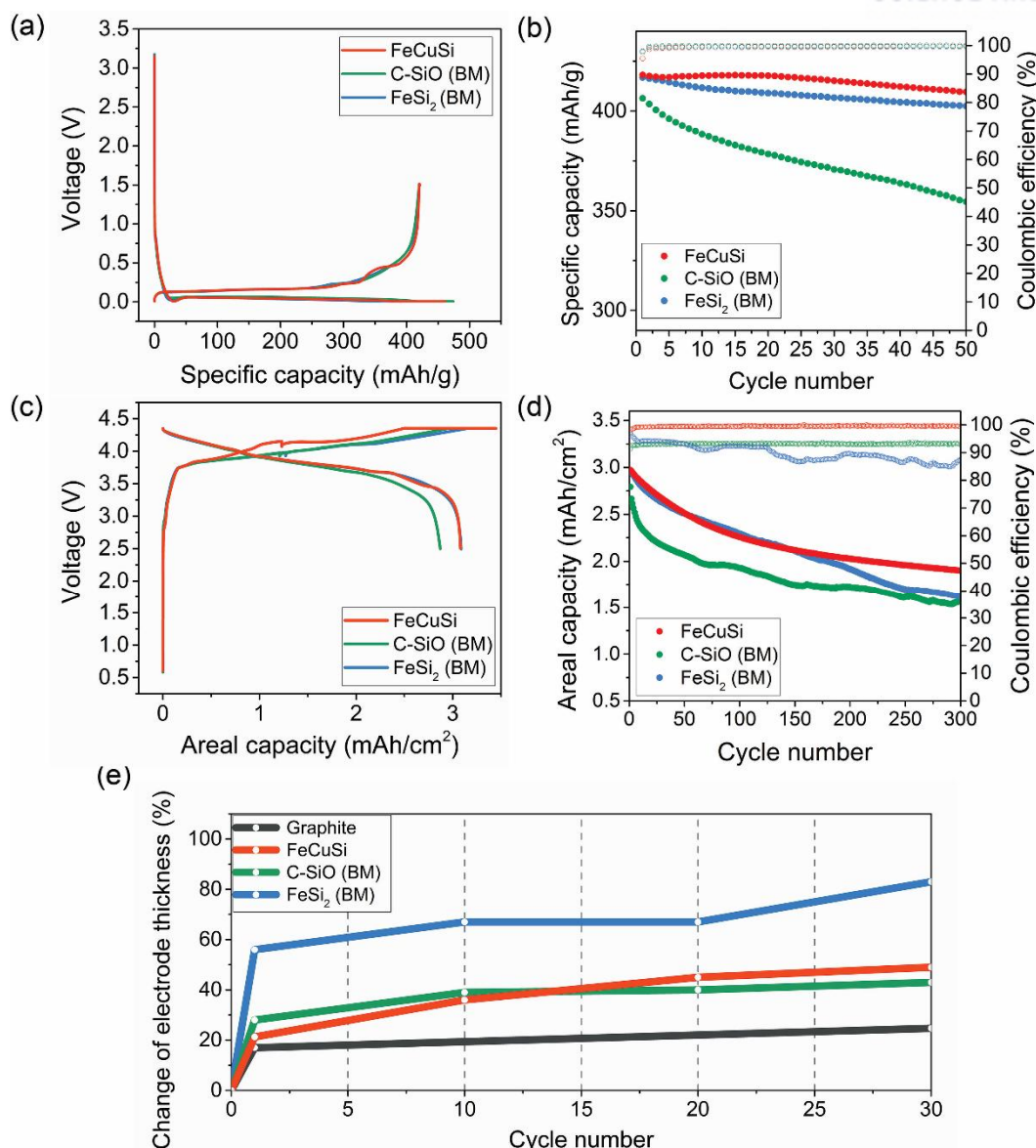


Figure. 2. 10. Electrochemical characterization of FeCuSi anode with benchmarking samples in half-cell (a, b) and full-cell (c, d) and measurement of the thickness change of electrode (e). (a) Voltage profiles of FeCuSi, C-SiO_x, and FeSi₂ at the formation cycle. (b) Reversible capacities and cycling CEs of FeCuSi, C-SiO_x, and FeSi₂ for 50 cycles. The formation cycle (a) and cycling test (b) in half-cell were carried out at a rate of 0.1C and 0.5C, respectively. (1C = 0.42 A/g.) (c) Voltage profiles of full-cell systems with LCO and different anodes of FeCuSi, C-SiO_x, and FeSi₂ at the formation cycle. (d) Reversible capacities and cycling CEs of the full-cells for 300 cycles with 1C. The formation cycle (c) and cycling test (d) in full-cell were carried out at a rate of 0.1C and 1C, respectively. (1C = 3.0 mA/cm²) All electrochemical tests were performed at 25 °C in 2032R coin-type cell. (e) The change of electrode thickness of graphite, FeCuSi, C-SiO_x, and FeSi₂ at lithiated state during 30 cycles. Electrode thickness at the lithiation state were measured with a micrometer after disassembling coin cells in Ar-filled glove box.

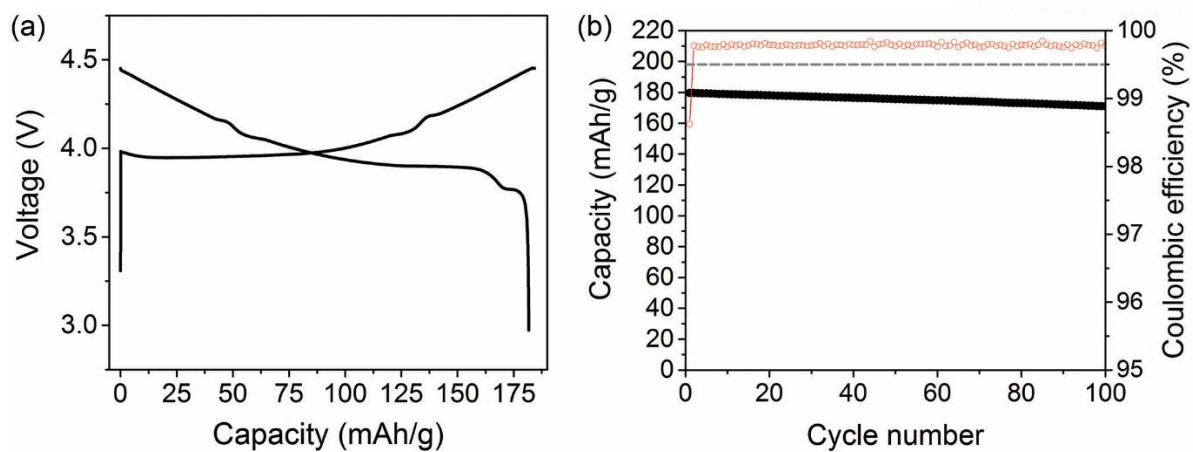


Figure 2. 11. Electrochemical properties of LCO. (a) Voltage profile of LCO at the formation cycle. (b) Reversible capacities of LCO for 100 cycles with 0.5C. The formation cycle (a) and cycling test (b) were carried out at a rate of 0.1C and 0.5C, respectively. (1C = 0.18 A/g) All electrochemical test were performed at 25 °C in 2032R coin-type cell.

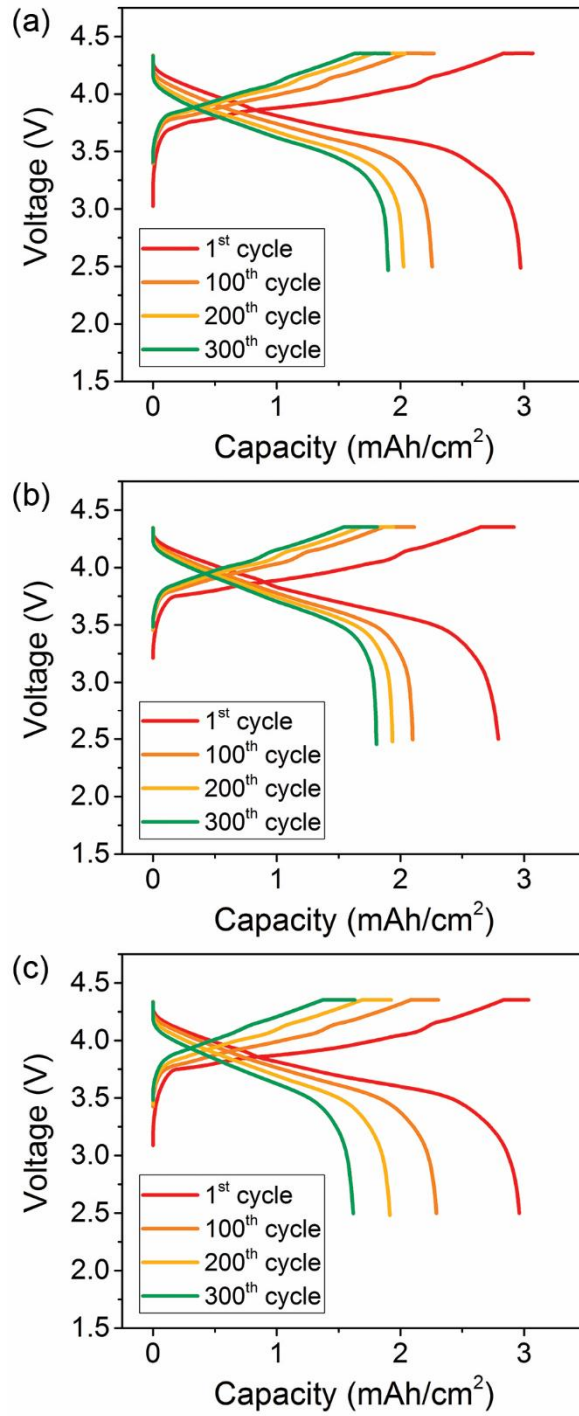


Figure 2. 12. Various voltage profiles of FeCuSi (a), C-SiO_x (b), and FeSi₂ (c) plotted for 1st, 100th, 200th, and 300th cycle.

	Only Si-based anodes		Si-Graphite blending anodes for 420 mAh/g			Full cell with Si-Graphite blending anodes and LCO		
Sample	Specific capacity (mAh/g)	Initial CE (%)	Initial CE (%)	Capacity retention (% , 50 th cycle)	Electrode thickness change (% , 30 th cycle)	Cell capacity (mAh/cm ²)	Initial CE (%)	Capacity retention (% , 300 th cycle)
FeCuSi	1287	91	91.4	98.0	49	3.08	89.4	63.9
C-SiO _x	1673	77	88.5	96.5	43	2.87	85.4	56.2
FeSi ₂	1148	88	91.1	87.2	83	3.08	89.4	54.6

Table 2. 2. Summary of electrochemical performance of FeCuSi and benchmarking samples

2.4 Conclusion

In summary, the new approach to solve the challenges of Si anode has been presented via developing Si secondary structure containing void space and numerous nano-sized metal silicides (FeCuSi) with using scalable spray drying and simple heat treatment. With exquisitely developed FeCuSi, both half-cell and full-cell test were carried out with high areal capacity (3.4 mAh/cm^2) and high electrode density (1.6 g/cc) in order to diagnose battery performances precisely. In half-cell test, where the active material was only composed of FeCuSi, 91% of initial CE with 1287 mAh/g of specific capacity was attained at the formation cycle. Besides, contrastive analysis with two of industrially developed benchmarking samples, which were C-SiO_x and FeSi₂, represented that FeCuSi exhibited the most stable cycling behavior with 98% of capacity retention after 50th cycle in high mass loading half-cell. Moreover, in terms of full-cell test with LCO, FeCuSi had superior discharge capacity at each cycle during 50th cycles with a high initial CE (89.4%) when compared with other benchmarking samples. Excellent battery performances of FeCuSi are considered as the fruits of the distinctive features which were confirmed by its material characterization: 1) Crystallized Si nanoparticles from amorphous one has several advantages in battery performances; 2) Si secondary structure with void space enable to alleviate volume change during cycling; 3) Abundant nano-sized metal silicides facilitate improvement of electrical conductivity effectively through reducing interparticle resistance; 4) Those metal silicides can not only reinforce the secondary structure as glue between Si particles but also reduce the volume expansion of the composite via diluting lithium-active phase. The accommodation of volume change during cycling was clearly elucidated in measuring electrode thickness change. However, we recognized that the cycling stability in full-cell system, under the condition of high areal capacity and high electrode density, still needs to be improved further via adjusting void space or wrapping Si secondary structure with lithium-conductive and rigid materials such as coal tar pitch. We believed that this advanced secondary structure design with metal silicides, which can alleviate volume change and have a high electrical conductivity, will be feasible candidate of next generation anode for high energy density batteries in the future.

2.5. References

1. Choi, N.-S.; Chen, Z.; Freunberger, S. A.; Ji, X.; Sun, Y.-K.; Amine, K.; Yushin, G.; Nazar, L. F.; Cho, J.; Bruce, P. G., Challenges Facing Lithium Batteries and Electrical Double-Layer Capacitors. *Angew Chem Int Edit* **2012**, *51* (40), 9994-10024.
2. Liu, J., Addressing the Grand Challenges in Energy Storage. *Adv. Funct Mater.* **2013**, *23* (8), 924-928.
3. Evarts, E. C., Lithium batteries To the limits of lithium. *Nature* **2015**, *526* (7575), S93-S95.
4. Park, C.-M.; Kim, J.-H.; Kim, H.; Sohn, H.-J., Li-alloy based anode materials for Li secondary batteries. *Chem Soc Rev* **2010**, *39* (8), 3115-3141.
5. Obrovac, M. N.; Chevrier, V. L., Alloy Negative Electrodes for Li-Ion Batteries. *Chemical Reviews* **2014**, *114* (23), 11444-11502.
6. Su, X.; Wu, Q.; Li, J.; Xiao, X.; Lott, A.; Lu, W.; Sheldon, B. W.; Wu, J., Silicon-Based Nanomaterials for Lithium-Ion Batteries: A Review. *Adv. Energy Mater.* **2014**, *4* (1).
7. Obrovac, M. N.; Christensen, L., Structural changes in silicon anodes during lithium insertion/extraction. *Electrochem Solid St* **2004**, *7* (5), A93-A96.
8. Obrovac, M. N.; Krause, L. J., Reversible cycling of crystalline silicon powder. *J Electrochem Soc* **2007**, *154* (2), A103-A108.
9. Zhang, W.-J., A review of the electrochemical performance of alloy anodes for lithium-ion batteries. *J Power Sources* **2011**, *196* (1), 13-24.
10. Nitta, N.; Yushin, G., High-Capacity Anode Materials for Lithium- Ion Batteries: Choice of Elements and Structures for Active Particles. *Part. Part. Syst. Charact.* **2014**, *31* (3), 317-336.
11. Ghadbeigi, L.; Harada, J. K.; Lettiere, B. R.; Sparks, T. D., Performance and resource considerations of Li-ion battery electrode materials. *Energ Environ Sci* **2015**, *8* (6), 1640-1650.
12. McDowell, M. T.; Lee, S. W.; Harris, J. T.; Korgel, B. A.; Wang, C.; Nix, W. D.; Cui, Y., In Situ TEM of Two-Phase Lithiation of Amorphous Silicon Nanospheres. *Nano Letters* **2013**, *13* (2), 758-764.
13. McDowell, M. T.; Lee, S. W.; Nix, W. D.; Cui, Y., 25th Anniversary Article: Understanding the Lithiation of Silicon and Other Alloying Anodes for Lithium-Ion Batteries. *Adv. Mater.* **2013**, *25* (36), 4966-4984.
14. Wu, H.; Cui, Y., Designing nanostructured Si anodes for high energy lithium ion batteries. *Nano Today* **2012**, *7* (5), 414-429.
15. Ko, M.; Oh, P.; Chae, S.; Cho, W.; Cho, J., Considering Critical Factors of Li-rich Cathode and Si Anode Materials for Practical Li-ion Cell Applications. *Small* **2015**, *11* (33), 4058-4073.
16. Szezech, J. R.; Jin, S., Nanostructured silicon for high capacity lithium battery anodes. *Energ Environ Sci* **2011**, *4* (1), 56-72.

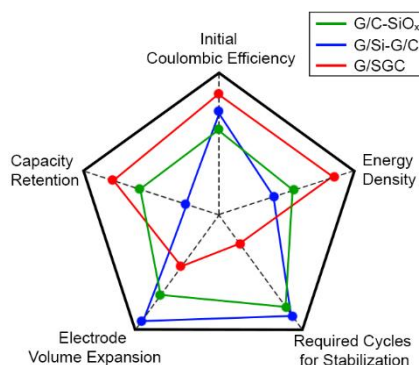
17. Ko, M.; Chae, S.; Cho, J., Challenges in Accommodating Volume Change of Si Anodes for Li-Ion Batteries. *Chemelectrochem* **2015**, *2* (11), 1645-1651.
18. Liu, N.; Lu, Z.; Zhao, J.; McDowell, M. T.; Lee, H.-W.; Zhao, W.; Cui, Y., A pomegranate-inspired nanoscale design for large-volume-change lithium battery anodes. *Nat Nanotechnol* **2014**, *9* (3), 187-192.
19. Lin, D.; Lu, Z.; Hsu, P.-C.; Lee, H. R.; Liu, N.; Zhao, J.; Wang, H.; Liu, C.; Cui, Y., A high tap density secondary silicon particle anode fabricated by scalable mechanical pressing for lithium-ion batteries. *Energ Environ Sci* **2015**, *8* (8), 2371-2376.
20. Dimov, N.; Xia, Y.; Yoshio, M., Practical silicon-based composite anodes for lithium-ion batteries: Fundamental and technological features. *J Power Sources* **2007**, *171* (2), 886-893.
21. Du, Z.; Dunlap, R. A.; Obrovac, M. N., High Energy Density Calendered Si Alloy/Graphite Anodes. *J Electrochem Soc* **2014**, *161* (10), A1698-A1705.
22. Yang, J.; Takeda, Y.; Imanishi, N.; Capiglia, C.; Xie, J. Y.; Yamamoto, O., SiO_x-based anodes for secondary lithium batteries. *Solid State Ionics* **2002**, *152*, 125-129.
23. Kim, T.; Park, S.; Oh, S. M., Solid-state NMR and electrochemical dilatometry study on Li⁺ uptake/extraction mechanism in SiO electrode. *J Electrochem Soc* **2007**, *154* (12), A1112-A1117.
24. Park, C.-M.; Choi, W.; Hwa, Y.; Kim, J.-H.; Jeong, G.; Sohn, H.-J., Characterizations and electrochemical behaviors of disproportionated SiO and its composite for rechargeable Li-ion batteries. *J Mater Chem* **2010**, *20* (23), 4854-4860.
25. Kim, J.-H.; Park, C.-M.; Kim, H.; Kim, Y.-J.; Sohn, H.-J., Electrochemical behavior of SiO anode for Li secondary batteries. *J Electroanal Chem* **2011**, *661* (1), 245-249.
26. Park, M.-S.; Rajendran, S.; Kang, Y.-M.; Han, K.-S.; Han, Y.-S.; Lee, J.-Y., Si-Ni alloy-graphite composite synthesized by arc-melting and high-energy mechanical milling for use as an anode in lithium-ion batteries. *J Power Sources* **2006**, *158* (1), 650-653.
27. Jung, H.; Kim, Y.-U.; Sung, M.-S.; Hwa, Y.; Jeong, G.; Kim, G.-B.; Sohn, H.-J., Nanosize Si anode embedded in super-elastic nitinol (Ni-Ti) shape memory alloy matrix for Li rechargeable batteries. *J Mater Chem* **2011**, *21* (30), 11213-11216.
28. Son, S.-B.; Kim, S. C.; Kang, C. S.; Yersak, T. A.; Kim, Y.-C.; Lee, C.-G.; Moon, S.-H.; Cho, J. S.; Moon, J.-T.; Oh, K. H.; Lee, S.-H., A Highly Reversible Nano-Si Anode Enabled by Mechanical Confinement in an Electrochemically Activated Li_xTi₄Ni₄Si₇ Matrix. *Adv. Energy Mater.* **2012**, *2* (10), 1226-1231.
29. Lee, K. J.; Yu, S.-H.; Kim, J.-J.; Lee, D.-H.; Park, J.; Suh, S. S.; Cho, J. S.; Sung, Y.-E., Si₇Ti₄Ni₄ as a buffer material for Si and its electrochemical study for lithium ion batteries. *J Power Sources* **2014**, *246*, 729-735.

30. Song, T.; Kil, K. C.; Jeon, Y.; Lee, S.; Shin, W. C.; Chung, B.; Kwon, K.; Paik, U., Nitridated Si-Ti-Ni alloy as an anode for Li rechargeable batteries. *J Power Sources* **2014**, *253*, 282-286.
31. Al-Maghrabi, M. A.; Suzuki, J.; Sanderson, R. J.; Chevrier, V. L.; Dunlap, R. A.; Dahn, J. R., Combinatorial Studies of Si_{1-x}O_x as a Potential Negative Electrode Material for Li-Ion Battery Applications. *J Electrochem Soc* **2013**, *160* (9), A1587-A1593.
32. Weydanz, W. J.; Wohlfahrt-Mehrens, M.; Huggins, R. A., A room temperature study of the binary lithium-silicon and the ternary lithium-chromium-silicon system for use in rechargeable lithium batteries. *J Power Sources* **1999**, *81*, 237-242.
33. Netz, A.; Huggins, R. A.; Weppner, W., The formation and properties of amorphous silicon as negative electrode reactant in lithium systems. *J Power Sources* **2003**, *119*, 95-100.
34. Netz, A.; Huggins, R. A., Amorphous silicon formed in situ as negative electrode reactant in lithium cells. *Solid State Ionics* **2004**, *175* (1-4), 215-219.
35. Jung, D. S.; Hwang, T. H.; Park, S. B.; Choi, J. W., Spray Drying Method for Large-Scale and High-Performance Silicon Negative Electrodes in Li-Ion Batteries. *Nano Letters* **2013**, *13* (5), 2092-2097.
36. Xun, S.; Xiang, B.; Minor, A.; Battaglia, V.; Liu, G., Conductive Polymer and Silicon Composite Secondary Particles for a High Area-Loading Negative Electrode. *J Electrochem Soc* **2013**, *160* (9), A1380-A1383.
37. Choi, S.; Jung, D. S.; Choi, J. W., Scalable Fracture-free SiOC Glass Coating for Robust Silicon Nanoparticle Anodes in Lithium Secondary Batteries. *Nano Letters* **2014**, *14* (12), 7120-7125.
38. Wang, P.; NuLi, Y.; Yang, J.; Zheng, Y., Carbon-coated Si-Cu/graphite Composite as Anode Material for Lithium-ion Batteries. *Int J Electrochem Sc* **2006**, *1* (3), 122-129.
39. Usui, H.; Meabara, K.; Nakai, K.; Sakaguchi, H., Anode Properties of Composite Thick-Film Electrodes Consisted of Si and Various Metal Silicides. *Int J Electrochem Sc* **2011**, *6* (6), 2246-2254.
40. Ko, M.; Chae, S.; Jeong, S.; Oh, P.; Cho, J., Elastic a-Silicon Nanoparticle Backboned Graphene Hybrid as a Self-Compacting Anode for High-Rate Lithium Ion Batteries. *Acs Nano* **2014**, *8* (8), 8591-8599.
41. Liu, X. H.; Zhong, L.; Huang, S.; Mao, S. X.; Zhu, T.; Huang, J. Y., Size-Dependent Fracture of Silicon Nanoparticles During Lithiation. *Acs Nano* **2012**, *6* (2), 1522-1531.
42. Fedorov, A. S.; Popov, Z. I.; Kuzubov, A. A.; Ovchinnikov, S. G., Theoretical study of the diffusion of lithium in crystalline and amorphous silicon. *Jetp Lett+* **2012**, *95* (3), 143-147.
43. Carne-Sanchez, A.; Imaz, I.; Cano-Sarabia, M.; Maspoch, D., A spray-drying strategy for synthesis of nanoscale metal-organic frameworks and their assembly into hollow

- superstructures. *Nat Chem* **2013**, 5 (3), 203-211.
44. Yuvaraj, S.; Lin, F. Y.; Chang, T. H.; Yeh, C. T., Thermal decomposition of metal nitrates in air and hydrogen environments. *J Phys Chem B* **2003**, 107 (4), 1044-1047.
 45. Atiemo-Obeng, V. A.; Penney, W. R.; Armenante, P.; Hand-book of Industrial Mixing, John Wiley&Sons, INC., 2004; pp 543-584.
 46. Zheng, H.; Li, J.; Song, X.; Liu, G.; Battaglia, V. S., A comprehensive understanding of electrode thickness effects on the electrochemical performances of Li-ion battery cathodes. *Electrochim Acta* **2012**, 71, 258-265.
 47. Radvanyi, E.; Porcher, W.; De Vito, E.; Montani, A.; Franger, S.; Larbi, S. J. S., Failure mechanisms of nano-silicon anodes upon cycling: an electrode porosity evolution model. *Phys Chem Chem Phys* **2014**, 16 (32), 17142-17153.
 48. Yi, R.; Dai, F.; Gordin, M. L.; Chen, S.; Wang, D., Micro-sized Si-C Composite with Interconnected Nanoscale Building Blocks as High-Performance Anodes for Practical Application in Lithium-Ion Batteries. *Adv. Energy Mater.* **2013**, 3 (3), 295-300.
 49. Kim, C.; Ko, M.; Yoo, S.; Chae, S.; Choi, S.; Lee, E.-H.; Ko, S.; Lee, S.-Y.; Cho, J.; Park, S., Novel design of ultra-fast Si anodes for Li-ion batteries: crystalline Si@amorphous Si encapsulating hard carbon. *Nanoscale* **2014**, 6 (18), 10604-10610.
 50. Lu, Z.; Liu, N.; Lee, H.-W.; Zhao, J.; Li, W.; Li, Y.; Cui, Y., Nonfilling Carbon Coating of Porous Silicon Micrometer-Sized Particles for High-Performance Lithium Battery Anodes. *Acs Nano* **2015**, 9 (3), 2540-2547.

Chapter 3

One-to-one Comparison of Graphite-blended Negative Electrodes using Silicon Nanolayer-embedded Graphite versus Commercial Benchmarking Materials for High-energy Lithium-ion Batteries



While existing carbonaceous anodes for lithium-ion batteries (LIBs) are approaching a practical capacitive limit, Si has been extensively examined as a potential alternative because it shows exceptional gravimetric capacity (3579 mAh/g) and abundance. However, the actual implementation of Si anodes is impeded by difficulties in electrode calendaring processes and requirements for excessive binding and conductive agents, arising from the brittleness, large volume expansion (> 300%), and low electrical conductivity (1.56×10^{-3} S/m) of Si. In one rational approach to using Si in high-energy LIBs, mixing Si-based materials with graphite has attracted attention as a feasible alternative for next-generation anodes. Here we demonstrate graphite-blended electrodes with Si nanolayer-embedded graphite/carbon (G/SGC) and perform detailed one-to-one comparisons of these electrodes with industrially developed benchmarking samples under the industrial electrode density (> 1.6 g/cc), areal capacity (> 3 mAh/cm²), and a small amount of binder (3 wt%) in a slurry. Compared to the benchmarking samples, G/SGC was successful in protecting the electrode integrity from volume variation, and exhibited the high first-cycle coulombic efficiency (CE) of 92% and a rapid increase of cycling CE exceeding 99.5% after only the third cycle. As a result, even in a full-cell configuration, the G/SGC material allowed a higher cell capacity (3.07 mAh/cm²) during the first formation cycle and a more stable cycling behavior, with the capacity retention of 67.1% and volumetric energy density of 387 Wh/L, than the benchmarking samples showed. Because of the favorable compatibility between SGC and conventional graphite, and the well-established structural features of SGC, great potential is envisioned. Since this feasibility study utilized realistic test methods and criteria, the rigorous

benchmarking comparison presented a comprehensive understanding for developing and characterizing Si-based anodes for practicable high-energy LIBs.

This chapter has been published.

Reproduced with permission from Chae, S.; Kim, N.; Ma, J.; Cho, J.; Ko, M., One-to-One Comparison of Graphite-Blended Negative Electrodes Using Silicon Nanolayer-Embedded Graphite versus Commercial Benchmarking Materials for High-Energy Lithium-Ion Batteries. *Adv. Energy Mater.* **2017**, 7 (15), 1700071.

3. 1. Introduction

Rechargeable Li-ion batteries (LIBs) are deemed the most important power sources for portable electronic devices, with a steady increase in energy density by 7–10% per year.^{1, 2} However, for forthcoming applications in electric vehicles (EVs) and large-scale energy storage systems (ESSs), achieving higher energy densities is the most urgent priority in the LIB industry.³⁻⁶ Considering practical relevance, Si–graphite blending has been investigated as a feasible technique for next-generation negative electrode materials with improved energy densities,⁷⁻¹⁰ since the tremendous volume expansion of Si-dominant electrodes has hindered their application in practical batteries until now.¹¹⁻¹³ In graphite-blended electrodes, the graphite offers high electrical conductivity to the electrode components and permits electrode calendaring to promote electrode density by acting as a lubricant.¹⁴ Furthermore, graphite enhances the initial coulombic efficiency (CE) and cyclic stability while mitigating electrode volume expansion.^{7, 14, 15} For these advantages, the practical utilization of Si in anodes has been vigorously studied via blending with graphite.

Moderate anode materials for graphite blending, including structures composed of nanoscale Si as inactive/active matrices, such as silicon oxide (SiO_x)^{16, 17, 18} and Si-containing graphite/carbon (Si-G/C) composites,¹⁹⁻²¹ have been recognized as modern anode materials with high tap densities, low specific surface areas, and scalable production methods, as well as high specific capacities. Heterogeneous matrices of Si-based materials act as buffer phases to mitigate the induced stress from Si volume variations. They suppress side reactions and promote capacity retention compared to those from Si anodes without matrix formats during electrochemical cycling. Recently, it was reported that a graphite-blended electrode containing 3 wt% SiO_{1.06} achieved the reversible specific capacity of 397 mAh/g with a stable capacity retention of 76% after 200 cycles in a full-cell system.²²

Si–G/C composites, in which Si nanoparticles (SiNPs) are anchored to graphite surfaces with pitch as a carbon source, have also been examined as industrially developed LIB anode materials.^{19-21, 23-25} Graphite and the included carbon source act as a ductile matrix and glue, respectively, for trapping

SiNPs, thereby accommodating Si volume expansion during cycling and providing high electrical conductivity and structural stability incorporated with the merits of nanoscale Si. Yoon et al. reported on Si–G/C composites fabricated by a mechanical milling method that demonstrated a reversible specific capacity of 655 mAh/g, high first-cycle CE of 86%, and stable capacity retention of 71.4% after 300 cycles.²⁰ Nevertheless, Si–G/C composites face critical challenges, such as the uniform distribution of SiNPs on graphite surfaces, optimization of the Si/G proportions, and the problem of graphite crumbling in conventional mechanical milling.

Recently, as a promising candidate for viable next-generation anode materials, we reported on scalable Si nanolayer-embedded graphite/carbon hybrids (SGCs) fabricated by chemical vapor deposition (CVD).²⁶ The SGC hybrids exhibited the specific reversible capacity of 523 mAh/g and a first-cycle CE of 92%. They also showed the stable capacity retention of 96% after 100 cycles, with a rapid increase in cycling CE to exceed 99.5% after only six cycles at industrial electrode density and areal capacity loading, when composited with 3.2 wt% of binder in a slurry.

In order to predict the practical implementation of commercially oriented anode materials, further detailed analyses and feasibility studies are required. Although numerous approaches for the advance of Si anodes have been reported, comparisons with commercially oriented benchmarks are rarely suggested from a comprehensive industrial perspective. Furthermore, as Obrovac et al. urged battery researchers to estimate volumetric energy densities or provide exact information to allow the estimation of volumetric energy densities in their comprehensive review¹⁵, it is necessary to examine recent developments with consideration for their implementation in practical cells. Herein, we have focused on the one-to-one comparison of the SGC hybrid anode material with state-of-the-art benchmarking samples, including carbon-coated SiO_x (denoted as C-SiO_x) and a Si-containing graphite/carbon composite (denoted as Si–G/C), in graphite-blended electrodes. For definite and effective examination of different Si anodes, the battery cycling phenomena with morphological investigation will be mainly discussed as a priority comparison factor. Based on our benchmarking comparison, we present a concrete guide to reasonable feasibility studies and provide profound insight in the characterization of Si anodes for other researchers. To the best of our knowledge, few previous reports have suggested tests of the overall electrochemical properties of full-cell configurations utilizing industrial electrode requirements.²⁷ Hence, in this study, all electrochemical tests are conducted at industrial electrode density (> 1.6 g/cc) and areal capacity (> 3.4 mAh/cm²), using a water-soluble styrene–butadiene rubber/carboxymethyl cellulose (SBR/CMC) binder composition (total 3.0 wt %) in both half- and full-cell systems. In addition, for a rational comparison, the specific reversible capacities of all samples are fixed at 420 mAh/g by blending with graphite in different proportions, where the blending ratios are 5 wt%, 19 wt%, and 38 wt% for C-SiO_x, Si–G/C, and SGC, respectively. Detailed material

characterizations are conducted by diverse analytical tools, and all critical factors influencing electrode performances were thoroughly investigated from an industrial perspective in accordance with the structural features, cycling behavior with stabilized CE, and volume variations of the electrodes before and after electrochemical cycling.

3.2. Experimental Detail

Synthesis of SGC: The preparation procedures of SGC are the same with our previous report.²⁶ In short, commercially available spherical-type graphite was uniformly coated with Si nanolayer and carbon layer by silane (SiH₄) and acetylene (C₂H₂) gas, successively.

Materials Characterization: Particle size distributions of C-SiO_x, Si-G/C, and SGC were easily estimated with the Fraunhofer approximation by laser diffraction particle size analysis instrument (Microtrac S3500, Microtrac). Specific surface area was determined by the Brunauer–Emmett–Teller (BET) theory with surface area and porosity analyzer (TriStar II, micromeritics). Tap density was measured by density analyzer (GeoPyc 1360, micromeritics) with tapping 1.5 g of each sample in the container. The morphologies of C-SiO_x, Si-G/C, SGC, and their graphite-blended electrodes were investigated with scanning electron microscopy (SEM, Verios 460, FEI). High resolution transmission electron microscopy (HR-TEM, JEM-2100F, JEOL) was performed for detailed characterization. Dual-beam focused ion beam (FIB, Helios 450HP, FEI) was utilized for sampling the particles for the cross-sectional view and TEM. Energy-dispersive spectroscopy (EDS) mapping analysis was carried out in SEM equipped with EDS (Bruker XFlash 6130) and in HR-TEM equipped with EDS (Oxford Aztec).

Electrochemical Measurement: In order to fabricate the working electrode, the slurry composed of the active material, the conductive additive (carbon black), and the binders (sodium carboxymethyl cellulose (CMC) and styrene butadiene rubber (SBR)) was homogeneously mixed by homogenizer with the mass ratio of 96:1:1.5:1.5. For the graphite-blended electrodes, C-SiO_x, Si-G/C, and SGC were blended with the graphite in mass the ratio of 5%, 19%, and 39%, respectively. The slurry was coated on the copper foil up to 3.4 mAh/cm² of high areal capacity and then dried at 80 °C. The electrode density was tuned as 1.6 g/cc with calendaring process. Before all the cell assembly process, the electrode went through vacuum drying at 110 °C overnight. CR2032 type was utilized for both of half- and full-cell. The electrolyte was 1.3M LiPF₆ in mixture of ethylene carbonate, ethyl methyl carbonate, and diethyl carbonate (3:5:2, by volume) with 10% fluoroethylene carbonate (Panax Starlyte, Korea). For the prototype full-cell, lithium cobalt oxide (LCO) was adopted as the cathode with 1.1 of N/P ratio. The electrochemical performances were measured in two steps with the constant current-constant voltage (CC-CV) mode, the formation and the cycling. In the formation, the half-cell was tested in the voltage window between 0.005 and 1.5 V versus Li⁺/Li. The full-cell was examined in the voltage

window between 2.7 and 4.35 V versus Li^+/Li . Then, in the cycling, the half-cell was carried out in a voltage range of 0.005-1V versus Li^+/Li and the full-cell was in the same voltage window with that of the formation stage. Detailed testing protocols are given in **Table 3. 1**. TOSCAT-3100 battery cycler (TOYO SYSTEM) was operated for the electrochemical measurement. In order to measure the electrode volume expansion, the cells were disassembled in Ar-filled glove box and rinsed with dimethyl carbonate. The electrode volume expansion was estimated based on thickness change from micrometer (Mitutoyo).

Test type	Step	Voltage window	CC-CV mode
Half-cell (Anode)	Formation	0.005 – 1.5 V	0.1C for charging and discharging 0.01C cut off at 0.005V
	Cycling	0.005 – 1V	0.5C for charging and discharging 0.01C cut off at 0.005V
Half-cell (Cathode)	Formation	3 – 4.45 V	0.1C for charging and discharging 0.01C cut off at 4.4V
	Cycling	3 – 4.45 V	0.5C for charging and discharging 0.01C cut off at 4.4V
Full-cell	Formation	2.7 – 4.35V	0.1C for charging and discharging 0.01C cut off at 4.35V
	Cycling	2.7 – 4.35V	0.5C for charging and 1C for discharging 0.02C cut off at 4.35V

Table 3. 1. Battery testing protocols for the half-cell and the full-cell.

3. 3. Results and discussion

3. 3. 1. Characterization of SGC and benchmarking samples

To verify the physical properties of SGC and the state-of-the-art benchmarking samples (C-SiO_x and Si-G/C), we analyzed the size distribution, tapped density, and specific surface area of each type of particle. As shown in **Figure 3. 1a**, the average particle size (D_{50}) of C-SiO_x is 5 μm , while those of the Si-G/C, SGC, and conventional graphite are confirmed as approximately 17 μm . The specific surface areas of C-SiO_x, SGC, and graphite are estimated to be in the range of $\sim 4\text{--}5\text{ m}^2/\text{g}$ by the Brunauer–Emmett–Teller (BET) method, with high tapped densities of approximately $\sim 1\text{--}1.1\text{ g/cc}$. Si-G/C shows a slightly higher specific surface area of $10\text{ m}^2/\text{g}$ and lower tap density of 0.8 g/cc (**Fig. 3. 1b,c**). These physical properties of micrometer-sized particles, high tapped densities, and small specific surface areas are considered important in battery industries. Proper particle sizes and high tap densities promote compatibility with conventional graphite in fabricating blended electrodes, particularly regarding homogeneous slurry formation and increased volumetric energy density.²⁸ Small specific surface areas also lower the viscosities of solvents in the slurry and the consumption of binder, thereby lowering the amount of solvent necessary and raising the binding strength.²⁹

For more detailed identification of the structural features and chemical compositions of C-SiO_x, Si-G/C, and SGC, we performed field-emission scanning electron microscopy (FE-SEM) with energy dispersive X-ray spectroscopy (EDS), and high-resolution transmission electron microscopy (HR-TEM) with fast Fourier transform (FFT) analysis. Cross-sectional single particles were prepared using a focused ion beam (FIB) workstation after coating with Ti to protect the particle morphology from the permeation of Ga⁺ during sample preparation. As presented in **Fig. 3. 1d**, the SEM images at high and low magnification show irregularly shaped C-SiO_x with an uneven coating layer on the surface. Through EDS mapping analysis (**Fig. 3. 1e, f**), it is confirmed that the coating layer is carbon with a measured thickness of approximately 25 nm on the SiO_x particle surface. Moreover, disproportionate Si is observed inside the cross-sectional particle,³⁰ and the size of the Si crystallite in C-SiO_x is approximately 5–8 nm, which agrees well with the HR-TEM and FFT images shown in **Fig. 3. 1g**. Both the Si-G/C and SGC particles exhibit spherical-shaped graphite particles comprising nanoscale Si and disordered carbon on their surfaces and beneath their inner pores (**Fig. 3. 1h–j and Fig. 3. 1l–n**). As shown in **Fig. 3. 1h**, the SEM images of Si-G/C depict a randomly distributed and partially aggregated coating layer on the particle surface. EDS mapping analysis of the cross-sectional Si-G/C particle (**Fig. 3. 1i, j**) elucidate the morphology: a large amount of $\sim 150\text{-nm}$ Si millet-like flakes are closely held by the carbon matrix and non-homogeneously piled onto the graphite surface, which retains the total thickness of $0.5\text{ }\mu\text{m}$, and are simultaneously filled in the inner pores of the spherical graphite particle. Such a thick and non-uniform coating morphology of excessive Si flakes and carbon can be expected to cause structural

failure by Si volume variations after long-term cycling, suggesting mechanical instability.^{12,31} Moreover, the HR-TEM and FFT images in **Fig. 3. 1k** demonstrate that the Si flakes and carbon matrix are crystalline and amorphous in phase, respectively. Meanwhile, the SEM images of the SGC at high and low magnifications indicate a smooth surface texture, as shown in **Fig. 3. 1l**. From the EDS mapping analysis of the cross-sectioned SGC particle, a thin and homogenous Si nanolayer is confirmed to coat the surface of the graphite. The nanolayer is also present beneath the particle's inner pores, retaining a uniform thickness of 15 nm. The layer is 30 times thinner than that in the Si-G/C benchmarking sample (**Fig. 3. 1m, n**). Moreover, the carbon coating layer is uniformly formed on the outmost surface of the Si nanolayer, where the thickness of the carbon coating is approximately 5 nm. Notably, the Si nanolayer on the inner pores of SGC possesses sufficient room for Si volume expansion during lithiation, promoting stable cycling behavior, and the post-coated carbon layer decreases the specific surface area of the particle resulting in enhanced cycling efficiency.²⁶ The HR-TEM and FFT images in **Fig. 3. 1l** clearly show that the Si and coated carbon are both amorphous in phase.

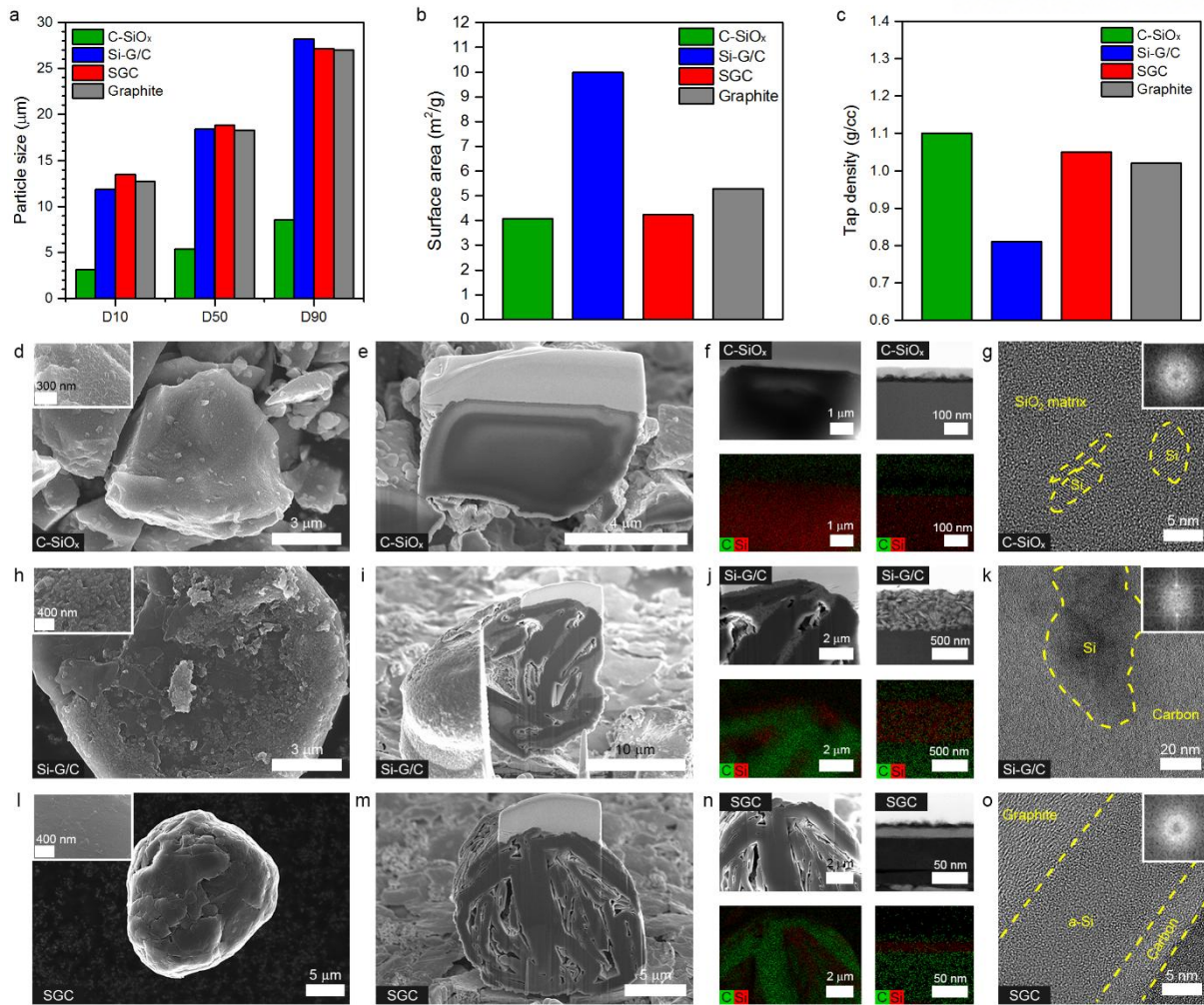


Figure 3. 1. Material characterization of pristine SGC and benchmarking samples. Benchmarking comparison for physical properties with a) particle size distribution, citing D10, D50, and D90, b) specific surface area based on BET theory, and c) tap density after mechanically tapping a container. Morphological comparison of C-SiO_x (d-g), Si-G/C (h-k), and SGC (l-o), using SEM images with top and cross-sectional views, EDS mapping from cross-sectional views, and HR-TEM images of the interfacial regions. SEM images (d, h, l) and HR-TEM images (g, k, o) include insets depicting magnified images and FFT analyses, respectively.

3. 3. 2. Electrochemical testing of SGC and benchmarking samples in the net electrode

To characterize the battery performances of pristine C-SiO_x, Si-G/C, and SGC, electrochemical evaluation was performed in the constant current–constant voltage (CC–CV) mode using coin-type Li half-cell (2032R) configurations at 24 °C (**Fig. 3. 2**). As presented in **Figure 3. 2a**, the benchmarking samples, including C-SiO_x and Si-G/C, exhibited the specific reversible capacities of 1600 mAh/g and 680 mAh/g, with first-cycle CEs of 76% and 85%, respectively. SGC showed the relatively high first-cycle CE of 92% and a reversible specific capacity of 523 mAh/g (details given in **Figure 3. 2**).

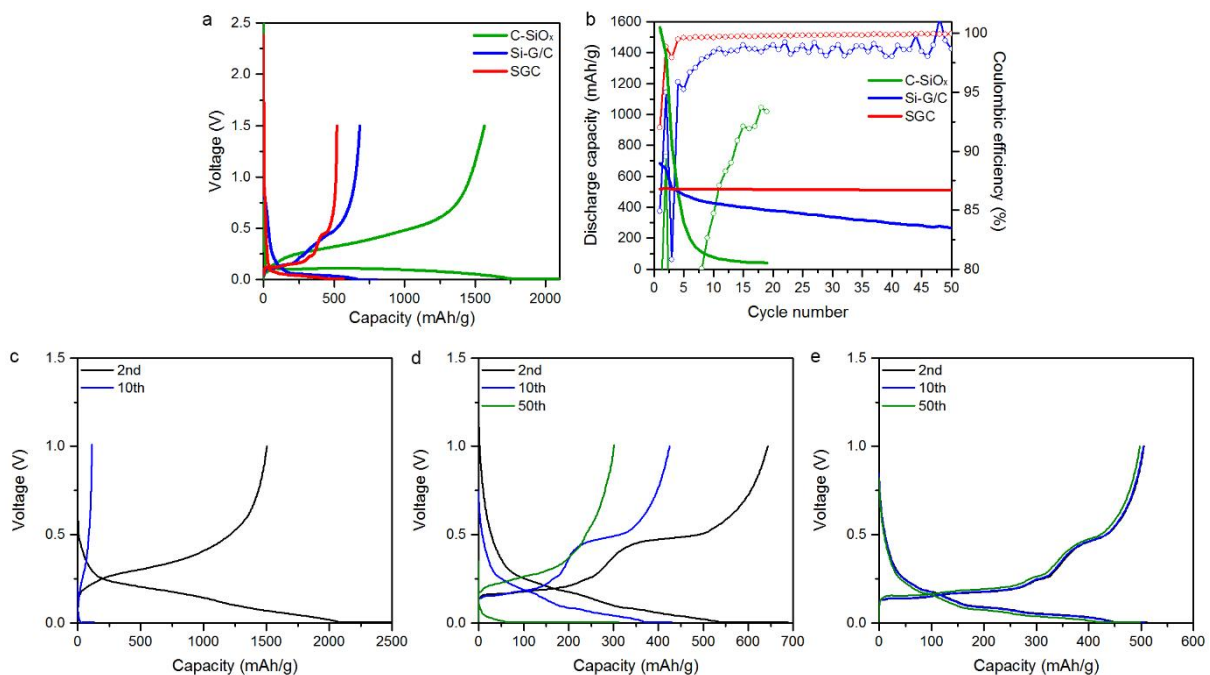


Figure 3. 2. Electrochemical evaluation of C-SiO_x, Si-G/C, and SGC in half-cell. a) Voltage profiles at the first cycle. b) Cycling performances at the charge/discharge rate of 0.5C with CE plots for 50 cycles. c-e) Various voltage profiles of C-SiO_x (c), Si-G/C (d), and SGC (e) at second, tenth, and fiftieth cycle.

3. 3. 3. Electrochemical testing of SGC and benchmarking samples in graphite-blended system

Based on the electrochemical characteristics of non-blended materials, we performed a practical comparison of the benchmarking samples and SGC through graphite blending, where the specific reversible capacity of all electrodes was fixed at 420 mAh/g by using blending ratios of 5 wt%, 19 wt%, and 38 wt% for C-SiO_x, Si-G/C, and SGC, respectively (named as G/C-SiO_x, G/Si-G/C, and G/SGC henceforth). Moreover, overall electrodes were fabricated following the industrial requirements with high electrode densities (> 1.6 g/cc), areal capacity loadings (> 3.4 mAh/cm²), and limited amounts of SBR-CMC binder (total 3.0 wt%) in the slurry. **Figure 3. 3** demonstrates the results of the electrochemical evaluation of all blended electrodes using coin-type Li half-cells (2032R) at 24 °C. As presented in **Figure 3. 3a, b**, the G/SGC achieves the highest first-cycle CE of 91.6% with a stable capacity retention of 97.2% after 100 cycles. G/C-SiO_x and G/Si-G/C show first-cycle CEs of 89.3% and 91.0% CEs with capacity retentions of 84.2% and 92.6% after 100 cycles, respectively. Although G/C-SiO_x and G/Si-G/C show somewhat low first-cycle CEs and decreased capacity retentions, their electrochemical performances are substantially enhanced via graphite blending compared to the non-blended materials. **Figure 3. 3c** shows the cycling CE for each blended electrode, depicting the reversible capacity per cycle. Both G/SGC and G/Si-G/C show a rapid increase in cycling CE, exceeding 99.5% after only three cycles, and sustain the efficiency for the subsequent cycles. Notably, G/SGC exhibits slightly higher average cycling CE for 100 cycles (99.92%) than that of G/Si-G/C (99.88%). However, G/C-SiO_x shows delayed increases in cycling CE, only exceeding 99.5% after seven cycles with the lowest average cycling CE for 100 cycles (99.81%). The cycling CE generally represents the actual Li consumptions of the counter electrode during electrochemical cycling.^{7, 32, 33} Therefore, the cycling CE in the half-cell is critical for accurately estimating the capacity retention of the full-cell system, where the amount of Li⁺ is limited. **Figure 3. 3d-f** plot the voltage profiles of the G/C-SiO_x, G/Si-G/C, and G/SGC electrodes corresponding to the above cycling tests, respectively.

To investigate the commercial viability, the prototype full-cells using the individual graphite-blended samples as anodes were assembled to evaluate the battery performances in the potential range of 2.7–4.35 V at 24 °C. Especially, we adopted the surface modified lithium cobalt oxide (LCO) which aimed at excellent stability with an additional capacity at high-voltages (>4.3 V vs Li). With this state-of-the-art high-voltage cathode, the samples can be evaluated under higher energy density condition. As a demonstration of the adequateness for the standard cathode, the galvanostatic voltage profiles and cycling plots of the high-voltage LCO are presented in **Figure 3. 4**. In **Figure 3. 5a**, we show that G/SGC exhibits the highest first-cycle CE of 89.7% in the full-cell, whereas the G/Si-G/C and G/C-SiO_x show relatively low first-cycle CEs of 88.0% and 85.9%, respectively. High first-cycle CEs are regarded as important factors in the performance of a Li-finite full-cell system, because the CE directly

affects the usable capacity of the practicably manufactured cell. At this point, G/SGC shows a cell capacity 4.4% higher, at 3.07 mAh/cm², than that of G/C-SiO_x (2.94 mAh/cm²) after the first formation cycle. Under the discharge rate of 1C, **Figure 3. 5b** demonstrates the prolonged cycling performance of each individual full cell for 400 cycles. In the case of G/SGC, it exhibits 67.1% capacity retention after 400 cycles, whereas G/Si-G/C and G/C-SiO_x show lower capacity retentions of 55.1% and 63.3%, respectively. To interpret the results of the cycling behavior, rescaled plots of reversible capacity as a function of cycle number and cycling CE are provided in the **Figure 3. 5b inset** and **Figure 3. 5c**, respectively. As shown in **Figure 3. 5c**, the initial CEs, which are below 99.5% during the first and subsequent several cycles, generally lead to dramatic capacity degradation in the cells. In this regard, G/C-SiO_x and G/Si-G/C show poor and delayed increases in initial CE (< 99.5%) for the first 22 cycles, followed by dramatic capacity fading. Meanwhile, G/SGC exhibits high initial CE, with a rapid increase to exceed 99.5% in only four cycles, and experiences less capacity loss during the initial cycles. After all electrodes achieved cycling CEs exceeding 99.5%, the slope indicating the degree of capacity deterioration is considered to be gentle as stable cycling behavior is retained, as shown in inset of **Figure 3. 5b**. Furthermore, the average efficiency of each full cell is recorded as 99.64%, 99.58%, and 99.51% for G/SGC, G/C-SiO_x, and G/Si-G/C, respectively, when calculated from the results of the first 100 cycles (**Fig. 3. 5c**). To this end, even though the differences in the average efficiencies are extremely small, the CE eventually affects the long-term cycle life of each individual full cell, as in **Figure 3b**.¹⁵ In addition, **Figure 3. 5d-f** plot the voltage profiles of the full cells for G/C-SiO_x, G/Si-G/C, and G/SGC, respectively. Interestingly, for G/SGC, most of the capacity (3.1 mAh/cm²) is charged in the constant current (CC) section during the charging process, which is divided into the CC and constant voltage (CV) modes. This result implies that G/SGC shows the lowest overpotential in the full cell under a current density of 1.7 mA/cm², compared to the G/C-SiO_x and G/Si-G/C full-cells.

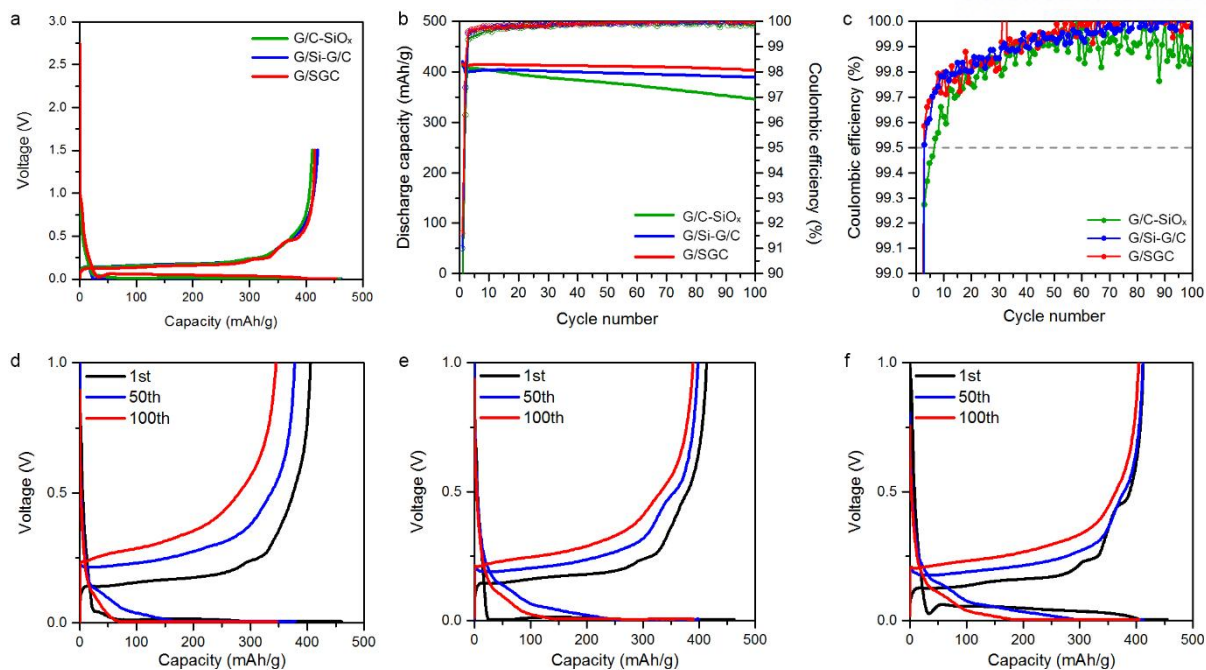


Figure 3. 3. Electrochemical evaluations of G/C-SiO_x, G/Si-G/C, and G/SGC in half-cell. a) Voltage profiles at the first cycle, corresponding to the battery formation process. b) Discharge capacities and CEs of the anodes cycled at 0.5C for 100 cycles. c) Rescaled form of CE at each cycle from 99 to 100%. d-f) Various voltage profiles of (d) G/C-SiO_x, (e) G/Si-G/C, and (f) G/SGC at the first, fiftieth, and hundredth cycle.

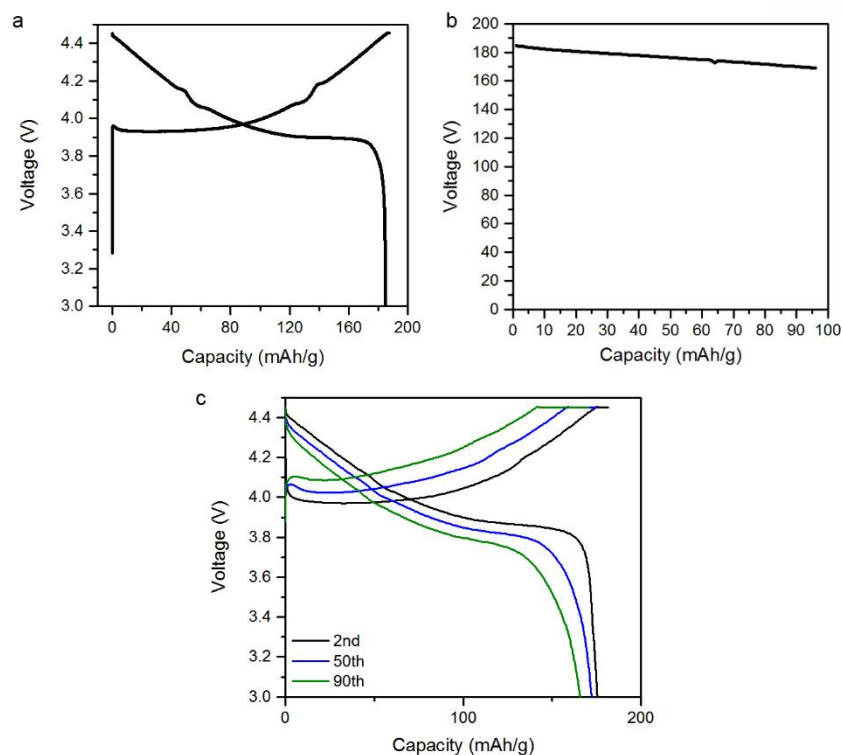


Figure 3. 4. Electrochemical performances of high-voltage LCO in half-cell. a) Voltage profile at the first cycle. b) Cycling performances at the charge/discharge rate of 0.5C. c) Voltage profiles at second, fiftieth, and ninetieth cycle. The surface modified LCO was used to improve structural stability even beyond 4.45 V. It showed high reversible specific capacity of 183 mAh/g with first cycle CE of 97.9% and capacity retention of 92.1% at ninetieth cycle in the voltage range of 4.45-3 V.

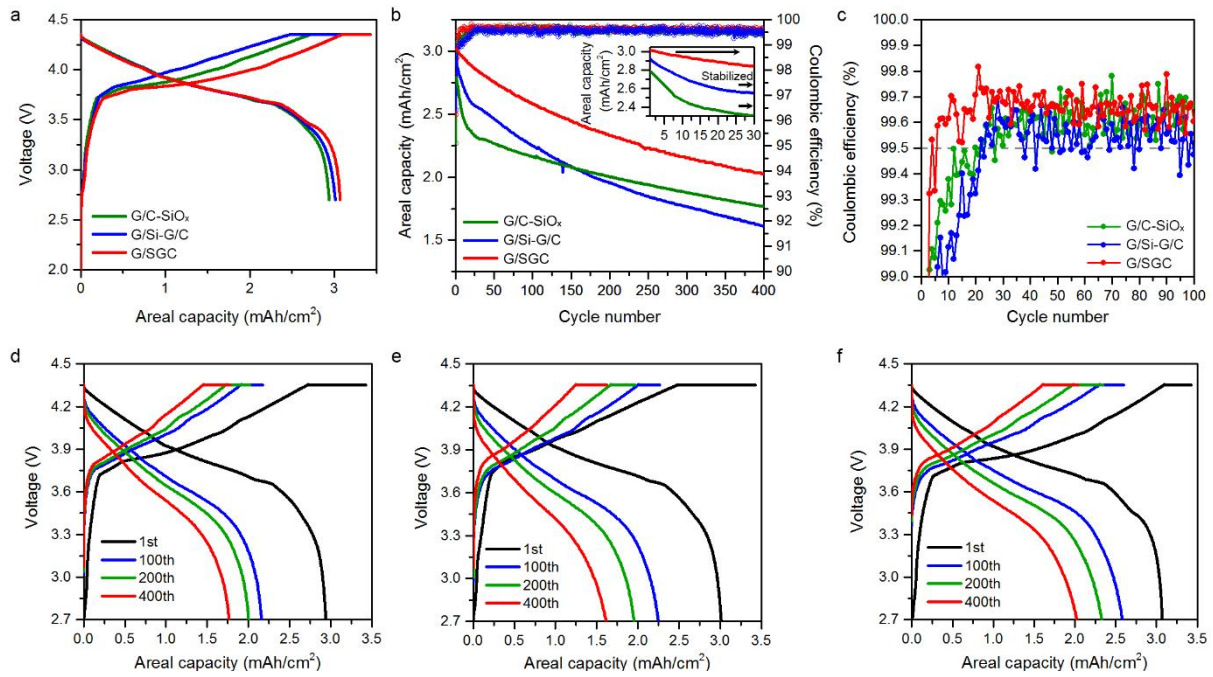


Figure 3. 5. Electrochemical performances of G/C-SiO_x, G/Si-G/C, and G/SGC in the prototype full-cell high-energy-density batteries. a) Voltage profiles of the prototype full cells at the first formation cycle. b) Cycling performances at the charge/discharge rate of 0.5C with CE plots for 400 cycles. Inset shows magnified areal capacity versus cycle number plotted for the early cycles. c) Rescaled form of CE at each cycle from 99 to 100% for 100 cycles. d-f) Voltage profiles of the prototype full cells at the first, hundredth, two-hundredth, and four-hundredth cycle.

3. 3. 4. Volume expansion testing of fabricated electrodes

In order to elucidate the causes for the different battery performances of G/C-SiO_x, G-Si-G/C, and G/SGC, we investigated the macroscopic aspects of the electrode volume expansion (**Fig. 3. 6**) and the microstructural changes of the materials (**Fig. 3. 7**) before and after cycling in the full-cell configuration by using SEM with EDS mapping analysis and TEM analysis. Generally, battery failure with Si electrodes has been attributed to the severe volume expansion of Si, which causes material breakdown, electrical contact loss from the current collector, and continuously accumulated solid–electrolyte interface (SEI) products.^{13, 34} In morphological studies, the volume expansion of Si detrimentally rearranges the electrode components, even deforming the surface morphology of the electrode and increasing the electrode thickness, which both imply the failure mechanisms of Si electrodes.³⁵⁻³⁷ **Figure 3. 6** shows the surface morphology variation and changes in electrode thickness change before and after 400 cycles, where the pristine electrode is prepared with high areal capacity (3.4 mAh/cm²) and high electrode density (1.6 g/cc). For accurate analyses, all electrodes were disassembled in the lithiated state after 400 cycles and rinsed with dimethyl carbonate (DMC) in an Ar-filled glove box.

As presented in **Figure 3. 6a-d**, the G/C-SiO_x electrode shows a volume expansion of 61% after 400 cycles, and the cross-sectional image in **Figure 3. 6d** depicts inter-particle cleavage within the electrode, as indicated by arrows. In fact, SiO_x generally exhibits a larger volume expansion of approximately 200% through Li alloying, and conventional graphite expands by approximately 15% in volume through the Li intercalation mechanism.^{1, 15, 38, 39} Moreover, the included oxygen in SiO_x is known to create unfavorable irreversible products (Li₂O and Li₄SiO₄) and promote poor initial CEs.^{22, 40} For this reason, the large difference in volume variation between C-SiO_x and conventional graphite, even with the irreversible products, forms localized cracks within the electrode and causes loss of electrical contact with relatively high capacity fading.

The G/Si-G/C electrode shown in **Figure 3. 6e-h** indicates the highest thickness increase of 85% accompanied with particle delamination from the electrode surface (**Fig. 3. 6g**). In addition, the cross-sectional electrode image in **Figure 3. 6h** depicts the formation of a large amount of pulverized powders within the electrode, unlike the pristine electrode shown in **Figure 3. 6f**. As such, the drastic electrode volume change crucially causes mechanical fracture of the electrode, thereby destroying the electrical network and deteriorating the battery performance.

The G/SGC electrode, as shown in **Figure 3. 6i-l**, exhibits 42% thickness increase after 400 cycles, with no sign of damage on the electrode surface (**Fig. 3. 6k**). The electrode preserves interconnectivity among components after cycling, as shown in the cross-sectional electrode image (**Fig. 3. 6l**). This implies that the G/SGC electrode sufficiently accommodates electrode volume expansion while retaining integrity after long-term cycling, thereby improving battery performance compared to the

other benchmarking samples. In addition, **Figure 3. 6m** briefly indexes the volume expansion of each electrode as a function of the cycle number, showing that the degree of electrode volume expansion closely follows the capacity fading of each individual full cell as in **Figure 3. 5b**.

From the measurement of electrode volume expansion, we estimate the volumetric energy densities for the prototype full cells of the G/SGC and benchmarking samples at the first and last cycles (**Fig. 3.6n**; detailed estimation is given in **Table 3. 2**). At the first cycle, mainly depending on the first-cycle CE, G/C-SiO_x, G/Si-G/C, and SGC exhibit energy densities of 619 Wh/L, 634 Wh/L, and 657 Wh/L, respectively. Interestingly, because of the synergy between low electrode volume expansion and high capacity retention, G/SGC exhibits the highest final volumetric energy density of 387 Wh/L compared to those of G/C-SiO_x and G/Si-G/C (317 Wh/L and 268 Wh/L). In this regard, we conclude that the electrode volume expansion is critical in determining the volumetric energy density of the full cell.

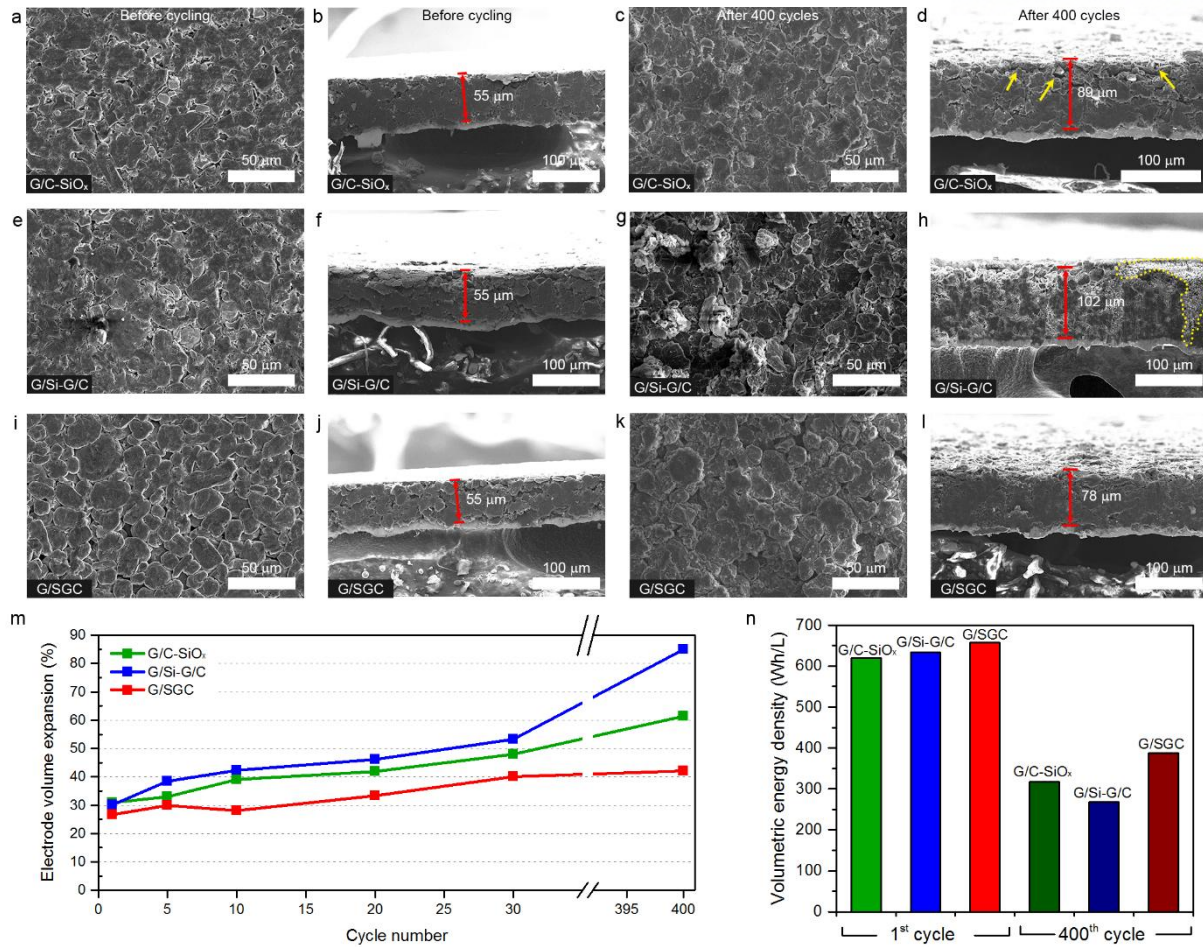


Figure 3. 6. Electrode volume expansion after cycling and estimation of volumetric energy density. a- l) SEM images of the electrodes composed of (a-d) G/C-SiO_x, (e-h) G/Si-G/C, and (i-l) G/SGC from top and cross-sectional views, describing the structural change of the electrodes before and after the cycling. m) *ex-situ* measurement of electrode volume expansion after cycling. n) Volumetric energy densities before and after 400 cycles.

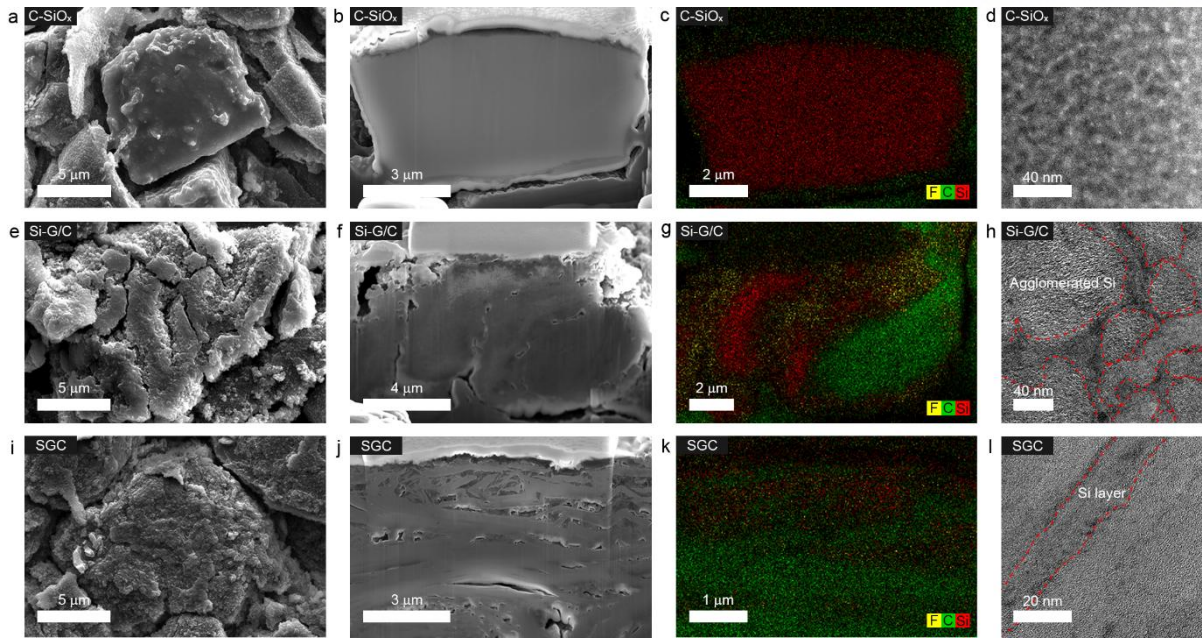


Figure 3. 7. Morphological changes of (a-d) SiO_x , (e-h) Si-G/C, and (i-l) SGC in the graphite-blended electrode after 400 cycles. a, e, i) SEM images of the Si composite on the electrodes cycled for 400 cycles. b, f, j) Cross-sectional images of SiO_x , Si-G/C, and SGC after 400 cycles with EDS mapping (c, g, k). F, C, and Si are indicated by yellow, green, and red, respectively. d, h, l) HR-TEM images at the interfacial region.

Volumetric energy density				
$\frac{(\text{Areal cell capacity}) \times (\text{Average voltage})}{(\text{Total thickness of cathode, anode and separator})}$				
Electrode information				
	Separator	Current collector (Cu)	Current collector (Al)	
Thickness (μm)	20	18	15	
Full-cell information				
	LCO	G/C-SiO _x	G/Si-G/C	G/SGC
1st cycle				
Areal capacity (mAh/cm ²)	-	2.94	3.01	3.07
Average voltage (V)	-	3.79	3.79	3.79
Thickness at fully-charged state (μm)	55 (fixed)	72	72	69
400th cycle				
Areal capacity (mAh/cm ²)	-	1.76	1.61	2.02
Average voltage (V)	-	3.55	3.50	3.56
Thickness at fully-charged state (μm)	55 (fixed)	89	102	78
Energy density estimation				
		G/C-SiO _x	G/Si-G/C	G/SGC
1 st cycle (Wh/L)		619	634	657
400 th cycle (Wh/L)		317	268	387

Table 3. 2. Volumetric energy density estimation

3. 3. 5. Characterization of SGC and benchmarking samples after electrochemical cycling

For a more detailed identification of the morphology changes in the particles after cycling, we inspected the C-SiO_x, Si-G/C, and SGC particles in each individual graphite-blended electrode with SEM, EDS, and TEM measurements, as shown in **Figure 3. 7**. Furthermore, we reveal the approximate amount of electrolyte decomposition by mapping F via EDS analysis. F can indicate the presence of the SEI layer because no F is used in the electrode components, including the active material, binder, and conducting agents, except for the Li salt and the additive in the electrolyte, i.e., LiPF₆ and fluorinated ethylene carbonate (FEC), respectively.^{20, 41} The images in **Figure 3. 7a-d** depict the C-SiO_x particles in the graphite-blended electrode after cycling. The SEM images show that C-SiO_x maintains structural stability without surface cracks (**Fig. 3. 7a**) or cracks inside the particle (**Fig. 3. 7b**). However, while the heterogeneous matrix effectively sustains its structural integrity after cycling, the large volume variation of C-SiO_x eventually creates a gap between adjacent particles measuring approximately 1 μm, as a proof of the loose electrical contact. EDS mapping shows that Si remains highly dispersed within the particle, and no F is found (**Fig. 3. 7c**). The bright-field TEM image in **Figure 3. 7d** clearly shows a mixture of lithium silicate phases^{40, 42} from repeated charging and discharging.

In the Si-G/C particle (**Fig. 3. 7e-h**), it clearly shows severe cracks after 400 cycles, as shown in **Figure 3. 7e**. Moreover, the cross-sectional SEM image (**Fig. 3. 7f**) shows that the inside of the particle is filled with accumulated unfavorable byproducts, a noticeable difference from the pristine particle before cycling, as seen in **Figure 3. 1i**. Through EDS mapping (**Fig. 3. 7g**) and TEM analysis (**Fig. 3. 7h**), we confirm that volume-expanded Si and significant SEI products are located inside the particle, where Si has become seriously aggregated relative to its initial morphology. Consequentially, the large volume expansion of the excessive Si in Si-G/C decisively caused severe particle fractures, and the electrolyte absorbed through these cracks continuously consumed Li⁺ by SEI accumulation, thereby deteriorating the battery performance.

Figure 3. 7i-l indicate the corresponding images of the SGC particles for SEM, EDS, and TEM measurement. Interestingly, while internal voids are reduced compared to those in the pristine particle (**Fig. 3. 1i**), no cracks are present on the surface (**Fig. 3. 7i**), and the overall structural stability is preserved without mechanical failure. As expected, the thin and homogeneous Si nanolayer effectively alleviates induced stress, and the sufficient void space within the SGC particle accommodates the Si volume expansion. Therefore, the particle retains structural integrity and minimizes the total volumetric change. By these means, it is clarified that a small amount of accumulated SEI products are observed in the particle by F mapping (**Fig. 3. 7k**), suggesting suppressed side reactions. Moreover, the TEM image in **Figure 3. 7l** shows that the Si nanolayer remains in contact with graphite and retains integrity without collapse or interlayer cleavage. The preservation of morphology effectively promotes lithium

transport along the carbon matrix. With these favorable features, we prove that SGC affords excellent compatibility with blended graphite particles, bringing good electrochemical performance compared to state-of-the-art benchmarking samples such as C-SiO_x and Si-G/C.

3. 4. Conclusion

To assess the commercial viability of SGC and state-of-the-art benchmarking samples of C-SiO_x and Si-G/C, we thoroughly investigated the detailed physical properties of each individual material and the electrochemical performances of graphite-blended electrodes using these materials. For a rational comparison, the specific reversible capacities of the graphite-blended electrodes were fixed at 420 mAh/g. In addition, the electrodes were fabricated using industrial electrode densities (> 1.6 g/cc), high areal capacity (> 3.0 mAh/cm²), and limited binder composition (3.0 wt%). Compared with the benchmarking samples, when blended with graphite, SGC exhibited better electrochemical performances in both half- and full-cell configurations (Summarized in **Table 3. 3**). In particular, G/SGC successfully achieved the highest first-cycle CE of 91.6% with a rapid increase of the cycling CE to exceed 99.5% after only three cycles in the half-cell, showing the stable capacity retention of 97.2% after 100 cycles. Furthermore, the prototype full-cell battery comprising high-voltage LCO and G/SGC also demonstrated the high first-cycle CE of 89.7% and a cell capacity approximately 4.4% higher (3.07 mAh/cm²) than that of G/C-SiO_x (2.94 mAh/cm²) at the first formation cycle. The full-cell battery with G/SGC showed stable cycling behavior with capacity retention of 67.1% after 400 cycles and the cycling CE exceeded 99.5% after only four cycles, creating the high average CE of 99.64%. The graphite-blended electrode with SGC completely overcame the deterioration arising from volume variation through structural integrity, and exhibited the lowest electrode thickness increase of 42% compared with its benchmarking sample counterparts (C-SiO_x; 61%, and Si-G/C; 85%), which led to a much higher volumetric energy density of 119 Wh/L greater than that of Si-G/C. In summary, the favorable features of SGC could afford good compatibility with blended graphite particles; G/SGC achieved better electrochemical performance and mechanical stability than graphite blended with state-of-the-art benchmarking samples. Even though the G/SGC full-cell battery showed gradual capacity fading upon cycling, we believe that this can be mitigated by surface treatments and electrolyte modifications. Overall, this rigorous benchmarking comparison under the test methods and criteria used in industrial battery manufacturing presents realistic guidelines and a comprehensive understanding of the implementation of Si anodes for battery researchers.

Sample	Only Si-based anodes		Si-Graphite blending anodes for 420 mAh/g		Full cell with Si-Graphite blending anodes and LCO				
	Specific reversible capacity	Initial CE (%)	Initial CE (%)	Capacity retention (% 100 th cycle)	Cell capacity (mAh/cm ²)	Initial CE (%)	400 th cycle		
							Cycle capacity (mAh/cm ²)	Capacity retention (%)	Electrode volume expansion (%)
C-SiO _x	1673	77.0	89.3	84.2	2.94	85.9	1.76	63.3	61
Si-G/C	681	84.8	91.0	92.6	3.01	88.0	1.61	55.1	85
SGC	520	92.0	91.6	97.2	3.07	89.7	2.02	67.1	42

Table 3. 3. Summarized electrochemical performances of C-SiO_x, Si-G/C, and SGC in half- and full-cell

3.5 References

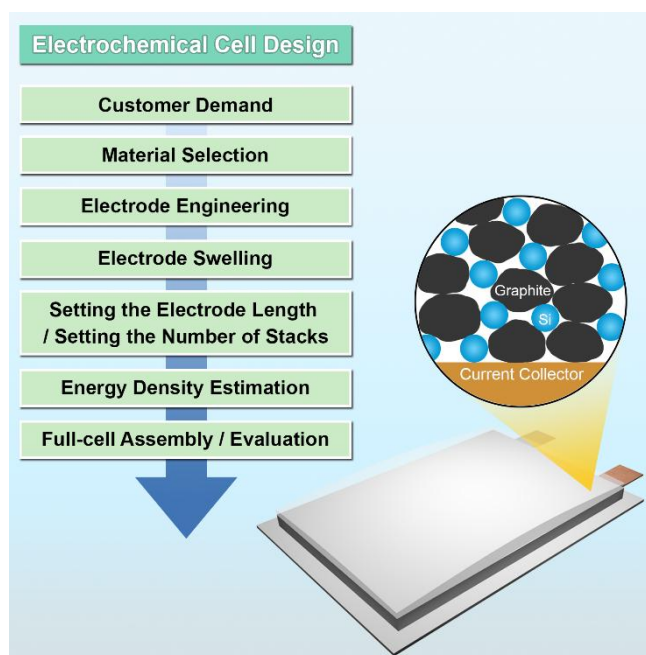
1. Jeong, G.; Kim, Y.-U.; Kim, H.; Kim, Y.-J.; Sohn, H.-J., Prospective materials and applications for Li secondary batteries. *Energ Environ Sci* **2011**, *4* (6), 1986-2002.
2. Crabtree, G.; Kocs, E.; Trahey, L., The energy-storage frontier: Lithium-ion batteries and beyond. *Mrs Bulletin* **2015**, *40* (12), 1067-1078.
3. Choi, N.-S.; Chen, Z.; Freunberger, S. A.; Ji, X.; Sun, Y.-K.; Amine, K.; Yushin, G.; Nazar, L. F.; Cho, J.; Bruce, P. G., Challenges Facing Lithium Batteries and Electrical Double-Layer Capacitors. *Angew Chem Int Edit* **2012**, *51* (40), 9994-10024.
4. Thackeray, M. M.; Wolverton, C.; Isaacs, E. D., Electrical energy storage for transportation-approaching the limits of, and going beyond, lithium-ion batteries. *Energ Environ Sci* **2012**, *5* (7), 7854-7863.
5. Goodenough, J. B., Evolution of Strategies for Modern Rechargeable Batteries. *Accounts of Chemical Research* **2013**, *46* (5), 1053-1061.
6. Rolison, D. R.; Nazar, L. F., Electrochemical energy storage to power the 21st century. *Mrs Bulletin* **2011**, *36* (7), 486-493.
7. Chevrier, V. L.; Liu, L.; Dinh Ba, L.; Lund, J.; Molla, B.; Reimer, K.; Krause, L. J.; Jensen, L. D.; Figgemeier, E.; Eberman, K. W., Evaluating Si-Based Materials for Li-Ion Batteries in Commercially Relevant Negative Electrodes. *J Electrochem Soc* **2014**, *161* (5), A783-A791.
8. Dash, R.; Pannala, S., Theoretical Limits of Energy Density in Silicon-Carbon Composite Anode Based Lithium Ion Batteries. *Scientific Reports* **2016**, *6*.
9. Dimov, N.; Xia, Y.; Yoshio, M., Practical silicon-based composite anodes for lithium-ion batteries: Fundamental and technological features. *J Power Sources* **2007**, *171* (2), 886-893.
10. Klett, M.; Gilbert, J. A.; Trask, S. E.; Polzin, B. J.; Jansen, A. N.; Dees, D. W.; Abraham, D. P., Electrode Behavior RE-Visited: Monitoring Potential Windows, Capacity Loss, and Impedance Changes in Li-1.03(Ni0.5Co0.2Mn0.3)(0.97)O-2/Silicon-Graphite Full Cells. *J Electrochem Soc* **2016**, *163* (6), A875-A887.
11. McDowell, M. T.; Lee, S. W.; Nix, W. D.; Cui, Y., 25th Anniversary Article: Understanding the Lithiation of Silicon and Other Alloying Anodes for Lithium-Ion Batteries. *Adv. Mater.* **2013**, *25* (36), 4966-4984.
12. Ko, M.; Oh, P.; Chae, S.; Cho, W.; Cho, J., Considering Critical Factors of Li-rich Cathode and Si Anode Materials for Practical Li-ion Cell Applications. *Small* **2015**, *11* (33), 4058-4073.
13. Wu, H.; Cui, Y., Designing nanostructured Si anodes for high energy lithium ion batteries. *Nano Today* **2012**, *7* (5), 414-429.
14. Du, Z.; Dunlap, R. A.; Obrovac, M. N., High Energy Density Calendered Si Alloy/Graphite Anodes. *J Electrochem Soc* **2014**, *161* (10), A1698-A1705.

15. Obrovac, M. N.; Chevrier, V. L., Alloy Negative Electrodes for Li-Ion Batteries. *Chemical Reviews* **2014**, *114* (23), 11444-11502.
16. Lee, J.-I.; Park, S., High-performance porous silicon monoxide anodes synthesized via metal-assisted chemical etching. *Nano Energy* **2013**, *2* (1), 146-152.
17. Song, J.-W.; Cao Cuong, N.; Song, S.-W., Stabilized cycling performance of silicon oxide anode in ionic liquid electrolyte for rechargeable lithium batteries. *Rsc Advances* **2012**, *2* (5), 2003-2009.
18. Suh, S. S.; Yoon, W. Y.; Kim, D. H.; Kwon, S. U.; Kim, J. H.; Kim, Y. U.; Jeong, C. U.; Chan, Y. Y.; Kang, S. H.; Lee, J. K., Electrochemical behavior of SiO_x anodes with variation of oxygen ratio for Li-ion batteries. *Electrochim Acta* **2014**, *148*, 111-117.
19. Yoon, Y. S.; Jee, S. H.; Lee, S. H.; Nam, S. C., Nano Si-coated graphite composite anode synthesized by semi-mass production ball milling for lithium secondary batteries. *Surface & Coatings Technology* **2011**, *206* (2-3), 553-558.
20. Lee, J.-H.; Kim, W.-J.; Kim, J.-Y.; Lim, S.-H.; Lee, S.-M., Spherical silicon/graphite/carbon composites as anode material for lithium-ion batteries. *J Power Sources* **2008**, *176* (1), 353-358.
21. Jo, Y. N.; Kim, Y.; Kim, J. S.; Song, J. H.; Kim, K. J.; Kwag, C. Y.; Lee, D. J.; Park, C. W.; Kim, Y. J., Si-graphite composites as anode materials for lithium secondary batteries. *J Power Sources* **2010**, *195* (18), 6031-6036.
22. Uono, H.; Kim, B.-C.; Fuse, T.; Ue, M.; Yamaki, J.-i., Optimized structure of silicon/carbon/graphite composites as an anode material for Li-ion batteries. *J Electrochem Soc* **2006**, *153* (9), A1708-A1713.
23. Wen, Z. S.; Yang, J.; Wang, B. F.; Wang, K.; Liu, Y., High capacity silicon/carbon composite anode materials for lithium ion batteries. *Electrochem. Commun.* **2003**, *5* (2), 165-168.
24. Lee, E. H.; Jeong, B. O.; Jeong, S. H.; Kim, T. J.; Kim, Y. S.; Jung, Y., Effect of Carbon Matrix on Electrochemical Performance of Si/C Composites for Use in Anodes of Lithium Secondary Batteries. *B Korean Chem Soc* **2013**, *34* (5), 1435-1440.
25. Ko, M.; Chae, S.; Ma, J.; Kim, N.; Lee, H.-W.; Cui, Y.; Cho, J., Scalable synthesis of silicon-nanolayer-embedded graphite for high-energy lithium-ion batteries. *Nature Energy* **2016**, *1*.
26. Chae, S.; Ko, M.; Park, S.; Kim, N.; Ma, J.; Cho, J., Micron-sized Fe-Cu-Si ternary composite anodes for high energy Li-ion batteries. *Energ Environ Sci* **2016**, *9* (4), 1251-1257.
27. Atiemo-Obeng, V. A.; Penney, W. R.; Armenante, P.; Hand-book of Industrial Mixing, John Wiley&Sons, INC., **2004**; pp 543-584.
28. Gulbinska, M. K.; Lithium-ion Battery Materials and Engineering: Current Topics and Problems from the Manufacturing Perspective, Springer, **2014**

29. Park, C.-M.; Choi, W.; Hwa, Y.; Kim, J.-H.; Jeong, G.; Sohn, H.-J., Characterizations and electrochemical behaviors of disproportionated SiO and its composite for rechargeable Li-ion batteries. *J Mater Chem* **2010**, *20* (23), 4854-4860.
30. Dimov, N.; Fukuda, K.; Umeno, T.; Kugino, S.; Yoshio, M., Characterization of carbon-coated silicon - Structural evolution and possible limitations. *J Power Sources* **2003**, *114* (1), 88-95.
31. Xu, Q.; Li, J.-Y.; Sun, J.-K.; Yin, Y.-X.; Wan, L.-J.; Guo, Y.-G., Watermelon-Inspired Si/C Microspheres with Hierarchical Buffer Structures for Densely Compacted Lithium-Ion Battery Anodes. *Adv. Energy Mater.* **2017**, *7* (3).
32. Wu, H.; Chan, G.; Choi, J. W.; Ryu, I.; Yao, Y.; McDowell, M. T.; Lee, S. W.; Jackson, A.; Yang, Y.; Hu, L.; Cui, Y., Stable cycling of double-walled silicon nanotube battery anodes through solid-electrolyte interphase control. *Nat Nanotechnol* **2012**, *7* (5), 309-314.
33. Ko, M.; Chae, S.; Cho, J., Challenges in Accommodating Volume Change of Si Anodes for Li-Ion Batteries. *Chemelectrochem* **2015**, *2* (11), 1645-1651.
34. Yi, R.; Dai, F.; Gordin, M. L.; Chen, S.; Wang, D., Micro-sized Si-C Composite with Interconnected Nanoscale Building Blocks as High-Performance Anodes for Practical Application in Lithium-Ion Batteries. *Adv. Energy Mater.* **2013**, *3* (3), 295-300.
35. Han, Z.-J.; Yabuuchi, N.; Shimomura, K.; Murase, M.; Yui, H.; Komaba, S., High-capacity Si-graphite composite electrodes with a self-formed porous structure by a partially neutralized polyacrylate for Li-ion batteries. *Energ Environ Sci* **2012**, *5* (10), 9014-9020.
36. Yoshio, M.; Kugino, S.; Dimov, N., Electrochemical behaviors of silicon based anode material. *J Power Sources* **2006**, *153* (2), 375-379.
37. Zhang, W.-J., A review of the electrochemical performance of alloy anodes for lithium-ion batteries. *J Power Sources* **2011**, *196* (1), 13-24.
38. Park, C.-M.; Kim, J.-H.; Kim, H.; Sohn, H.-J., Li-alloy based anode materials for Li secondary batteries. *Chem Soc Rev* **2010**, *39* (8), 3115-3141.
39. Miyachi, M.; Yamamoto, H.; Kawai, H.; Ohta, T.; Shirakata, M., Analysis of SiO anodes for lithium-ion batteries. *J Electrochem Soc* **2005**, *152* (10), A2089-A2091.
40. Nie, M.; Abraham, D. P.; Chen, Y.; Bose, A.; Lucht, B. L., Silicon Solid Electrolyte Interphase (SEI) of Lithium Ion Battery Characterized by Microscopy and Spectroscopy. *J Phys Chem C* **2013**, *117* (26), 13403-13412.
41. Yu, B.-C.; Hwa, Y.; Park, C.-M.; Sohn, H.-J., Reaction mechanism and enhancement of cyclability of SiO anodes by surface etching with NaOH for Li-ion batteries. *J Mater Chem A* **2013**, *1* (15), 4820-4825.

Chapter 4

Confronting Issues of the Practical Implementation of Si Anode in High-energy Lithium-ion Batteries



Over twenty years, Si has been investigated as a promising alternative to conventional graphite because of its high specific capacity and proper working voltage. As numerous strategies have demonstrated their improved electrochemical properties with addressing the intrinsic challenges of Si anode, the practical investigation with a full-cell has been regarded as an important task to verify their feasibilities. In this Perspective, we discuss key issues in the practical implementation of the Si anode in the high-energy full-cell. With the target of the improvement in the volumetric energy density, the comprehensive overview of an electrochemical cell design for Si anodes is presented with its influence on electrochemical properties. Moreover, we highlight the electrode swelling issues and the capacity fading of the Si anode which is pronounced in the full-cell rather than in the half-cell. Finally, we offer insights regarding the potential future directions in the development of the Si anode for high-energy lithium-ion batteries.

This chapter has been published.

Reproduced with permission from Chae, S.; Ko, M.; Kim, K.; Ahn, K.; Cho, J., Confronting issues of the practical implementation of Si anode in high-energy lithium-ion batteries. *Joule* **2017**, *1* (1), 47-60.

4.1 Introduction

In accordance with increasing energy demands, the development of high-tech electrical gadgets and electric vehicles has required the smaller, lighter and longer lasting power supplier^{1,2}. Lithium-ion battery (LIB) has played an important role as energy storage devices in a broad range of applications, however the limit of available energy densities in LIBs urges the battery researchers to achieve a significant breakthrough via substituting the current electrode materials with high capacity electrode materials³⁻⁵. In this regard, among a variety of emerging anode materials for substituting the conventional graphite, Si has been considered as the most outstanding candidate with ten times gravimetric capacity of graphite^{6,7}, low working voltage⁸, and low price⁹. However, in contrast to these distinguished features, Si has intrinsic hurdles for the commercial anode, which are the huge volume change of maximum 400% while (de)alloying with lithium^{10,11} and its low electrical conductivity of $\sim 10^{-3}$ S/m (**Fig. 4. 1a**)¹². During the electrochemical lithiation, lithiation-induced expansion dominantly occurs at the phase boundary between Li-rich Li_xSi and Si ^{10,13}. This phase boundary is responsible for stress intensification and anisotropic swelling. While the stress generation is different with the size and phase of Si, the repeated volume changes eventually cause the mechanical fracture and pulverization, where the critical particle sizes for fracture are 150 nm for crystalline Si and 870 nm for amorphous Si ^{10,14}. This mechanical fracture and pulverization considerably make the loss of active material^{15,16}. In addition, the formation of the solid electrolyte interphase (SEI) layer on Si is unstable and the SEI layer grows continuously as a result of the dynamic volume change during cycling^{17,18}. This persistent side reaction with the electrolyte consumes the lithium ion and the solvent parasitically, as well as accumulating the SEI layer with increasing the internal resistance. Furthermore, the increased resistance and the rearrangement of active materials in the electrode lead to the electrical isolation of active materials from the current collector^{19,20}. Aside from the influence of the huge volume change, the electrochemical reversibility for Li-Si (de)alloying may be even not perfect because lithium can be trapped in the defect sites during the complicated structural transformation of Si ^{10,21}.

Ever since the advent of the Si anode, numerous strategies have been presented to overcome these challenges and make the best use of the Si anode²²⁻²⁷. The representatives are summarized in **Figure 4. 1c**. Although these strategies have truly succeeded in improving the electrochemical properties of Si anodes in a half-cell, their practical investigation with a full-cell is still insufficient to verify the feasibility^{28,29}. The main purpose of adopting Si is obviously to obtain the higher volumetric energy density than graphite^{30,31}. Accordingly, some of recent articles have emphasized the implementation of the Si anode in the full-cell and the consideration for the volumetric energy density^{32,33}. However, it is demanding work to develop the Si anode that has competent battery performances concurrently with higher volumetric energy density. In retrospect, as extensive efforts have been devoted to utilize the

carbonaceous anode, the commercial graphite has become admirable in every way, including the electrochemical property, the price, and the electrode manufacturing process³⁴⁻³⁶. Now that the considerable improvements in the Si anode have been achieved with various strategies, it is time to carry out comprehensive studies for the Si anode in the full-cell.

In this Perspective, we discuss the key factors for the implementation of the newly developed Si anodes in the practical full-cell. Based on the intrinsic property of Si and previous studies for conventional LIBs comprising of graphite, the major parameters for the electrochemical cell design are addressed in terms of the energy density. Particularly, considering the huge volume change of Si during cycling, the issue of electrode swelling is focused on with regard to its influence on energy density and the measurement method in the practical point of view. Moreover, we deal with the capacity fading of the Si anode in the full-cell which is less remarkable in the half-cell. In the final section, we propose the future directions for developing the Si anode toward higher volumetric energy density.

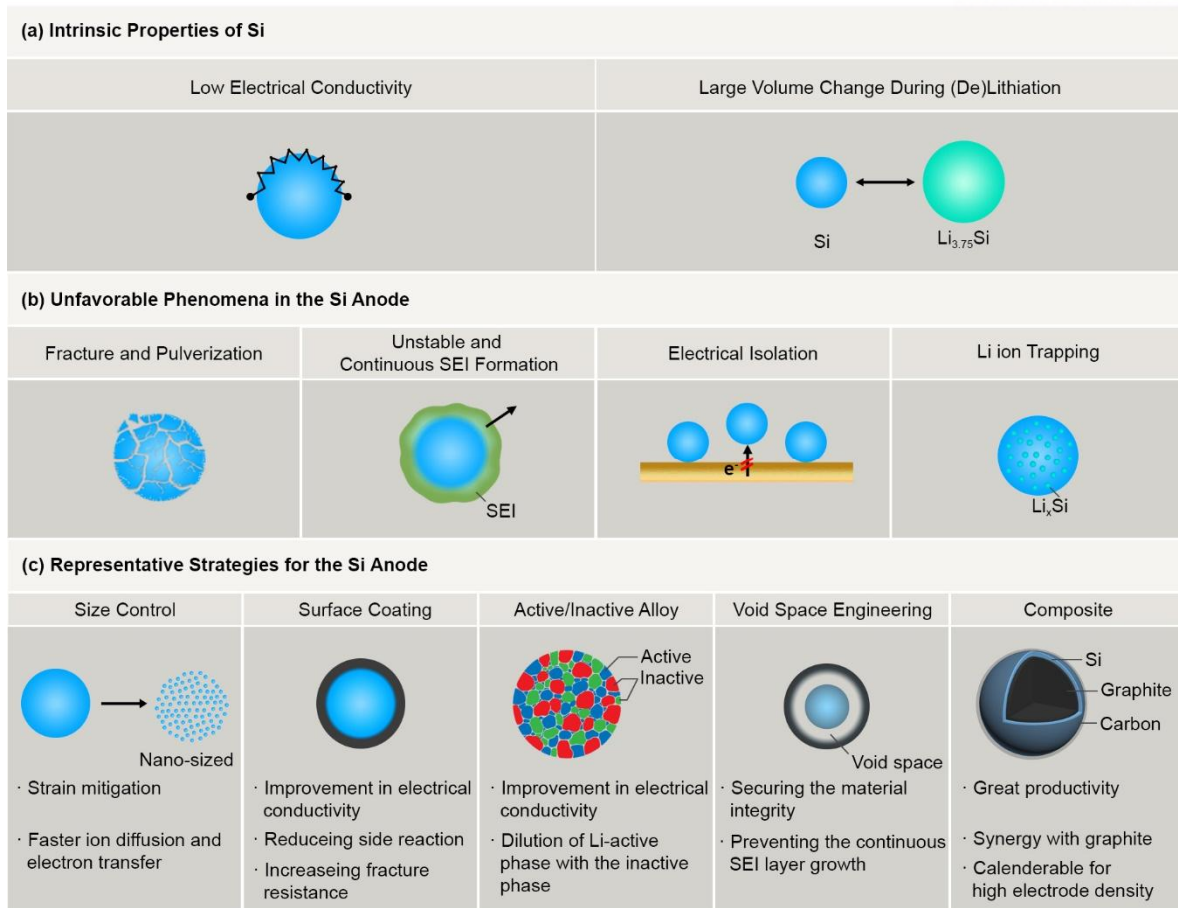


Figure 4. 1. Overview of the challenges and representative strategies associated with the Si anode. (a) Intrinsic properties of Si disadvantageous to charge transfer kinetics and to stable cycling behavior. (b) Unfavorable phenomena in the Si anode causing the active material loss and consumption of lithium ion in the cell. (c) Various representative strategies for addressing the unfavorable phenomena such as size control, surface coating, active/inactive alloy, void space engineering, and composite.

4.2 Result and discussion

Electrochemical cell design

To satisfy the specific requirements of different applications, commercial LIB cells have been manufactured with different electrochemical cell designs^{37,38}. For example, the mobile devices require the long lasting battery to secure the operation hours, so the high energy density is requisite in this battery. On the other hand, the power tools utilize a large amount of energy in short time, thus it requires the battery with high power density. In order to focus on the preferred electrochemical properties, the electrochemical cell design is customized with several parameters, such as material selection, electrode composition, areal capacity, negative electrode capacity/positive electrode capacity (N/P) ratio, electrode density, and so on. Definitely, maximizing all the electrochemical properties is ideal for a battery, however there is a trade-off between the energy and power densities in the electrochemical cell design³⁹. Therefore, when developing the active materials and evaluating the cell, we should recognize the influence of electrochemical cell design on the battery performances and should determine which electrochemical properties have a priority.

In this regard, before the practical implementation of the Si anode in the full-cell, the consideration about the electrochemical cell design is essential as in conventional LIBs. Unfortunately, most of previous studies presented only the gravimetric capacity with initial Coulombic efficiency (CE) and focused on improving the cycling performance without considering the electrochemical cell design and even the main purpose of the Si anode, i.e. higher energy density than that with graphite^{27,33}. Consequently, it has been difficult to compare their performances with each other based on several parameters of the electrochemical cell design and to prove the feasibility of their own Si anodes for commercial LIBs.

For the sake of exploring the electrochemical cell design of the Si anode, we classified the parameters into two categories: material and electrode engineering. The flow chart of electrochemical cell design is demonstrated in **Figure 4. 2**. The material indicates what we utilize as an active material, a binder and a conductive agent, involving the parameters such as specific (dis)charge capacity, initial CE, and average voltage. As is well known, the specific (dis)charge capacity is the total amount of charge in unit mass, which can be measured in half-cell test. When the areal capacity and electrode density are set, the specific capacity determines the loading level, i.e. the mass loading per unit area, and electrode thickness, contributing to the gravimetric and volumetric energy density. Generally, the Si anode has lower loading level than that of graphite at the same areal capacity owing to its superior specific capacity, thus it has a merit in gravimetric energy density. Meanwhile, it seems to be far too soon to judge the volumetric energy density because the electrode swelling is not yet considered. The initial CE, which

is estimated by dividing the initial discharge capacity by initial charge capacity, is an important indicator for the reversibility of the electrochemical reaction. Here, for the sake of avoiding the confusion of terminology, we inform that the charge and discharge means the lithiation and delithiation of anodes, respectively. While the side reactions such as SEI layer formation mainly occur at the initial cycle in commercial graphite, the Si anode can accompany continuous side reactions because of huge volume changes during cycling^{17,18}. It gives rise to capacity loss and hinders the stabilization of following CEs. Thus, especially for the Si anode, the cycling CEs up to stabilization is worthwhile to be traced for predicting the usable capacity^{29,40,41}. The average voltage, specifically during the discharging, is one of the most important parameters which considerably contribute to the energy density in the full-cell. Before conducting the full-cell test, the approximate average voltage of the full-cell can be estimated by subtracting the average voltage of anode from that of cathode³³. Indeed, the Si anode has slightly higher average voltage versus Li^+/Li than that of graphite, thus it can be disadvantageous to energy density.

The electrode engineering has significant influence on electrochemical properties. The manufacturing process of the electrode including mixing, coating and calendaring brings about the controllable parameters such as areal capacity, electrode composition, and electrode density. In the majority of Si anode studies, in order to demonstrate the stable cycling of Si anodes in half-cell, the electrode has been frequently designed with the low areal capacity, excessive use of binders and conductive agents and low electrode density. Enough conductive agents and binders can prevent the electrical isolation and delamination of active materials from the huge volume changes of Si anodes during cycling. However, in the case of those electrodes with low areal capacity, the true energy density is low because of high volume and weight fraction of other cell components such as the current collector, the separator and the cell package⁴². Besides, indiscriminately increasing the component ratios of the conductive agent and binder lowers the energy density. Overusing binders and carbonaceous conductive agents also bring about an increase in the electrical resistance and large amounts of side reactions because of their large specific area, respectively^{43,44}. Finally, the low electrode density of the uncalendered electrode significantly lowers the volumetric energy density with a large fraction of void spaces in the electrode. Hence, in order to realize the high energy density with the Si anode, the areal capacity, the electrode composition, and the electrode density need to be properly optimized, and the electrochemical properties should be characterized in this condition³⁷.

For the electrode with high areal capacity, which could realize the high energy density, the total amount of electrochemical reactions per unit area is larger than that with low areal capacity at the same C-rate, and so is the amount of unfavorable side reactions^{37,38}. As a result, a lot of byproducts seriously increase the interfacial overpotential. Besides, the electrode with high areal capacity is inevitably thicker than

the electrode with low areal capacity. The thick electrode limits the lithium ion transport by prolongation of diffusion pathway of lithium ion⁴⁵. Because of limited mass transport in thick electrode, lithium plating can occur in the regions of the anode close to the separator^{46,47}. More importantly, the thick electrode is apparently vulnerable to the damage from repeated volume changes which result in the electrode-level cracking and failure⁴⁸. Meanwhile, it is noted that the ceiling of areal capacity is set from the cathode, whose the thickness is limited by kinetic factors, with considering the N/P ratio in the full-cell⁴⁹.

In order to achieve high electrode density, the electrode is calendared under high pressures, leading to the increase in the volume fraction of active materials. From the electrode density, the initial porosity of electrode can be estimated with the electrode composition and the density of each individual component³⁸. Notably, the porosity affects the capacity fading mechanism of the anode across the board, including SEI layer side reaction, lithium plating side reaction, and mechanical degradation due to charging induced stress⁵⁰. Thus, the optimization of electrode density is needed to achieve both high energy density and competent electrochemical properties. However, the comprehensive studies for the impact of electrode density is not vigorous for the Si anode. It is because the brittleness and hardness of Si make the calendaring process tough. Furthermore, a lot of approaches for Si anodes with the material design, especially with the void space, can be easily damaged and be deformed into unintended morphology. However, without densification of the electrode, the energy density with the Si anode is inferior to commercial graphite anodes which have suffered densification. In this regard, as a feasible technique for improving the volumetric energy density with the densified Si anode, blending Si with proper amounts of graphite during slurry mixing process has been suggested, where the graphite plays roles as a lubricant, a conductive additive, and an active material^{29,31}.

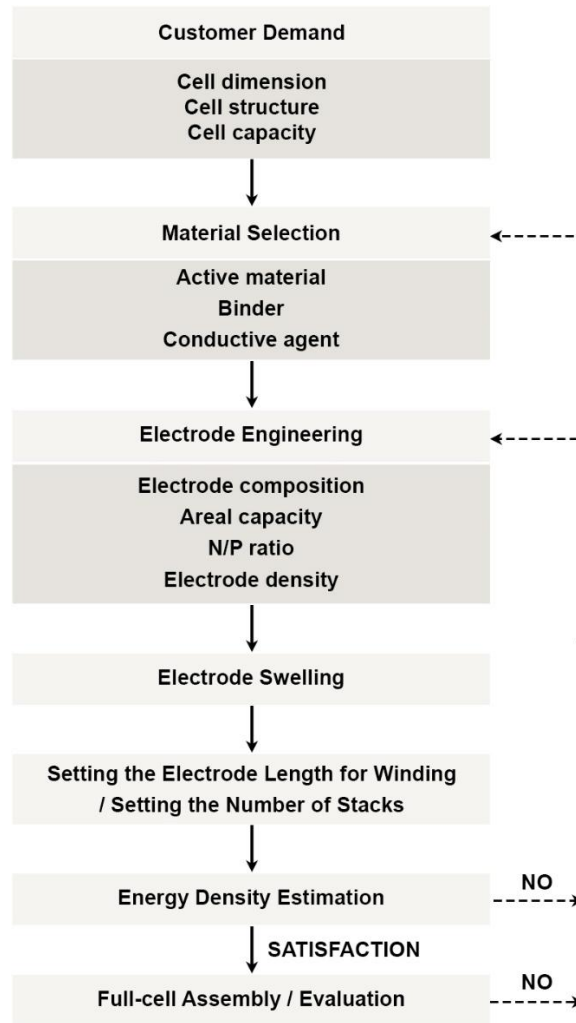


Figure 4. 2. Flow chart of the electrochemical cell design. The brief procedure of the electrochemical cell design is presented from the customer demand, such as cell dimension and structure, to the full-cell assembly/evaluation.

Electrode swelling

When it comes to the volumetric energy density, the electrode swelling during cycling is one of the most important factors to be mainly addressed. Ideally, the maximum energy density of the Si anode is realized when its porosity becomes 0% at the fully-lithiated state. Considering that the volume expansion of Si as 270% and ideal packing density of the face-centered-cubic (FCC) stacking, at least 80% of initial porosity is required to prevent the volume change of the electrode during lithiation/delithiation⁵¹. However, this ideal electrode does not include the binder and conductive agent, which imposes several practical limitations including poor manufacturability, low electrical conductivity and retention of mechanical integrity after repeated cycling. Furthermore, the actual electrode has a highly complicated structure with the active material, binder and conductive agent, such as pore size, pore distribution, and diverse particle sizes. Therefore, the comprehensive studies are necessary for predicting practical electrode swelling in the cell and the actual measurement of the electrode swelling is essential.

Here, we adopt the imaginary graphite-blended Si anodes as proper and practical examples to describe several parameters affecting the electrode swelling. The graphite-blended Si anode can have various specific capacities proportional to the blending ratio of graphite and Si. Considering the practical limit of Si anodes, the graphite-blended Si anode has been recognized as a feasible strategy for practically improving volumetric energy density, where the graphite can make up for the drawbacks of the Si anode. The graphite in the blended anode enables the densification of electrode with high electrical conductivity and mitigating the volume expansion as lowering the utilization ratio of Si in the electrode.

In order to investigate the influence of electrode swelling on volumetric energy density, we estimated the energy density depending on the electrode swelling of the graphite-blended Si anode at an interval of 5% of electrode swelling according to the flow chart of electrochemical cell design. The specific capacity of graphite-blended Si anode is set as 520 mAh/g. High-voltage lithium cobalt oxide (HVLCO) was adopted as the state-of-the-art cathode material. Detailed electrochemical cell design including requisite information and assumption is described as follows.

Customer Demand				
Cell dimension (W*L*H)		70 mm*90 mm*2.5 (max) mm		
Jelly roll dimension (W*L*H)		54 mm*81 mm*2.2 (max) mm		
		Cathode (W*L)	50 mm*68.5 mm	
		Anode (W*L)	54 mm*72.5 mm	
Cell structure		Stacking type pouch cell		
Cell capacity		1.2 Ah		
Material selection				
		Cathode		Anode
Active material		High-voltage lithium cobalt oxide (HVLCO)	Specific capacity: 183 mAh/g	Graphite
			ICE: 98%	Graphite-blended Si
		ICE: 92%		
				Specific capacity: 520 mAh/g
				ICE: 92% (Fixed) ^[1]
Binder	Polyvinylidene fluoride (PVDF)		Styrene butadiene rubber (SBR) and carboxymethyl cellulose (CMC)	
Conductive agent	Carbon black		Carbon black	
Electrode engineering				
		Cathode		Anode
Electrode composition (Active material:Binder:Conductive agent)		94:3:3		96:2.5:1
Areal discharge capacity (mAh/cm ²)		3.32		3.34
N/P ratio		1.1 ^[2]		
Electrode density (g/cc)		4		1.6
Electrode swelling (%)				
		Cathode		Anode
		HVLCO	3	Graphite
				20
				Graphite-blended Si
				20~80
Number of stacks ^[3]				
		Cathode		Anode
HVLCO/Graphite		6		7
HVLCO/ Graphite-blended Si	20~45% Electrode swelling	7		8
	50~80% Electrode swelling	6		7

Table 4. 1. Detailed electrochemical cell designs for graphite and graphite-blended Si anodes

[1] The initial Coulombic efficiency of all the graphite-blended Si anodes are fixed as 92% for facile comparison.

[2] N/P ratio is set as the ratio of areal capacity of anode and usable capacity of the full-cell in unit area.

$$\text{N/P ratio} = \frac{\text{Areal capacity of anode}}{\text{Usable cell capacity}}$$

$$\text{Usable cell capacity [mAh/cm}^2\text{]} = \text{Charge capacity of cathode [mAh/cm}^2\text{]} - \text{Irreversible cell capacity [mAh/cm}^2\text{]}$$

Irreversible cell capacity is defined as either the irreversible capacity of the anode or the irreversible capacity of the cathode, whichever is larger. In the case of our electrochemical cell design, the irreversible cell capacity is equal to the irreversible capacity of anode.

[3] The stacking sequence of electrodes follows below.

DS anode | [DS cathode | DS anode |] DS cathode | DS anode

Where DS = double sided, | = separator and [] = repeatable unit

Estimation of Average Cell Voltage

$$\text{Average cell voltage} = V_{\text{cathode}} - V_{\text{anode}}$$

$$V_{\text{cathode}} = \text{Average voltage of cathode in the half-cell}$$

$$V_{\text{anode}} = \text{Average voltage of anode in the half-cell}$$

The average voltage of lithium cobalt oxide (LCO), which we adopted here, is 3.9 V (vs Li⁺/Li).

Average voltages of graphite and Si are 0.15 V (vs Li⁺/Li) and 0.4 V (vs Li⁺/Li), respectively.

Based on a capacity averaged linear combination of graphite and Si, the average voltage of the graphite-blended Si anode in the half-cell can be estimated. For example, the average voltage of the graphite-blended Si anode with 520 mAh/g can be estimated as follows:

$$V_{\text{anode}} = \frac{360}{520} \times 0.15 + \frac{160}{520} \times 0.4 \text{ (V)}$$

$$= 0.210 \text{ (V)}$$

Estimation of Volumetric Energy Density

Based on the electrochemical cell design, we estimated the volumetric energy densities of graphite and graphite-blended Si anodes as follows.

Cell capacity =

Usable cell capacity in unit area * Cathode area * 2 (for double-sided) * the number of stacks for cathode

$$\text{Volumetric energy density} = \frac{\text{Cell capacity} * \text{Average cell voltage}}{\text{Active area volume}}$$

$$\text{Active area volume}^{[1]} = 54 \text{ mm} * 81 \text{ mm} * \text{Cell thickness}$$

[1] Active area volume only includes the jelly roll and the packaging in z-axis with ignoring the margin of the packaging in order to ignore the arbitrary margin of the packaging.

In order to investigate the influence of electrode swelling, we make the areal capacity, the cell capacity, and the N/P ratio almost the same. The volumetric energy density varies as a function of the cell thickness, and cell thickness highly depends on the electrode swelling and the number of stacks. Therefore, the electrode swelling determines the volumetric energy density.

Herein, the stacking type pouch cell was adopted, and the cell dimension is set as 70 mm * 90 mm * 2.5 (max) mm for 1.2 Ah. The photographs of pouch-type cell are presented as an example in **Figure 4. 3**. The thickness of the cell is variable with the electrode swelling, however the swollen thickness cannot exceed 2.5 mm. Based on the volume of swollen cell, the volumetric energy density of the graphite-blended Si anode decreases as the electrode swelling increases (**Fig. 4. 4a**). When comparing the graphite-blended Si with commercial graphite, the graphite-blended Si anode can lose the merit of energy density as its electrode swelling become severe, where the electrode swelling exceeds 60%. It is noted that the volumetric energy density suddenly drops at 50% of electrode swelling with losing the number of stacks from 7 cathodes and 8 anodes to 6 cathodes and 7 anodes because of the limited dimension. The loss in the number of stack is indicated by the decrease in the cell thickness. In other words, losing the number of stacks results in the decrease in the cell capacity.

Typically, the electrode swelling strongly depends on the specific capacity of the anode due to the intrinsic property of anode materials^{33,52}. In terms of the volumetric energy density, the limits of electrode swelling for the graphite-blended Si anodes could be the points that the volumetric energy densities of graphite-blended Si anodes become the same with that of commercial graphite because of the electrode swelling. In the same manner of electrochemical cell design in **Figure 4. 4a**, we estimated the swelling points at an interval of 10 mAh/g of specific capacity of graphite-blended Si anodes, where the volumetric energy densities of graphite-blended Si anodes become same with that of graphite (**Fig. 4. 4b**). When the electrode swelling exceeds these points, the graphite-blended Si anodes with 1.6 g/cc of electrode density have no merit of high volumetric energy density. Meanwhile, the electrode swelling even under the limit can deteriorate the electrochemical properties in conventional cell by deforming the separator as blocking the pore and squeezing out the electrolyte⁵³. Besides, it raises a safety issue with bulging of the battery package⁵⁴⁻⁵⁶. Therefore, the extensive efforts to reduce the electrode swelling are required for the enhancement of volumetric energy density.

In this regard, the measurement of the electrode swelling is as important as characterizing the electrochemical properties. It is noted that the electrode swelling can be different, even though the same active materials are utilized. With the same active materials, the electrode swelling depends on how many active materials are contained and reacted with lithium in unit volume. Accordingly, the following parameters are explored: electrode composition, electrode density, state of charge (SOC), and N/P ratio; Obviously, the component ratio of the active material is proportional to the electrode swelling. If multiple active materials, which exhibit different swelling behavior, are utilized, then the ratio of these materials should also be considered. The initial electrode density is crucial in the electrode swelling because it determines the initial porosity as aforementioned. The porosity can represent the fraction of void space over the electrode for the volume expansion of active materials. As shown in **Figure 4. 4c**,

as an example of the commercial graphite anode, the electrode with 1.6 g/cc of electrode density has larger porosity than the electrode with 1.3 g/cc of electrode density as much as about 14%, which means that the electrode has more space for accommodating volume expansion of graphite. The true density of Si (2.328 g/cc) is not much different to that of graphite (2.267 g/cc), so we can figure out that Si anodes, including graphite-blended Si anodes, are in the similar situation with graphite when it comes to their initial porosity for volume expansion. Hence, without considering the electrode density or porosity, characterizing the electrode swelling loses its meaning. During the battery operation, the electrode swelling varies as a function of SOC, which is maximized at the fully charged state. Notably, from this characteristic, the anomalous electrode behavior such as electrolyte decomposition and lithium plating can be detected through confirming one-to-one correspondence between the electrochemical data and swelling behavior carefully^{57,58}. In terms of the full-cell, because the N/P ratio is generally larger than 1 in order to prevent the lithium plating⁵⁹, the anode materials is not fully used in the full-cell during the operation. Hence, the electrode swelling can be mitigated with the N/P ratio (> 1).

To measure the electrode swelling, the thickness change of the electrode has been observed because the direction of electrode swelling is mainly parallel with the direction of calendaring which is vertical to current collector. The thickness change can be measured in micro-scale with the micrometer or the microscope such as optical microscope and scanning electron microscope (SEM) (**Fig. 4. 4d**). The micrometer is obviously the simpler method than the microscope, whereas the microscope offers more detailed information with the morphological structure of the swollen electrode. Unfortunately, these methods require destructive sample preparation, thus a lot of samples are consumed to gauge continuously changing thickness during cycling. Besides, the cell should be carefully disassembled to keep the bending of the electrode and the self-discharge from the electrical short. In order to measure the thickness changing in real time, the electrochemical dilatometry has been suggested⁶⁰⁻⁶². Since the first report of electrochemical dilatometry with nonaqueous electrolytes in 1994⁶⁰, various electrodes including graphite, Sn, and Si have been measured⁶³⁻⁶⁶. Generally, the dilatometer is equipped with the linear gauge and constant load (or spring) as illustrated in **Figure 4. 4e**. The electrochemical dilatometry is suitable for measuring the electrode swelling due to the non-destructive testing and the identical condition for electrochemical evaluation with ordinary battery test. It is noted that the additional calibration can be done for accuracy with considering the cathode swelling because the electrode swelling is measured for both of cathode and anode together in the dilatometry⁵⁸.



Figure 4. 3. Photographs of the pouch-type full-cell with the cell capacity of 1.2 Ah. (a) Double-sided cathode and anode for stack type pouch cell. (b) Stacking type pouch cell with the dimension of 70 mm * 90 mm * 2.5 mm. (c) Cross sectional photograph of the pouch cell.

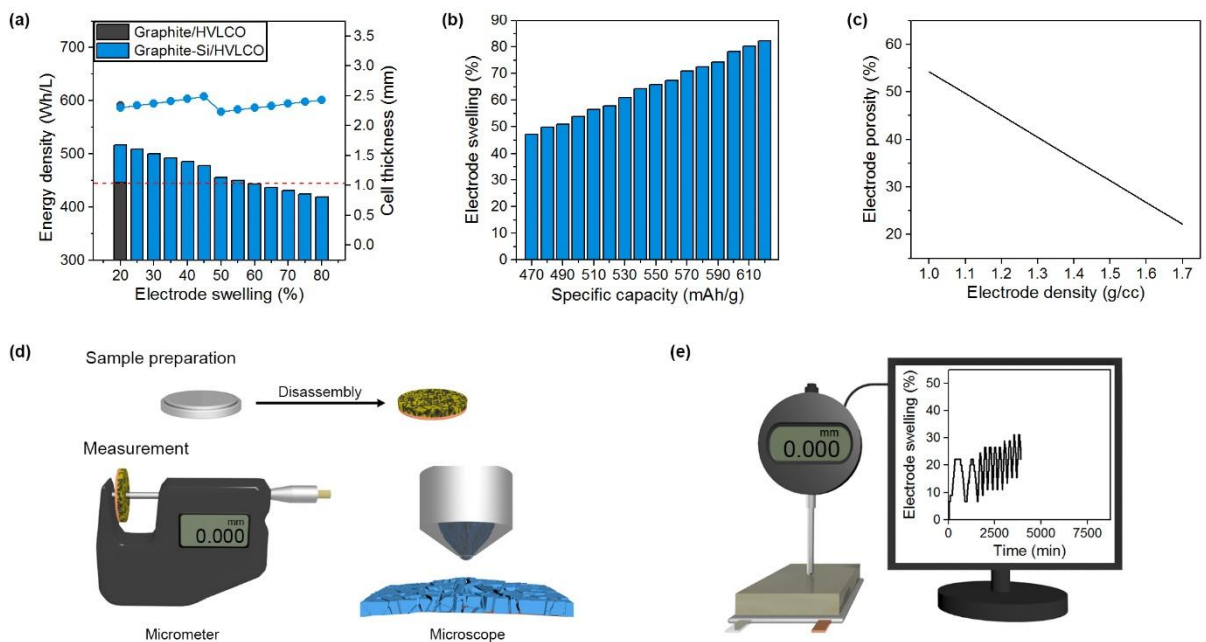


Figure 4. 4. The relationship between the energy density and the electrode swelling and the measurement of the electrode swelling. (a) Energy density plot of Graphite/HVLCO and graphite-blended Si anode/HVLCO full-cells as a function of the electrode swelling. (b) The limits of electrode swelling in different specific capacities of graphite-blended Si anode where the energy density of graphite-blended Si anode and graphite become the same. The electrode swelling of graphite is set as 20%. (c) Electrode porosity versus electrode density in graphite. The electrode porosity is estimated with the true density of graphite, binder, and conductive agents. (d) *Ex situ* measurement of the electrode swelling by micrometer and microscope. (e) *In situ* measurement of the electrode swelling with electrochemical dilatometry.

Capacity fading of the Si anode in the full-cell

Achieving stable cycle life of Si anodes in the high energy full-cell is another tough challenge for Si anode researchers in that the capacity fading of Si anodes is pronounced in the full-cell rather than in the half-cell. The differences in the electrochemical system between the half-cell and the full-cell result in the gap of capacity fading between the half-cell and full-cell (**Fig. 4. 5**). Typically, the half-cell comprises of the working electrode, such as the cathode or anode of LIBs, and lithium metal as both counter and reference electrodes, while the full-cell is built up with the cathode and anode. According to Christensen and Newman, the irreversible capacity is associated with the active material loss, whereas the reversible capacity loss is associated with side reactions⁶⁷. For reversible capacity loss, the addition of cyclable lithium in the cell can compensate the capacity loss. Therefore, the reversible capacity loss doesn't stand out in the half-cell, where the cyclable lithium is infinitely supplied from the lithium metal. In contrast, the consumption of cyclable lithium originated from the side reactions results in remarkable capacity losses in the lithium-confined full-cell. This phenomena can be easily observed in electrochemical data, such as the capacity retention and the cycling CE. The discharge capacity of the particular cycle is occasionally smaller than the charge capacity of the following cycle in the half-cell, however, this is not in the lithium-confined full-cell^{41,68}. Under this circumstance of the full-cell, the parasitic side reactions from repeated volume changes in the Si anode significantly deteriorate the cycling performances with consuming the cyclable lithium.

Additionally, from the three-electrode configuration including the working, counter and reference electrodes, the voltage profiles of the cathode and anode can be observed individually in the full-cell^{69,70} (**Fig. 4. 5b**). Unlike the constant cut-off voltage of the working electrode in the half-cell, the cut-off voltages of the cathode and Si anode move to higher voltages in the full-cell although the cut-off voltage of the full-cell is fixed. The shift of cut-off voltages occurs in both of charge and discharge of full-cell, and especially pronounced at the end of discharge. Consequently, the voltage window of cathode is narrowed, and the capacity of the active material is not exhibited as usual⁶⁹. Besides, regarding with a voltage profile of the Si anode in the full-cell, SOC shifts toward higher voltage as a consequence of the reductive side reactions, such as continuous growth of SEI layer, during the cycling, which hinders the utilization of low voltage region⁷⁰. SOC shift is fatal in the graphite-blended Si anode because the capacity of graphite at low voltage cannot be used when SOC shifts seriously.

Finally, the amount of electrolyte is limited in the commercial full-cell with considering the energy density and prices (**Fig. 4. 5c**). Generally, in most prototype full-cells, the electrolyte volume to the electrode pore volume ratio is adequately fixed between 2.5 and 3, where the electrode pore volume is the sum of the pore volumes of cathode and anode after calendaring³⁸. The small amount of electrolyte additives have a considerable influence on cycle life of the Si anode with favorable SEI layer

formation⁷¹. For example, fluoroethylene carbonate (FEC) is well known to be certainly effective in improving the capacity retention of the Si anode via forming denser and thinner SEI layer⁷². For the Si anode, the continuous growth of SEI layer consumes a lot of electrolytes including the additive. Although the effect of electrolyte consumption on capacity fading is not remarkable in the coin-type half-cell, in which an electrolyte is excessively injected, the limited amount of the electrolyte in full-cell can be depleted after long-term cycling. Hence, the depletion of the additives can bring about the sudden capacity fading during long-term cycling⁷³.

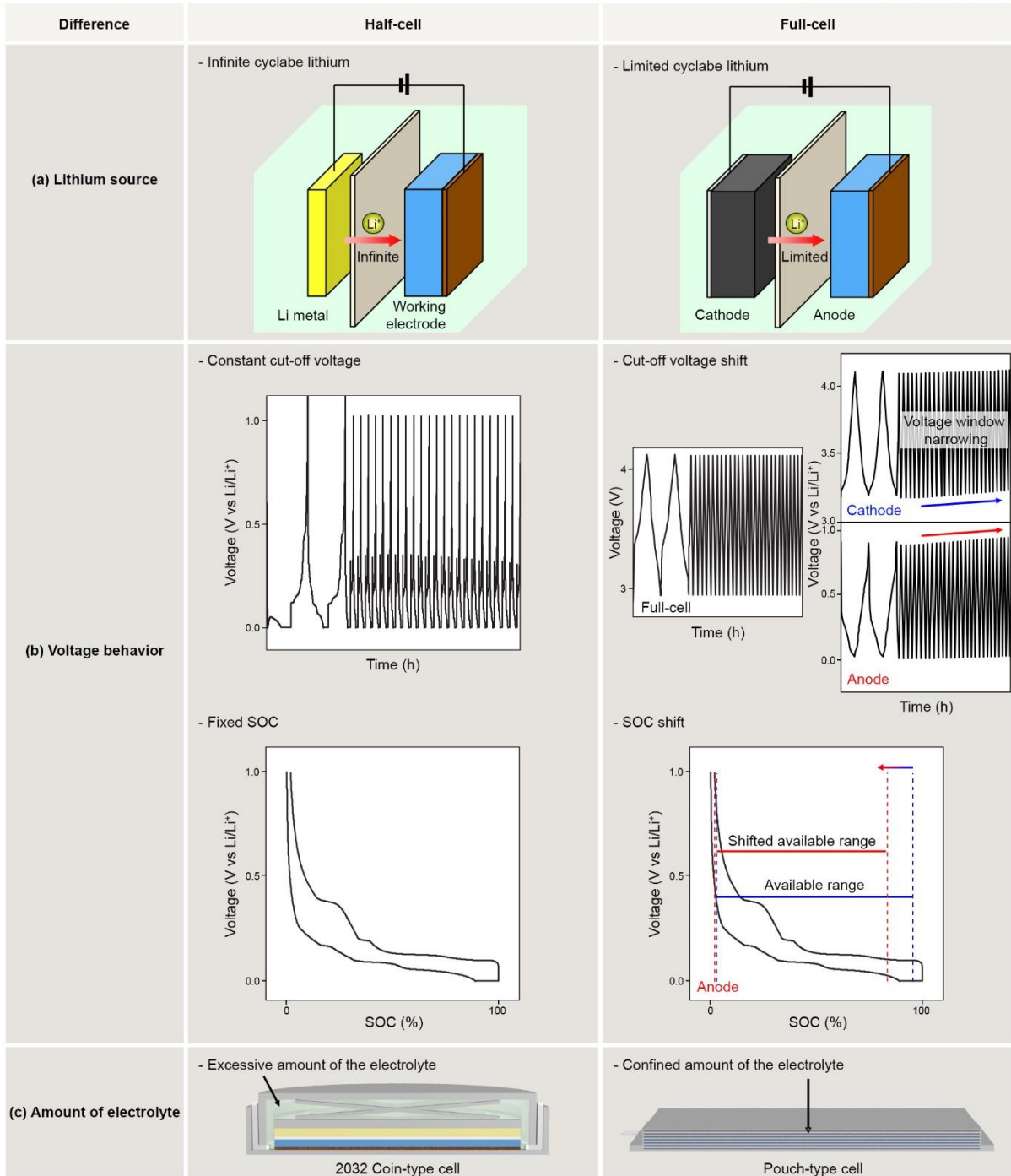


Figure 4. 5. The causes of the difference in the capacity fading between the half-cell and the full-cell. (a) Contrasting lithium sources in the half-cell and in the full-cell. The cyclable lithium is infinitely supplied from the lithium metal in the half-cell, whereas the supply is limited to the capacity of the cathode in the full-cell. (b) Different voltage behaviors between the half-cell and the full-cell. While the cut-off voltages and SOC are fixed with the lithium metal reference/counter electrode, the cut-off voltages and SOC shift as a result of the degradation. (c) The difference in the amounts of the electrolyte for the coin-type half-cell and for the commercial full-cell such as a pouch-type cell. The coin-type cell for the half-cell test is generally filled with the excessive amount of the electrolyte, on the other hand, the commercial cell such as pouch-type cell contains the limited amount of the electrolyte.

4.3 Conclusion and outlook

As the technological improvement in the Si anode proceeds, the practical implementation of the Si anode in the high energy full-cell is certainly the main task for battery researchers. This Perspective has organized the crucial factors of electrochemical cell design for high energy density. For an accurate evaluation of the Si anode, the influence of electrochemical cell design on electrochemical properties is discussed in detail. Besides, the issue of the electrode swelling is addressed in terms of the volumetric energy density. Meanwhile, we discussed the noticeable capacity fading of the Si anode in the full-cell. In order to realize high energy LIBs with utilizing Si in the future, the progress on the development should be accompanied by the implementation in high energy full-cell.

Finally, with regard to the development of the Si anode, we suggest the potential future direction associated with several issues as follows:

(1) Electrode swelling

When it comes to the practical application of the Si anode, the electrode swelling is one of the most critical challenges because of the volumetric energy density, the cycling performance and the safety. For the sake of low electrode swelling, the volume expansion of Si should be investigated in terms of the particle and the electrode levels. In the particle level, the crack and pulverization should be prevented after repeated cycles. Reducing the size of Si or building the mechanical clamping layer can decrease the strain and improve the fracture resistance⁷⁴⁻⁷⁶. Besides, Si alloys including SiO_x and Si-metal compounds can reduce the volume expansion of Si via diluting the active phase of Si with inactive phases such as Li₄SiO₄⁷⁷ and metal silicides⁵². Because the expansion of Si is proportional to the amount of lithium in Si matrix⁷⁸, it should be carefully considered to just suppress the expansion of Si. In the electrode level, the distribution of Si and void is important to electrode swelling. The aggregated Si increase the volume of electrode much more than the dispersed one^{29,40}. Thus, it is favorable to achieve the homogeneous distribution of Si in the whole electrode.

(2) Capacity fading

To improve the capacity retention of the Si anode in the full-cell, both reversible and irreversible capacity losses need to be mitigated. For reversible capacity loss, comprehensive strategies including material engineering and new electrolytes are desired in order to inhibit the continuous side reaction at re-exposed surface during cycling. It will minimize the required number of cycles for the stabilization, where cycling CE is above 99.5%, and increase the cycling CE over the whole cycling^{29,40,68}. Meanwhile, if the several issues of the prelithiation method such as safety, stability and compatibility with battery industry are resolved, it can be applicable for compensating the loss of cyclable lithium effectively^{67,79-}

⁸¹. For irreversible capacity loss, the pulverization and electrical isolation of Si should be avoided, which keeps the active material.

(3) Feasibility study

As we emphasized in this Perspective, the electrochemical properties of Si anode highly depend on the electrochemical cell design, and the capacity fading is accelerated in the full-cell. For the practical application of the Si anode to high-energy LIBs, it is indispensable to investigate the electrochemical behavior and the electrode swelling of the Si anode in the full-cell configuration while considering the electrochemical cell design. We believe that the comprehensive consideration about electrochemical cell design, which specifically aims for high volumetric energy density, will lay the groundwork for the realization of the high energy LIBs with utilizing the Si anode.

4.4 References

1. Dunn, J. B.; Gaines, L.; Kelly, J. C.; James, C.; Gallagher, K. G., The significance of Li-ion batteries in electric vehicle life-cycle energy and emissions and recycling's role in its reduction. *Energ Environ Sci* **2015**, 8 (1), 158-168.
2. Thackeray, M. M.; Wolverton, C.; Isaacs, E. D., Electrical energy storage for transportation—approaching the limits of, and going beyond, lithium-ion batteries. *Energ Environ Sci* **2012**, 5 (7), 7854-7863.
3. Blomgren, G. E., The Development and Future of Lithium Ion Batteries. *J Electrochem Soc* **2017**, 164 (1), A5019-A5025.
4. Crabtree, G.; Kocs, E.; Trahey, L., The energy-storage frontier: Lithium-ion batteries and beyond. *Mrs Bulletin* **2015**, 40 (12), 1067-1078.
5. Choi, J. W.; Aurbach, D., Promise and reality of post-lithium-ion batteries with high energy densities. *Nature Reviews Materials* **2016**, 1, 16013.
6. Obrovac, M. N.; Christensen, L., Structural changes in silicon anodes during lithium insertion/extraction. *Electrochem Solid St* **2004**, 7 (5), A93-A96.
7. Obrovac, M. N.; Krause, L. J., Reversible cycling of crystalline silicon powder. *J Electrochem Soc* **2007**, 154 (2), A103-A108.
8. Chandrasekaran, R.; Magasinski, A.; Yushin, G.; Fuller, T. F., Analysis of Lithium Insertion/Deinsertion in a Silicon Electrode Particle at Room Temperature. *J Electrochem Soc* **2010**, 157 (10), A1139-A1151.
9. Nitta, N.; Wu, F. X.; Lee, J. T.; Yushin, G., Li-ion battery materials: present and future. *Materials Today* **2015**, 18 (5), 252-264.
10. McDowell, M. T.; Lee, S. W.; Harris, J. T.; Korgel, B. A.; Wang, C.; Nix, W. D.; Cui, Y., In situ TEM of two-phase lithiation of amorphous silicon nanospheres. *Nano Lett* **2013**, 13 (2), 758-64.
11. McDowell, M. T.; Lee, S. W.; Nix, W. D.; Cui, Y., 25th anniversary article: Understanding the lithiation of silicon and other alloying anodes for lithium-ion batteries. *Adv. Mater.* **2013**, 25 (36), 4966-85.
12. Pollak, E.; Salitra, G.; Baranchugov, V.; Aurbach, D., In situ conductivity, impedance spectroscopy, and ex situ raman spectra of amorphous silicon during the Insertion/Extraction of lithium. *J Phys Chem C* **2007**, 111 (30), 11437-11444.
13. Wang, J. W.; He, Y.; Fan, F.; Liu, X. H.; Xia, S.; Liu, Y.; Harris, C. T.; Li, H.; Huang, J. Y.; Mao, S. X.; Zhu, T., Two-phase electrochemical lithiation in amorphous silicon. *Nano Letters* **2013**, 13 (2), 709-715.
14. Liu, X. H.; Zhong, L.; Huang, S.; Mao, S. X.; Zhu, T.; Huang, J. Y., Size-Dependent Fracture

- of Silicon Nanoparticles During Lithiation. *Acs Nano* **2012**, *6* (2), 1522-1531.
15. Dash, R.; Pannala, S., Theoretical Limits of Energy Density in Silicon-Carbon Composite Anode Based Lithium Ion Batteries. *Sci Rep* **2016**, *6*, 27449.
 16. Kalnaus, S.; Rhodes, K.; Daniel, C., A study of lithium ion intercalation induced fracture of silicon particles used as anode material in Li-ion battery. *J Power Sources* **2011**, *196* (19), 8116-8124.
 17. Kumar, R.; Tokranov, A.; Sheldon, B. W.; Xiao, X. C.; Huang, Z. Q.; Li, C. Z.; Mueller, T., In Situ and Operando Investigations of Failure Mechanisms of the Solid Electrolyte Interphase on Silicon Electrodes. *Acs Energy Letters* **2016**, *1* (4), 689-697.
 18. Wu, H.; Cui, Y., Designing nanostructured Si anodes for high energy lithium ion batteries. *Nano Today* **2012**, *7* (5), 414-429.
 19. Park, C. M.; Kim, J. H.; Kim, H.; Sohn, H. J., Li-alloy based anode materials for Li secondary batteries. *Chem Soc Rev* **2010**, *39* (8), 3115-41.
 20. Ryu, J. H.; Kim, J. W.; Sung, Y. E.; Oh, S. M., Failure modes of silicon powder negative electrode in lithium secondary batteries. *Electrochem Solid St* **2004**, *7* (10), A306-A309.
 21. Zhang, W. J., A review of the electrochemical performance of alloy anodes for lithium-ion batteries. *J Power Sources* **2011**, *196* (1), 13-24.
 22. Ko, M.; Chae, S.; Cho, J., Challenges in Accommodating Volume Change of Si Anodes for Li-Ion Batteries. *ChemElectroChem* **2015**, *2* (11), 1645-1651.
 23. Li, Y.; Yan, K.; Lee, H.-W.; Lu, Z.; Liu, N.; Cui, Y., Growth of conformal graphene cages on micrometre-sized silicon particles as stable battery anodes. *Nature Energy* **2016**, *1*, 15029.
 24. Liu, N.; Lu, Z.; Zhao, J.; McDowell, M. T.; Lee, H.-W.; Zhao, W.; Cui, Y., A pomegranate-inspired nanoscale design for large-volume-change lithium battery anodes. *Nat Nanotechnol* **2014**, *9* (3), 187-192.
 25. Su, X.; Wu, Q. L.; Li, J. C.; Xiao, X. C.; Lott, A.; Lu, W. Q.; Sheldon, B. W.; Wu, J., Silicon-Based Nanomaterials for Lithium-Ion Batteries: A Review. *Adv. Energy Mater.* **2014**, *4* (1).
 26. Zhao, H.; Yuan, W.; Liu, G., Hierarchical electrode design of high-capacity alloy nanomaterials for lithium-ion batteries. *Nano Today* **2015**, (0).
 27. Zuo, X. X.; Zhu, J.; Muller-Buschbaum, P.; Cheng, Y. J., Silicon based lithium-ion battery anodes: A chronicle perspective review. *Nano Energy* **2017**, *31*, 113-143.
 28. Chae, S.; Ko, M.; Park, S.; Kim, N.; Ma, J.; Cho, J., Micron-sized Fe-Cu-Si ternary composite anodes for high energy Li-ion batteries. *Energ Environ Sci* **2016**, *9* (4), 1251-1257.
 29. Chae, S.; Kim, N.; Ma, J.; Cho, J.; Ko, M., One-to-One Comparison of Graphite-Blended Negative Electrodes Using Silicon Nanolayer-Embedded Graphite versus Commercial Benchmarking Materials for High-Energy Lithium-Ion Batteries. *Adv. Energy Mater.* **2017**,

- 1700071.
30. Yim, C. H.; Niketic, S.; Salem, N.; Naboka, O.; Abu-Lebdeh, Y., Towards Improving the Practical Energy Density of Li-Ion Batteries: Optimization and Evaluation of Silicon: Graphite Composites in Full Cells. *J Electrochem Soc* **2017**, *164* (1), A6294-A6302.
 31. Du, Z. J.; Dunlap, R. A.; Obrovac, M. N., High Energy Density Calendered Si Alloy/Graphite Anodes. *J Electrochem Soc* **2014**, *161* (10), A1698-A1705.
 32. Li, J.-Y.; Xu, Q.; Li, G.; Yin, Y.-X.; Wan, L.-J.; Guo, Y.-G., Research progress regarding Si-based anode materials towards practical application in high energy density Li-ion batteries. *Mater. Chem. Front.* **2017**.
 33. Obrovac, M. N.; Chevrier, V. L., Alloy Negative Electrodes for Li-Ion Batteries. *Chemical Reviews* **2014**, *114* (23), 11444-11502.
 34. Winter, M.; Besenhard, J. O.; Spahr, M. E.; Novak, P., Insertion electrode materials for rechargeable lithium batteries. *Adv. Mater.* **1998**, *10* (10), 725-763.
 35. Yoshio, M.; Wang, H.; Fukuda, K., Spherical carbon-coated natural graphite as a lithium-ion battery-anode material. *Angew Chem Int Ed Engl* **2003**, *42* (35), 4203-6.
 36. Yoshio, M.; Wang, H. Y.; Fukuda, K.; Umeno, T.; Abe, T.; Ogumi, Z., Improvement of natural graphite as a lithium-ion battery anode material, from raw flake to carbon-coated sphere. *J Mater Chem* **2004**, *14* (11), 1754-1758.
 37. Tran, H. Y.; Greco, G.; Taubert, C.; Wohlfahrt-Mehrens, M.; Haselrieder, W.; Kwade, A., Influence of electrode preparation on the electrochemical performance of LiNi_{0.8}Co_{0.15}Al_{0.05}O₂ composite electrodes for lithium-ion batteries. *J Power Sources* **2012**, *210*, 276-285.
 38. Gallagher, K. G.; Trask, S. E.; Bauer, C.; Woehle, T.; Lux, S. F.; Tschek, M.; Lamp, P.; Polzin, B. J.; Ha, S.; Long, B.; Wu, Q. L.; Lu, W. Q.; Dees, D. W.; Jansen, A. N., Optimizing Areal Capacities through Understanding the Limitations of Lithium-Ion Electrodes. *J Electrochem Soc* **2016**, *163* (2), A138-A149.
 39. Buqa, H.; Goers, D.; Holzapfel, M.; Spahr, M. E.; Novak, P., High rate capability of graphite negative electrodes for lithium-ion batteries. *J Electrochem Soc* **2005**, *152* (2), A474-A481.
 40. Ko, M.; Chae, S.; Ma, J.; Kim, N.; Lee, H. W.; Cui, Y.; Cho, J., Scalable synthesis of silicon-nanolayer-embedded graphite for high-energy lithium-ion batteries. *Nature Energy* **2016**, *1*.
 41. Jin, Y.; Li, S.; Kushima, A.; Zheng, X. Q.; Sun, Y. M.; Xie, J.; Sun, J.; Xue, W. J.; Zhou, G. M.; Wu, J.; Shi, F. F.; Zhang, R. F.; Zhu, Z.; So, K. P.; Cui, Y.; Li, J., Self-healing SEI enables full-cell cycling of a silicon-majority anode with a coulombic efficiency exceeding 99.9%. *Energ Environ Sci* **2017**, *10* (2), 580-592.
 42. Gogotsi, Y.; Simon, P., True Performance Metrics in Electrochemical Energy Storage. *Science*

- 2011**, 334 (6058), 917-918.
43. Chou, S. L.; Pan, Y.; Wang, J. Z.; Liu, H. K.; Dou, S. X., Small things make a big difference: binder effects on the performance of Li and Na batteries. *Phys Chem Chem Phys* **2014**, 16 (38), 20347-59.
 44. Fransson, L.; Eriksson, T.; Edstrom, K.; Gustafsson, T.; Thomas, J. O., Influence of carbon black and binder on Li-ion batteries. *J Power Sources* **2001**, 101 (1), 1-9.
 45. Sawai, K.; Ohzuku, T., Factors affecting rate capability of graphite electrodes for lithium-ion batteries. *J Electrochem Soc* **2003**, 150 (6), A674-A678.
 46. Danner, T.; Singh, M.; Hein, S.; Kaiser, J.; Hahn, H.; Latz, A., Thick electrodes for Li-ion batteries: A model based analysis. *J Power Sources* **2016**, 334, 191-201.
 47. Singh, M.; Kaiser, J.; Hahn, H., Thick Electrodes for High Energy Lithium Ion Batteries. *J Electrochem Soc* **2015**, 162 (7), A1196-A1201.
 48. Lu, W. Q.; Jansen, A.; Dees, D.; Nelson, P.; Veselka, N. R.; Henriksen, G., High-energy electrode investigation for plug-in hybrid electric vehicles. *J Power Sources* **2011**, 196 (3), 1537-1540.
 49. Zheng, H. H.; Li, J.; Song, X. Y.; Liu, G.; Battaglia, V. S., A comprehensive understanding of electrode thickness effects on the electrochemical performances of Li-ion battery cathodes. *Electrochim Acta* **2012**, 71, 258-265.
 50. Suthar, B.; Northrop, P. W. C.; Rife, D.; Subramanian, V. R., Effect of Porosity, Thickness and Tortuosity on Capacity Fade of Anode. *J Electrochem Soc* **2015**, 162 (9), A1708-A1717.
 51. Beattie, S. D.; Larcher, D.; Morcrette, M.; Simon, B.; Tarascon, J. M., Si electrodes for li-ion batteries - A new way to look at an old problem. *J Electrochem Soc* **2008**, 155 (2), A158-A163.
 52. Chevrier, V. L.; Liu, L.; Le, D. B.; Lund, J.; Molla, B.; Reimer, K.; Krause, L. J.; Jensen, L. D.; Figgemeier, E.; Eberman, K. W., Evaluating Si-Based Materials for Li-Ion Batteries in Commercially Relevant Negative Electrodes. *J Electrochem Soc* **2014**, 161 (5), A783-A791.
 53. Gor, G. Y.; Cannarella, J.; Prevost, J. H.; Arnold, C. B., A Model for the Behavior of Battery Separators in Compression at Different Strain/Charge Rates. *J Electrochem Soc* **2014**, 161 (11), F3065-F3071.
 54. Lee, J. H.; Lee, H. M.; Ahn, S., Battery dimensional changes occurring during charge/discharge cycles—thin rectangular lithium ion and polymer cells. *J Power Sources* **2003**, 119–121, 833-837.
 55. Lamb, J.; Orendorff, C. J., Evaluation of mechanical abuse techniques in lithium ion batteries. *J Power Sources* **2014**, 247, 189-196.
 56. Doughty, D. H.; Roth, E. P., A General Discussion of Li Ion Battery Safety. *The Electrochemical Society Interface* **2012**, 21 (2), 37-44.

57. Ohzuku, T.; Matoba, N.; Sawai, K., Direct evidence on anomalous expansion of graphite-negative electrodes on first charge by dilatometry. *J Power Sources* **2001**, 97-8, 73-77.
58. Bitzer, B.; Gruhle, A., A new method for detecting lithium plating by measuring the cell thickness. *J Power Sources* **2014**, 262, 297-302.
59. Kim, C. S.; Jeong, K. M.; Kim, K.; Yi, C. W., Effects of Capacity Ratios between Anode and Cathode on Electrochemical Properties for Lithium Polymer Batteries. *Electrochim Acta* **2015**, 155, 431-436.
60. Besenhard, J. O.; Winter, M.; Yang, J.; Biberacher, W., *Abstracts of the 7th International Meeting on Lithium Batteries* **1994**, 7, 278
61. Besenhard, J. O.; Winter, M.; Yang, J.; Biberacher, W., Filming Mechanism of Lithium-Carbon Anodes in Organic and Inorganic Electrolytes. *J Power Sources* **1995**, 54 (2), 228-231.
62. Biberacher, W.; Lurf, A.; Besenhard, J. O.; Möhwald, H.; Butz, T., A high resolution dilatometer for in situ studies of the electrointercalation of layered materials. *Mater Res Bull* **1982**, 17 (11), 1385-1392.
63. Besenhard, J. O.; Yang, J.; Winter, M., Will advanced lithium-alloy anodes have a chance in lithium-ion batteries? *J Power Sources* **1997**, 68 (1), 87-90.
64. Jeong, G.; Lee, S. M.; Choi, N. S.; Kim, Y. U.; Lee, C. K., Stabilizing dimensional changes in Si-based composite electrodes by controlling the electrode porosity: An in situ electrochemical dilatometric study. *Electrochim Acta* **2011**, 56 (14), 5095-5101.
65. Kim, H. K.; Roh, K. C.; Kim, K. B., In Situ Electrochemical Dilatometric Study of Fe₃O₄/Reduced Graphene Oxide Nanocomposites as Anode Material for Lithium Ion Batteries. *J Electrochem Soc* **2015**, 162 (12), A2308-A2312.
66. Kim, T.; Park, S.; Oh, S. M., Solid-state NMR and electrochemical dilatometry study on Li⁺ uptake/extraction mechanism in SiO electrode. *J Electrochem Soc* **2007**, 154 (12), A1112-A1117.
67. Christensen, J.; Newman, J., Cyclable Lithium and Capacity Loss in Li-Ion Cells. *J Electrochem Soc* **2005**, 152 (4), A818-A829.
68. Wu, H.; Chan, G.; Choi, J. W.; Ryu, I.; Yao, Y.; McDowell, M. T.; Lee, S. W.; Jackson, A.; Yang, Y.; Hu, L.; Cui, Y., Stable cycling of double-walled silicon nanotube battery anodes through solid-electrolyte interphase control. *Nat Nanotechnol* **2012**, 7 (5), 310-5.
69. Kierzek, K.; Machnikowski, J., Factors influencing cycle-life of full Li-ion cell built from Si/C composite as anode and conventional cathodic material. *Electrochim Acta* **2016**, 192, 475-481.
70. Klett, M.; Gilbert, J. A.; Trask, S. E.; Polzin, B. J.; Jansen, A. N.; Dees, D. W.; Abraham, D. P., Electrode Behavior RE-Visited: Monitoring Potential Windows, Capacity Loss, and Impedance Changes in Li-1.03(Ni_{0.5}Co_{0.2}Mn_{0.3})(0.97)O₂/Silicon-Graphite Full Cells. *J*

- Electrochem Soc* **2016**, *163* (6), A875-A887.
71. Xu, K., Electrolytes and interphases in Li-ion batteries and beyond. *Chem Rev* **2014**, *114* (23), 11503-618.
 72. Choi, N.-S.; Yew, K. H.; Lee, K. Y.; Sung, M.; Kim, H.; Kim, S.-S., Effect of fluoroethylene carbonate additive on interfacial properties of silicon thin-film electrode. *J Power Sources* **2006**, *161* (2), 1254-1259.
 73. Petibon, R.; Chevrier, V. L.; Aiken, C. P.; Hall, D. S.; Hyatt, S. R.; Shunmugasundaram, R.; Dahn, J. R., Studies of the Capacity Fade Mechanisms of LiCoO₂/Si-Alloy: Graphite Cells. *J Electrochem Soc* **2016**, *163* (7), A1146-A1156.
 74. Gao, H.; Xiao, L.; Plümel, I.; Xu, G.-L.; Ren, Y.; Zuo, X.; Liu, Y.; Schulz, C.; Wiggers, H.; Amine, K.; Chen, Z., Parasitic Reactions in Nanosized Silicon Anodes for Lithium-Ion Batteries. *Nano Letters* **2017**, *17* (3), 1512-1519.
 75. Kim, H.; Seo, M.; Park, M. H.; Cho, J., A Critical Size of Silicon Nano-Anodes for Lithium Rechargeable Batteries. *Angewandte Chemie, International Edition* **2010**, *49* (12), 2146-2149.
 76. Lee, S. W.; Lee, H. W.; Ryu, I.; Nix, W. D.; Gao, H. J.; Cui, Y., Kinetics and fracture resistance of lithiated silicon nanostructure pairs controlled by their mechanical interaction. *Nature Communications* **2015**, *6*, 7533.
 77. Al-Maghrabi, M. A.; Suzuki, J.; Sanderson, R. J.; Chevrier, V. L.; Dunlap, R. A.; Dahn, J. R., Combinatorial Studies of Si_{1-x}O_x as a Potential Negative Electrode Material for Li-Ion Battery Applications. *J Electrochem Soc* **2013**, *160* (9), A1587-A1593.
 78. Chevrier, V. L.; Dahn, J. R., First Principles Model of Amorphous Silicon Lithiation. *J Electrochem Soc* **2009**, *156* (6), A454-A458.
 79. Sun, Y. M.; Lee, H. W.; Seh, Z. W.; Liu, N.; Sun, J.; Li, Y. Z.; Cui, Y., High-capacity battery cathode prelithiation to offset initial lithium loss. *Nature Energy* **2016**, *1*, 15008.
 80. Zhao, J.; Lu, Z.; Wang, H.; Liu, W.; Lee, H. W.; Yan, K.; Zhuo, D.; Lin, D.; Liu, N.; Cui, Y., Artificial Solid Electrolyte Interphase-Protected Li_xSi Nanoparticles: An Efficient and Stable Prelithiation Reagent for Lithium-Ion Batteries. *J Am Chem Soc* **2015**, *137* (26), 8372-5.
 81. Zhao, J.; Lu, Z.; Liu, N.; Lee, H. W.; McDowell, M. T.; Cui, Y., Dry-air-stable lithium silicide-lithium oxide core-shell nanoparticles as high-capacity prelithiation reagents. *Nat Commun* **2014**, *5*, 5088.

Acknowledgement

힘든 대학원 과정 끝에 많은 분들의 도움으로 무사히 박사학위를 받게 되었습니다. 짧은 글로나마 감사의 인사를 드리고자 합니다.

가장 먼저, 우수한 연구 환경에서 아낌없이 지도해주신 조재필 교수님께 감사드립니다. 어려운 연구 과제라도 항상 믿고 맡겨 주셔서 주체적인 연구자로 성장할 수 있었습니다. 학부 연구 인턴 생활부터 5년이 넘도록 더 나은 결과를 위해 누구보다 열정적이고 성실하신 교수님을 보면서, 이제 막 연구자의 길로 접어드려 는 저에게는 최고의 롤 모델이 되어 주셨습니다. 졸업 후에도 늘 절실한 마음으로 훌륭한 연구자가 될 수 있도록 노력하겠습니다.

바쁘신 와중에도 제 박사학위 논문을 심사해 주신 정경민 교수님, 최남순 교수님, 강석주 교수님, 이현욱 교수님께 감사드립니다. 교수님들께서 해주신 조언과 가르침 덕분에 더 넓은 시야를 갖고 발전할 수 있었습니다.

처음 연구실을 들어왔을 때, 연구실에 적응할 수 있도록 가족처럼 해주시고 많은 것을 알려주셨던 고민성 형님, 오필건 형님, 정수경 형님, 손윤국 형님 덕분에 아무것도 모르던 제가 연구실 생활을 잘 시작하고 또 성장할 수 있었습니다. 그 외에 많은 NESM 선배님들께도 감사드립니다.

힘든 프로젝트들에서도 서로 믿고 도와준 우리 음극 팀원들, 손영욱 형, 남규태 형, 박승규 형, 마지영 형, 성재경 형, 최성현 형, 이운광 형, 김남형, 안기홍, 이태용, 신슬기, 장해성. 여러분들과 함께 연구할 수 있어서 대학원 생활이 즐거웠고, 저의 부족한 많은 부분들을 배울 수 있었습니다. 대학원 기간 동안 동고동락한 동기들 류재찬, 조용래, 그리고 석사로 졸업한 동기들 공그림, 노은솔 누나까지. 힘든 시기에 힘이 되어주어 감사합니다. 그 외에도 각자의 자리에서 더 나은 연구실을 위해 애써준 후배님들, 김준혁, 진우영, 마현수 형, 차형연, 윤문수 형, 황재성, 이효명, 이소미, 강주원, 유영빈, 구예현. 앞으로도 더욱 열심히 해서 좋은 결과가 있길 바라겠습니다.

마지막으로, 가장 사랑하는 부모님과 형에게 감사의 인사를 드립니다. 항상 제가 하고 싶어 하는 일을 믿고 지원 해주시고, 크고 든든한 버팀목이 되어 주셔서 감사합니다. 앞으로도 더욱 열심히 정진하여 자랑스런 아들이 되도록 노력하겠습니다. 사랑합니다.